A Numerical Protocol for Death-time Estimation

Sipho Mfolozi

MBChB (UCT), Dip For Med (SA) Path, FC For Path (SA), MMed Forensic Pathology (UCT)

Thesis Presented for the Degree of

DOCTOR OF PHILOSOPHY

Faculty of Health Sciences

UNIVERSITY OF CAPE TOWN

March 2021

Supervisors:

Professor Arnaud George Malan

Professor Tunde Bello-Ochende

Professor Lorna Jean Martin

TABLE OF CONTENTS

LIST OF USED ACRONYMS……………………………………………………………iv

DECLARATION……………………………………………………………………..1

ABSTRACT……………………………………………………………………..…4

ACKNOWLEDGEMENTS……………………………………………………………6

CHAPTER 1……………………………………………………………..……....………8
Introduction and background

CHAPTER 2……………………………………………………………………………..15
Research aims, objectives and setting

CHAPTER 3……………………………………………………………………………...28
Bibliographic review of death-time estimation methods

CHAPTER 4……………………………………………………………………………...62
Bibliographic review of bioheat modelling methods

CHAPTER 5……………………………………………………………..……...……99
Research materials and methods

CHAPTER 6…………………………………………………………………...…120
Numerical approximation of antemortem body temperature

CHAPTER 7………………………………………………………………………….139
Numerical analysis of postmortem axial heat transfer

CHAPTER 8…………………………………………………………...……………175
Multipoint axial thermometry

CHAPTER 9……………………………………………………………......…………193
A numerical protocol for death-time estimation

CHAPTER 10……………...……………………………………………………..245
Sources of uncertainty and limitations

CHAPTER 11……………………………………………..……………..……………..263
Summary and conclusions

ANNEXURE 1……………………………………………………………………supplied

LIST OF USED ACRONYMS

Acronym	**Explanation**
1D	One dimensional
3D	Three dimensional
ADD	Accumulated Degree Day
AI	Artificial intelligence
ASME	American Society of Mechanical Engineers
BMI	Body mass index
CFD	Computational fluid dynamics
CT	Computed tomography
CMSA	Colleges of Medicine of South Africa
FDTD	Finite difference time domain
FEM	Finite Element Model
GISS	Goddard Institute of Space Studies
IT'IS	Information Technologies in Society
MAT	Multipoint axial thermometry
MRI	Magnetic resonance image
MRtI	Magnetic resonance thermal image
NASA	National Aeronautics and Space Administration
NCEI	National Centres of Environmental Information
NOAA	National Oceanic and Atmospheric Administration
NRF	National Research Foundation
PMTP	Postmortem temperature plateau
PMI	Postmortem interval
TEF	Triple Exponential Formula
TOD	Time of death
UCT	University of Cape Town
ViP	Virtual Population

DECLARATION

I, Sipho Mfolozi, am the author of all parts of this thesis. Roles and contribution of supervisors are described below per chapter.

Chapter 6

Mfolozi S, Malan AG, Bello-Ochende T, Martin LJ. Numerical approximation of antemortem body temperature.

Sipho Mfolozi was the lead investigator in this numerical analysis study. He designed the study. All computational techniques in the methods section were executed by him. He performed post-processing and data analysis. Lorna Jean Martin supervised the forensic pathology aspect of the study. Arnaud George Malan and Tunde Bello-Ochende guided and supervised on relevant aspects of heat-transfer and numerical analysis, which included its physics and mathematical handling. Sipho Mfolozi prepared the manuscript, which was critically reviewed by all authors.

Chapter 7

Mfolozi S, Malan AG, Bello-Ochende T, Martin LJ. Numerical analysis of postmortem axial heat transfer.

Sipho Mfolozi was the lead investigator in this numerical analysis study. He designed the study. All computational techniques in the methods section were executed by him. He performed post-processing and data analysis. Lorna Jean Martin supervised the forensic pathology aspect of the study. Arnaud George Malan and Tunde Bello-Ochende guided and supervised on relevant aspects of heat-transfer and numerical analysis, which included its physics and mathematical handling. Sipho Mfolozi prepared the manuscript, which was critically reviewed by all authors.

Chapter 8

Mfolozi S, Malan AG, Bello-Ochende T, Martin LJ. Multipoint Axial Thermometry.

Sipho Mfolozi was the lead investigator and designer of this empirical and numerical demonstration study. Research materials were procured by him. He built the cooling dummy used as a human surrogate. He conceptualised and designed the proposed multipoint axial thermometry device, which was built by a privately contracted company. Sipho Mfolozi performed all the manual experiment tasks. Arnaud George Malan supervised on relevant aspects of heat-transfer.

Chapter 9

Mfolozi S, Malan AG, Bello-Ochende T, Martin LJ. A numerical protocol for death-time estimation.

Sipho Mfolozi was the lead investigator who designed the study. He created the 3D model of the proposed device for measurement of axial isotherms in the simulation environment. He conceptualised the numerical protocol and all computational techniques used were executed by him. He performed post-processing and data analysis. Lorna Jean Martin supervised the forensic pathology aspect of the study.

Arnaud George Malan and Tunde Bello-Ochende guided and supervised on relevant aspects of heat transfer and numerical analysis, which included its physics and mathematical handling. Sipho Mfolozi prepared the authored the chapter, which was critically reviewed by all authors.

Chapter 10

Mfolozi S, Malan AG, Bello-Ochende T, Martin LJ. Sources of uncertainty and limitations.

Arnaud George Malan and Tunde Bello-Ochende guided and supervised on relevant aspects of heat transfer and numerical analysis, which included its physics and mathematical handling. Sipho Mfolozi prepared the authored the chapter, which was critically reviewed by all authors.

Chapter 11

Mfolozi S, Malan AG, Bello-Ochende T, Martin LJ. Summary and conclusions. Sipho Mfolozi prepared the authored the chapter, which was critically reviewed by all authors.

Signed,

Signed by candidate

Sipho Mfolozi
March 2021

ABSTRACT

A body's axial temperature distribution at death was experimentally demonstrated by the author to predict the postmortem temperature plateau (PMTP), which is known to affect the measured core temperature value and hence death-time estimation. Yet today's methods of death-time estimation apply only a single-point approximation of a body's core temperature in life as well as a single-point measurement of a body's core temperature after death.

Four studies were carried out to understand the relationship between a body's axial temperature distribution and the PMTP. The first study numerically approximated antemortem temperature distribution in an MRI-built, high-definition, anatomically-segmented 3D computational human phantom consisting of several hundred tissues. Metabolic heat generation (Q_m) and blood perfusion (ω_b) parameters were applied to all thermogenic tissue using the Pennes BioHeat Model. The study demonstrated that the antemortem axial temperature distribution was nonlinear, that tissue temperature distribution was inhomogeneous, and that the position and size of the antemortem central isotherm was predicted by the size, shape and location of the most thermogenic internal organ in a given axial plane. Numerical approximation of a body's antemortem axial temperature distribution using this study's materials and methods was proposed for death-time estimation.

The second study examined postmortem axial heat transfer. The approximated antemortem axial temperature distribution constituted the initial condition. Q_m and ω_b were set to zero to simulate death. Postmortem cooling was simulated in still air, on a cold concrete floor and on a heated floor. The antemortem central isotherm that single-point core thermometry detects was the PMTP. Its size at death, body radius, axial thermometry-depth and length of the postmortem interval (PMI) all predicted PMTP length. The cold concrete floor shifted the central isotherm away from the floor, while the heated floor shifted it towards the floor. Ground temperature and material properties, along with the aforementioned PMTP

predictors, result in variation in measured single-point core thermometry values, yet today's death-time estimation methods do not measure, approximate or standardise them. This is a source of uncertainty. This study demonstrated that a body's postmortem axial thermal profile was very specific to the PMI at which it exists, including during the PMTP that single-point core thermometry detects. This study proposed a body's measured postmortem axial thermal profile for death-time estimation to reduce PMTP uncertainties. The study also proposed numerical modelling of the ground, its temperature and material properties.

The third study proposed a multipoint axial thermometry (MAT) device to measure a body's postmortem axial thermal profile. The author designed the device prototype. Its fabrication was outsourced. Empiric and numerical MAT studies were conducted on a cooling dummy and 3D human phantom, respectively. MAT curves indicated a parabolic shape.

The fourth study proposed a numerical protocol for death-time estimation that iteratively tested a MAT profile measured at an unknown PMI from a decedent using the proposed MAT device against MAT profiles predicted by numerical simulations of sequentially longer candidate PMIs. A candidate PMI whose MAT profile matched was considered the PMI estimated by the protocol. The proposed protocol applied the exact historical meteorological temperatures that existed during the final estimated PMI. Application of the protocol was demonstrated using a fictitious scenario in which a candidate PMI within 120s of the final estimated PMI was excluded. Potential sources of uncertainty of the proposed protocol were discussed and concluding remarks on future research were made.

ACKNOWLEDGEMENTS

The research was funded by the National Research Foundation (NRF) of South Africa under the Thuthuka PhD Track funding instrument, fund number TK14042966700. Sim4Life®, the biological simulation software that includes a thermal solver, was generously provided by Zurich MedTech, Switzerland. The 3D computational phantoms were generously provided by IT'IS Foundation, Switzerland.

I thank Professor Arnaud George Malan and Professor Tunde Bello-Ochende for their frank pragmatic advice and mentoring. I thank Professor Lorna Martin for endless patience that allowed me time to complete this study. I thank Niran Ilangkoon for assisting me with the spreadsheet. I thank all my former colleagues in the Division of Forensic Medicine at UCT for putting up with me during this time. My late father A. M. Mfolozi inspired me to be bold and tenacious, and to excel. My mother M. N. Mgidlana showed constant unconditional love and support. I thank them both. I thank Prof Alan Morris for being my spiritual mentor and adopted father. I thank my brother, Dr Msimelelo Mgidlana, for supporting me through rough patches in my life. Thank you Thombela. I acknowldge my Masters of Medicine examiner and colleague, the late Professor Jacob Johannes Dempers, for encouraging me to continue my research by registering for this degree.

Sipho Mfolozi.
March 2021

CHAPTER 1

Introduction and background

Chapter 1

Introduction and background

In 2009, the author, Sipho Mfolozi, registered for the degree of Master of Medicine in Forensic Pathology at the University of Cape Town, South Africa. The aim of his research was to derive empiric corrective factors of measured wind-speed and measured relative humidity, to build onto those of the Henβge[1] Rectal Temperature Nomogram method of death-time estimation. His dissertation title was *Cooling rates of dummies under various degrees of air humidity, wind speed and air temperature*[2]. The corrective factors Mfolozi sought were to be programmed into an electronic device for estimating the postmortem interval that he had invented that year. The device was patented in South Africa in 2011[3,4].

Human surrogates Mfolozi used were known as *cooling dummies*, the same kind used by Henβge in the 1970s and 80s. Mfolozi fitted permanent digital thermocouple probes in their deep-core to record their temperature during postmortem cooling. Mfolozi would preheat the cooling dummies to 37°C in an incubator to simulate antemortem temperature distribution. Subsequent postmortem cooling after removal from the incubator produced a postmortem temperature plateau (PMTP). This is a well-documented period in the early postmortem cooling phase during which the core temperature remains relatively stable for a variable interval. PMTP causes were poorly understood and controversial.

The PMTP was a particularly contentious topic because a mathematical method of estimating the PMI had to take it into consideration. A mathematical expression of rectal cooling, which had been described by Marshall and Hoare[5] and was the basis for the Henβge's Nomogram method, consists of a term whose exponent represents the PMTP. Attempts to describe methods of quantifying the PMTP value of a given dead body that would be neatly applied to Marshall and Hoare's mathematical expression proved unsuccessful. The PMTP thus remained a source of uncertainty of death-time estimation despite many studies that tried to explain its causes.

Among Mfolozi's cooling dummies, one was modified by fitting a cylindrical electrical aquarium heater at its core to expedite rewarming at the end of a cooling experiment. The modified cooling dummy exhibited a 3-hour PMTP after incubator preheating, as expected. However, it failed to produce a PMTP after its core was preheated to 37°C using its internal aquarium heater. That observation was unexpected, and initially Mfolozi had no explanation for it. As far as he was concerned, all known experiment parameters that had previously caused a PMTP to appear had not been altered: the modified cooling dummy's core temperature was 37°C in both instances at death, and the ambient air temperature was also the same in both instances. At the time of the study, there was no description in the literature of a study in which a body that had previously demonstrated a PMTP failed to demonstrate it under certain conditions. Causing the PMTP to disappear was not the intention of his study.

To explain this observation, Mfolozi placed a thermometer sensor on the skin of the modified cooling dummy followed by preheating in the incubator. Incubator preheating caused uniform body temperature – both the skin and deep core temperature was 37°C at death. Precipitous lowering of skin temperature occurred after removal from the incubator (death), while core temperature remained 37°C for the 3 hours afterwards. Mfolozi surmised that rapid skin cooling caused cooling of a thin layer of the body immediately beneath the skin, which itself caused cooling of an even deeper body layer, and so on, in a domino effect. This sequential cooling process thus propagated away from the skin towards the core, and was sustained by continued cooling of the skin. The cooling process continued as long as a temperature gradient existed between the skin and the core. Mfolozi surmised that the cooling process propagated slowly due to thermal properties of the body. The cooling process eventually reached the core 3 hours after death, where it caused core cooling. Mfolozi concluded that it was the 'delayed propagation of this sequential cooling process' that caused the PMTP. The prerequisite was that core and skin temperatures at death had to be both high.

To explain absence of the MPTP, Mfolozi preheated the modified cooling dummy's core to 37°C using its internal aquarium heater and then recorded core and skin temperatures after switching off the aquarium heater (death). The skin sensor indicated that skin temperature was already low at death (15° C). The core thermocouple probe recorded the highest rate of cooling precisely when the PMTP was expected on the cooling curve, which also lasted for exactly 3 hours. Mfolozi surmised that absence of the PMTP in that experiment, which was replaced by the most rapid core cooling rate, was the result of the hot core being surrounded by a cold body as indicated by the skin sensor. In other words, the magnitude and direction of temperature difference between the core and skin, alternatively referred to as the antemortem axial temperature distribution in this thesis, is the entity that predicted presence or absence of the PMTP. Body core temperature at death on its own was not sufficient as a predictor. At the time of the study, the Rectal Temperature Nomogram method applied a single-point body core thermometry value measured rectally from a dead body at an unknown PMI. No death-time estimation method quantified the antemortem magnitude and direction of temperature difference between the core and skin.

Mfolozi appreciated that postmortem heat transfer occurred from the body core through the body bulk by thermal conduction to the skin, and from the skin to the environment through thermal conduction, thermal convention, and thermal radiation. He also appreciated that coldness, like darkness, was not a physical entity. Nonetheless Mfolozi imagined the hypothesised sequential cooling process responsible for the PMTP to be a measurable thermal event, and because it evidently propagated in a direction opposite to heat flow, he imagined it was a wave having an amplitude equal to the core-surface temperature gradient at death. Mfolozi therefore called it the ‘core-surface temperature gradient wave’, with which he further hypothesised that:

- the axial thermometry-depth was directly proportional to PMTP length within a given body.
- when the ratio of thermometry-depth to body radius was standardised among different bodies, body radius was directly proportional to PMTP length.

- no PMTP would be recorded at any location in the body if thermometry was undertaken at that location after the ‘wave’ had already reached that location. In other words, the PMTP length was inversely proportional to the PMI (time from death to thermometry).
- the postmortem thermal-core, generally regarded to be a static entity, was gradually shrunk axially by the ‘wave’ and therefore was not static; and
- the position of the postmortem thermal-core was influenced by thermophysical properties of the ground (temperature, density, thermal conductivity, thermal capacitance). Accelerated skin cooling caused by a cold surface shifted the postmortem thermal-core away from the ground.

Mfolozi was concerned by absence of these hypotheses in forensic / postmortem cooling / death-time estimation literature. To him, his hypotheses suggested that:

1) thermometry-depth should be standardised in death-time estimation methods that used a core temperature measurement, yet no method did this at the time.
2) body radius should be incorporated in death-time estimation methods that used a core temperature measurement, yet no method did this at the time.
3) thermophysical properties of the ground-surface should be incorporated in death-time estimation methods that used a core temperature measurement, yet no method did this at the time; and
4) axial temperature distribution at death should be formally approximated for a body and applied in death-time estimation, yet no method did this at the time.

Mfolozi's hypotheses proved to be the turning point in his master's research. They abruptly transformed his research from being a regular forensic pathology problem to being a heat transfer problem. At the time of the study, Mfolozi had no formal or informal training or qualification in mechanical engineering. Midway through his research, Mfolozi conducted a second literature review on heat transfer and discovered that mechanical engineers were already familiar with hypothesised heat transfer process – Fourier's Law. Mfolozi acknowledged this in his dissertation. Mfolozi appreciated that further research on postmortem heat transfer was required to better understand PMTP causes so that a method of death-time estimation that avoided PMTP uncertainties could be developed. Mfolozi concluded his master's dissertation without deriving corrective factors for the Henβge Rectal Temperature Nomogram method as originally planned. He graduated in 2013. His examiners encouraged him to continue his research by pursuing the degree of Doctor of Philosophy in Forensic Pathology, advice he heeded. Two years prior to graduating, Mfolozi obtained a Fellowship in Forensics Pathology from the Colleges of Medicine of South Africa (CMSA) and became a qualified specialist forensic pathologist. In 2014 he registered for the degree Doctor of Philosophy in Forensic Pathology at the University of Cape Town through the Faculty of Health Sciences. He requested and received supervision, support and guidance from the Faculty of Mechanical Engineering and Built Environment of the University of Cape Town.

Bibliography and References Cited

1. Henβge C (1988). Death time estimation in casework. I: the rectal temperature–time of death nomogram, Forensic Sci. Int. 209-266.

2. Mfolozi S (2013). Cooling rates of dummies under various degrees of air humidity, wind speed and air temperature. Masters dissertation. University of Cape Town.

3. Mfolozi S (2011). WO2012017300A1. Apparatus for estimating the post-mortem interval of a corpse.

4. Apparatus for estimating the post-mortem interval of a corpse (2013). South African Patent Journal: 2 (46), 134.

5. Marshall TK, Hoare FE (1962). Estimating the time of death. The rectal cooling after death and its mathematical expression. Journal of Forensic Science, 56-81.

CHAPTER 2

Research aims, objectives and setting

Chapter 2

Research aims, objectives and setting

2.1 Research Aims

The overarching goal of this PhD research was to contribute towards advancing the science of thermometric death-time estimation. The research aims of this thesis were:

2.1.1 To understand postmortem axial heat transfer in the human body, particularly during the PMTP period (to prove/disprove the author’s mater’s dissertation hypotheses).

2.1.2 To apply that understanding to develop a method of death-time estimation free of PMTP uncertainties.

2.2 Research Objectives

Primary objectives, as set out at prior to beginning of this research, were:

2.2.1 To apply numerical analysis as a method of choice for studying axial heat transfer in the human body during postmortem cooling. Proprietary numerical analysis software often consists of a post-processing visualization tool that the author hoped to exploit to demonstrate his ‘wave hypothesis’, even after becoming aware of Fourie’s Law. This objective therefore defined one of the research methods.

2.2.2 To apply a high anatomical-fidelity 3D computational phantom as a human surrogate in the intended numerical analysis. The belief was that a better understanding of postmortem axial heat transfer could only occur if the 3D computational phantom was as geometrically consistent as possible with human anatomy in terms of organ size, organ shape, organ position, and organ relations. The author hoped to improve on 3D computational phantoms used by Mall and Eisenmenger[1,2,] Schenkl et al[3] and Weiser et al[4], all of which consisted of just 14 organ-domains. This objective therefore defined one of the research materials.

2.2.3 To propose separation of numerical approximation of antemortem temperature distribution from numerical estimation of the postmortem interval. The belief was that such separation would help define the moment of death. Another motivation for the separation was to demonstrate that the PMTP can be demonstrated in numerical simulation without using deliberate methods such as application of a calibrated decrease-rate of heat production used by Mall and Eisenmenger [1,2]. In other words, separation was intended to demonstrate that supravital energy production was not a cause of the PMTP. A third motivation was the belief that separation would allow systematic approximation of the antemortem total-body temperature distribution not comingled with postmortem cooling simulation.

2.2.4 To numerically estimate the antemortem temperature distribution by applying organ-specific metabolic rates and organ-specific blood perfusion rates (collectively referred to in this thesis as *biothermal parameters*), in preference to the approach adopted by Mall and Eisenmenger [1,2] of apportioning fixed percentages of the calculated power-mass density value to various organs and body regions. Databases of organ-specific biothermal parameters exist, and the author felt that the organ blood perfusion and metabolic rates do not restrict themselves to fixed percentages. The secondary aim was to apply these parameters and assess results with known antemortem temperature distribution patterns as described in the literature.

2.2.5 To apply the solution of a numerical analysis that predicted antemortem temperature distribution in initial conditions of a numerical analysis that simulates postmortem cooling by natural convection and thermal radiation only, i.e. without thermal conduction to the environment. This study was to form a baseline simulation against which later simulations under altered cooling conditions would be compared. Post-processing tools would be used to visualise postmortem heat transfer in the axial plane to confirm or refute the author's mater's dissertation hypotheses about causes of the PMTP.

2.2.6 To apply the solution of a numerical analysis that predicted antemortem temperature distribution, as described in item 2.2.4 above, in initial conditions of a numerical analysis that simulates postmortem cooling by natural convection, thermal radiation *and* thermal condition with a cold ground-surface. This study would prove or refute the author's master's degree hypothesis that temperature and thermophysical properties of a ground-surface modify the rate of postmortem cooling and result in shifting of the postmortem central isotherm relative to the ground. The study would demonstrate that the ground-surface was not an infinite heat-sink that did not need to be modelled in the simulation, as asserted by Mall and Eisenmenger [1,2]. This study would apply the numerical analysis described in 2.2.5 above as the baseline simulation for comparing effects of temperature and thermophysical properties of a ground-surface.

2.2.7 To apply the solution of a numerical analysis that predicted antemortem temperature distribution, as described in item 3.2.4 above, in initial conditions of a numerical analysis that simulates postmortem cooling by natural convection, thermal radiation and thermal condition with a heated ground-surface. The aims of this objective to prove the effects of high temperature of a ground-surface on the rate of postmortem cooling and shift of the postmortem central isotherm.

Secondary aims and objectives were defined as those formulated during the course of the study as informed by results and conclusions of ongoing research to meet primary objectives. To this end, the secondary aim was to propose measurement of postmortem axial isotherms as a new thermometry procedure that reduces uncertainties associated with the PMTP. Secondary objectives were therefore:

2.2.8 To design and fabricate a multipoint axial thermometry device, whose application in death-time estimation is unprecedented.

2.2.9 To explore technical and logistical considerations of multipoint axial thermometry in the human body in the context of death-time estimation using numerical analysis.

2.2.10 To propose a numerical protocol of death-time estimation that applies axial isotherm thermometry.

2.2.11 To exploit the nature of the proposed numerical protocol of death-time estimation to apply temperature measurements from a periodic historical meteorological record from the nearest weather station.

2.2.12 To demonstrate application of the proposed protocol.

2.2.13 To explore theoretical sources of uncertainty of the proposed protocol.

2.3 Setting

All the studies were performed while Sipho Mfolozi was a registered PhD candidate of the University of Cape Town between the years 2014 and 2020.

IT'IS Foundation & University of Cape Town (UCT) Research Contract

The University of Cape Town and IT'IS Foundation, Switzerland, formally entered into a research contract in which the University of Cape Town was granted an academic licence to use Virtual Family v1.x 3D computational phantoms (Ella, Duke, Billie, Thelonious). The contract, by extension, also included licence for use of the multiphysics solver called Sim4Life® by Zurich Med Tech, Switzerland.

2.4 Chronology of studies

Chapter 6

Mfolozi S, Malan AG, Bello-Ochende T, Martin LJ. Numerical approximation of total-body temperature distribution at death.

The aim of this study was to demonstrate numerical analysis of antemortem temperature distribution in a high-definition anatomically segmented 3D computational phantom by applying organ-specific biothermal parameters. The solution of the analysis would constitute initial conditions numerical analysis in chapter 5 that simulated postmortem cooling.

Chapter 7

Mfolozi S, Malan AG, Bello-Ochende T, Martin LJ. Numerical analysis of postmortem axial heat transfer.

The aim was to study axial heat transfer during simulated of postmortem cooling of a high-definition anatomically segmented 3D computational phantom in air, on cold concrete and on a heated surface. The aim was to prove the many hypotheses by Mfolozi[5] regarding the PMTP and the central postmortem isotherm.

Chapter 8

Mfolozi S, Malan AG, Bello-Ochende T, Martin LJ. Multipoint axial thermometry.

The aim was to propose multipoint axial thermometry for death-time estimation and demonstrate it empirically and numerically using a proposed propose multipoint axial thermometry device.

Chapter 9

Mfolozi S, Malan AG, Bello-Ochende T, Martin LJ. A Numerical Protocol for Death-time Estimation

The aim was to propose a numerical protocol of death-time estimation that applied multipoint axial thermometry iterative comparison and representative historical meteorological data.

Chapter 10

Mfolozi S, Malan AG, Bello-Ochende T, Martin LJ. Limitations and sources of uncertainty.

The aim was to discuss limitations and sources of uncertainty arising from the proposed numerical protocol

Chapter 11

Mfolozi S, Malan AG, Bello-Ochende T, Martin LJ. Conclusions. The aim was to discuss the potential impact of the proposed protocol to the science of death-time estimation as well as for future research.

2.5 Outline of thesis

In **Chapter 1** an introduction and background are presented in which the motivation for this thesis is given.

In **Chapter 2** research aims, objectives, setting and thesis coherence are provided.

In **Chapter 3** a bibliographic review of thermometric death-time estimation methods relevant to this thesis is presented.

In **Chapter 4** a bibliographic review of bioheat modelling methods is presented.

In **Chapter 5** research materials and methods are presented.

In **Chapter 6** a numerical method to approximate antemortem body temperature distribution using an anatomically segmented 3D computational phantom and organ-specific metabolic and blood perfusion rates is presented and results analysed.

In **Chapter 7** numerical analysis of postmortem axial heat transfer is undertaken using a high-definition anatomically segmented 3D computational phantom cooling in air, on cold concrete and on a heated floor.

In **Chapter 8** multipoint axial thermometry is proposed and demonstrated empirically in a cooling dummy and numerically in a 3D computational phantom using a proposed multi-point axial thermometry device.

In **Chapter 9** a numerical protocol for death-time estimation that applies iterative multipoint axial thermometry comparisons is proposed and demonstrated.

In **Chapter 10** sources of uncertainty and limitations of the proposed numerical protocol are discussed.

In **Chapter 11** concluding remarks regarding the impact of this thesis to the science of death-time estimation and to future research are given.

2.6 Coherence of the thesis

I (Sipho Mfolozi) am the author of all ten chapters of this thesis and was the lead investigator in all studies. The chapter 6 study forms the basis for the chapter 7 study. The chapter 7 study forms the basis for proposal of the device described in chapter 8. Studies in chapter 7 and chapter 8 form the basis for proposal of the numerical protocol described in chapter 9. Chapter 10 discusses potential sources of error of the protocol proposed in chapter 9. Chapter 11 provides concluding remarks of the thesis. Professor Arnaud George Malan, Professor Tunde Bello-Ochende and Professor Lorna Jean Martin jointly supervised the studies while I was registered as a student at the University of Cape Town, South Africa, which overlapped with my employment as the Head of Department of Forensic Medicine by the University of KwaZulu-Natal, South Africa. All computational studies applied the same research materials and methods.

Bibliography and References Cited

1. Mall G, Eisenmenger W (2005). Estimation of time since death by heat-flow Finite-element model part I: method, model, calibration, and validation. Legal Medicine, 1-14.

2. Mall G, Eisenmenger W (2005). Estimation of time since death by heat-flow Finite-element model part II: application to non-standard cooling conditions and preliminary results in practical casework. Legal Medicine, 69-80.

3. Schenkl S, Muggenthaler H, Hubig M, Erdmann B, Weiser M, Zachow S, Heinrich A, Güttler FV, Teichgräber U, Mall G (2017). Automatic CT-based finite element model generation for temperature-based death time estimation: feasibility study and sensitivity analysis. International Journal of Legal Medicine, 699-712.

4. Weiser M, Erdmann B, Schenkl S, Muggenthaler H, Hubig M, Mall G, Zachow S (2017). Uncertainty in temperature-based determination of time of death. Heat and Mass Transfer, 2815-2826.

CHAPTER 3

Bibliographic review of death-time estimation methods

Chapter 3

Bibliographic review of death-time estimation methods

3.1 Preamble

Death-time estimation plays an important role in the justice system of many states in modern society. It is a forensic pathology subspecialty that involves multiple sciences as climatology, meteorology, microbiology, entomology, taphonomy, anthropology, molecular biology, biochemistry, and others. Evidence used for death-time estimation may come from three sources:

a) Anamnestic Evidence, that which is based on the decedent's day-to-day habits, activities, and routines. This evidence is often gathered from family, relatives, neighbours, employees, co-workers, financial transactions, closed-circuit television (CCTV) surveillance footage, cellular telephone activity and mapping, etc. Collection of anamnestic evidence is generally the responsibility of law enforcement agencies.
b) Environmental Evidence, that which is present in the vicinity of the decedent's body. Securing and preserving this type of evidence is also generally the responsibility of law enforcement agencies, although it may be of interest to sciences like forensic entomology.
c) Corporal Evidence, that which is present on and in the body. This type of evidence is generally the responsibility of medical practitioners such as

medical examiners, coroners, and forensic pathologists, who generally have jurisdiction over the body.

Corporal evidence may manifest in the body either during the so-called *early postmortem period*, which is from death to about 3 days, or the *late postmortem period*, which has no time limit. Bodily changes that occur in the early postmortem period used for PMI estimation include phenomena as body-cooling; rigor mortis[1]; livor mortis[2]; biochemical alterations[3] in natural body-cavity fluids (vitreous humour, pleural fluid, cerebrospinal fluid, synovial fluid); stomach emptying[4]; postmortem electrical excitability of skeletal muscles[5]; protein-based approaches[6] and multiple other changes. These phenomena are subjects of continuous research and evolved into distinct sub-specialities under the general umbrella of 'Death-time Estimation'. Fig. 3.1 depicts the general classification of death-time estimation literature and methods. This thesis falls under the category of '*body-cooling'*, and no further reference to the other categories shall be made. Similarly, methods of death-time estimation based on bodily changes that appear in the late postmortem period, e.g. putrefaction, mummification, adipocerification, tissue breakdown by insects/scavengers, skeletonization and fossilization, are not relevant to this thesis.

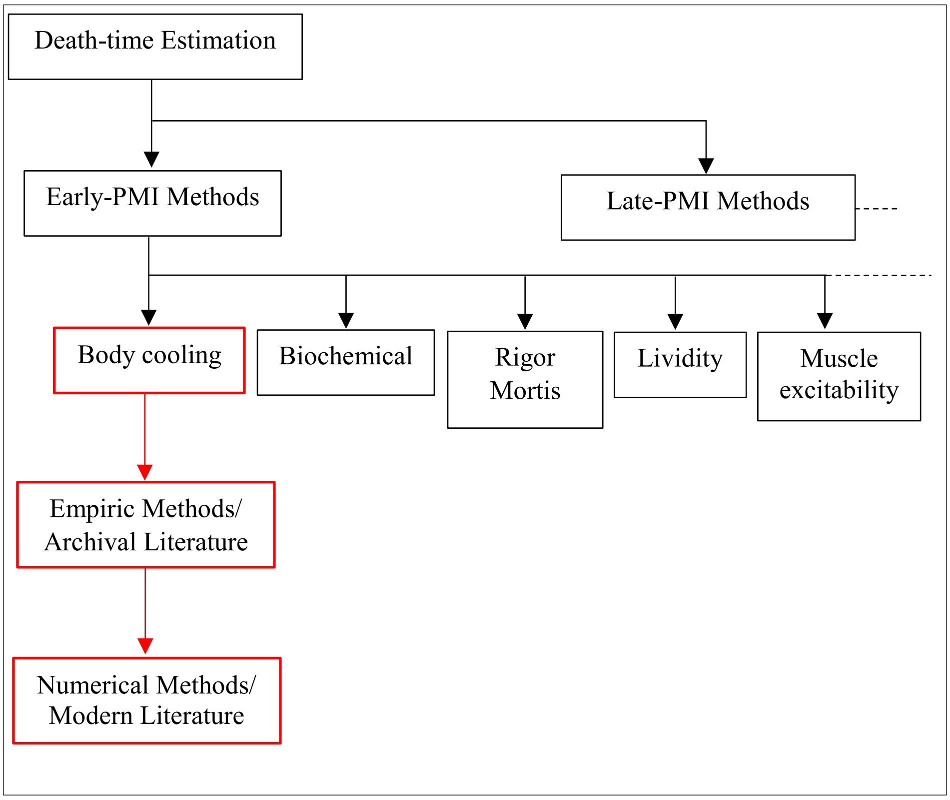

Fig. 3.1 – A general classification of death-time estimation literature and methods. Red boxes indicate literature this thesis is limited to.

3.2 Current knowledge, critical questions and challenges related to thermometric death-time estimation

Body-cooling methods of death-time estimation can generally be divided into two categories, namely empiric and numerical/mechanicalistic methods. Empiric methods apply one or other empirically derived mathematical expression of body-cooling to calculate the body's cooling time using an assumed antemortem body temperature value, together with a body temperature measurement made by an investigator at an unknown PMI. Numerical methods, on the other hand, apply laws of physics on a 3D computational phantom that represents the dead human body to mathematically model heat transfer by thermal conduction, convection, and radiation. Numerical methods therefore allow more variables that affect postmortem cooling to be included. This thesis falls under the 'numerical methods' category. Numerical methods can therefore be considered state-of-the-art because they advance on empiric methods, although the two categories still coexist in practice today and have some continuity and overlaps.

Subsections discussed in the next few pages are a synthesis of ten subjects considered by the author to represent current knowledge, critical questions, and challenges in thermometric death-time estimation relevant to this thesis.

3.2.1 Postmortem rectal cooling is characterised by the PMTP

Postmortem cooling has been known to occur in the human body since before time immemorial. Beginning in the 19th century, postmortem cooling was noted to be characterised by a lagging of internal visceral cooling several hours after death. Authors such as Davey[7], Rainy[8], Schwarz and Heidenwolf[9], Sellier[10], de Saram et al[11], Marshall and Hoare[12] and Henβge[13] observed this phenomenon either at autopsy or during rectal thermometry. Core temperature time-curves in the first stages of postmortem cooling exhibited a sigmoid double-exponential shape caused by initial slow rate of cooling. This delayed core cooling became known as the postmortem temperature plateau (PMTP) and appeared inconsistent with Newton's law of cooling[14], would have otherwise been applied to calculate the PMI and settle the matter. Appearance of the PMTP varied among different studies. Some authors[15,16,17,18,19,20] did not observe it in their subjects. The author of this thesis believes that variations of the PMI before thermometry was commenced in those studies were partially responsible for the PMTP's unpredictability.

Erstwhile rule-of-thumb methods of death-time estimation, including those described by Burman[21], Rainy[8], Womack[22], Rhodes et al[23] and Simpson[24], did not feature the PMTP in their description. These methods were thus criticised by subsequent authors as being suboptimal[25]. The practice of addition of an arbitrary fixed time-value that represents the PMTP in a proposed method of death-time estimation, e.g. standard addition of 45 minutes by the de Saram et al[11] method, was also criticised as being suboptimal[26]. Other methods of death-time estimation that included the PMTP were described. One was the so-called Triple Exponential Formula (TEF) method by Al-Alousi et al[18,19], which he devised for his proposed microwave thermometry method. The TEF consisted of three exponential terms corresponding to the three cooling stages: namely the PMPT, the fast cooling phase following the PMTP and the slow cooling phase towards the end of cooling. Each exponential term consisted of two parameters whose description was nonetheless not provided. Temperature-curves plotted using Al-Alousi's microwave thermometry did not show a PMTP. Al-Alousi attempted to correlate cooling factors of each body site with body parameters such as weight, height, surface area, hip width, head circumference, and cooling size (surface area/weight), all with little success. The exception was that thin and fat bodies could be distinguished using rectal temperatures.

Marshall and Hoare[12] mathematically expressed rectal cooling using a so-called 'Cooling Formula' that consisted of two exponential terms, the second of which represented the PMTP. Marshall pointed out that using average values for the constants in the Cooling Formula (including constants of the PMTP exponential term) did not enable the TOD of a body found dead to be determined with a satisfactory degree of accuracy, unless the constants were determined specifically for that body concerned. In other words, cooling-formula constants that enable accurate death-time estimation are specific to a given body found dead and therefore must first be solved for.

3.2.2 No consensus on PMTP causes

The logical next step after Marshall and Hoare's Cooling Formula was description of a method of solving for Cooling Formula constants, including the PMTP-value of a given body, which would then neatly be applied into the Cooling Formula to estimate the PMI. For that to occur, causes of the PMTP first needed to be well understood. Several explanations were offered by various authors before and after the Cooling Formula was described. Rainy[8] had stated that gradual cessation of the calorific process/postmortem supravitality and decomposition played a role in retarding cooling in the early postmortem period. Lundquist[27] had suggested postmortem heat generation by glycolysis (glucose breakdown) in muscle over several hours. Shapiro[25] had thought that cooling in the centre of the body was delayed until a temperature gradient was established by conduction from the body centre to the body periphery. Sellier[10] had thought that the PMTP could be explained purely by elemental physical considerations, specifically the existence of a temperature gradient, pointing out that body radius had much more influence on the shape of the postmortem cooling curve than cooling conditions. Joseph and Schickele[28] had attributed the PMTP to a small temperature gradient that exists at the core, also emphasising the significance of body radius. Brown and Marshall[29] suggested that internal conductivity and thermal capacity of the human body retarded cooling of the core. Nokes et al[30] suggested that anaerobic glycogenolysis (glycogen breakdown) was responsible for maintaining a temperature equilibrium shortly after death, and that the PMTP depended on environmental temperature, surface insulation and body size. Nelson[31] stated that anaerobic respiration, cell lysis, chemical processes, bacterial activity, and rigor mortis all contributed to causing the PMTP. Smart and Kaliszan[32] stated that the appearance of the PMTP was random and could not be predicted, citing inter-individual differences in states such as core body temperature, hyperthermia, drugs, trauma, and biomarker concentration.

The author[33] in 2013 hypothesised that:

A) The PMTP would be longest at the core when body temperature was uniform at death, but would be absent if at death the core was warm but the body around it was cold,

B) The PMTP would be recorded as being the longest in a body with an initially uniform temperature distribution when thermometry was at the core. PMTP would be recorded as being progressively shorter and eventually absent as thermometry-depth reduced towards the skin,

C) Core thermometry of a body whose temperature was uniform at death would result in the longest PMPT being recorded if the thermometry was commenced at death. The PMTP would be recorded as being progressively shorter if thermometry was commenced at increasingly longer PMIs,

D) The PMTP of a body with a larger circumference (body radius) would be longer than that of a body with a smaller circumference (body radius) when core thermometry was commenced at death in both instances.

The author opined that variation in the combination of these 5 factors resulted in the apparently unpredictable nature of the PMTP among different bodies.

This thesis demonstrates the true nature and cause of the PMTP phenomenon. The thesis proposes a numerical method of death-time estimation that avoids its uncertainty.

3.2.3 No method to solve for the PMTP value of a given body found dead

While the debate of PMTP causes continued, Henβge[34] empirically determined a strong correlation of the value of the cooling constant "A" in Marshall and Hoare's Cooling Formula with body-mass to the power of –0.625. Using that correlation, Henβge described the so-called Rectal Temperature Nomogram method[35,36] that applied body mass and corrective factors for cooling conditions that differ from standard conditions, e.g. clothing and air-flow over the body. The Rectal Temperature Nomogram method became the widely accepted method of death-time estimation as it was relatively simple to use. It appeared to acceptably negate the need for solving for a given body's specific PMTP-value by applying body mass and corrective factors. The Rectal Temperature Nomogram method reportedly had a 95% permissible variation of the estimated PMI in hours and was verified by a number of studies[37,38,39,48,49].

None of the PMTP causes suggested by the various authors manifested in the development of a method for solving for a given body's specific PMTP-value as envisioned by Marshall and Hoare's Cooling Formula. As stated in 3.2.2, the time between death and thermometry of a body found dead (i.e. its PMI), the very factor solved by the Cooling Formula, also predicted the measured PMTP value of that body. The author therefore believed that it was not practically possible to completely solve for all Cooling Formula constants that describe the PMTP value of a given body found dead, as envisaged by Marshall, unless the dead body was rewarmed to its initial condition at death and then re-cooled in identical conditions.

The PMTP debate appeared to subside after the Rectal Temperature Nomogram method was proposed , although work continued for alternative death-time estimation methods that avoided the PMTP problem altogether, e.g. outer ear thermometry methods by Kinawaku[20] and Baccino et al[40]. As this thesis demonstrates in later chapters, the PMTP-value of a given body depends on multiple factors and the PMTP-value may vary for a given PMI in the same body.

This thesis proposes a numerical protocol of death-time estimation that is free of the PMTP uncertainty.

3.2.4 Assumptions and approximation of antemortem body temperature

Rectal temperature empiric methods of death-time estimation, such as Marshall's Cooling Formula and the Henβge Rectal Temperature Nomogram method, operate on the assumption that antemortem body temperature is represented only by the body core having a temperature of 37°C. However, the living human body is generally accepted under normal conditions to consist of a cooler outer shell and a hot core. Outer shell temperature is therefore disregarded. Effects of antemortem body temperature on the rate of subsequent postmortem cooling were highlighted by Schwarz and Heidenwolf[9]. The requirement for accurate approximation of antemortem body temperature was pointed out by Al-Alousi et al[18], particularly in relation to his microwave thermometry method. To approximate antemortem body temperature, Al-Alousi suggested averaging of temperature values at death to be used for the brain, liver, and rectum (naked and covered) based from their results. In erstwhile postmortem cooling studies, a number of authors stated that they excluded cases whose body temperatures before death were outside normal parameters[26], without explaining how or when body temperatures were measured. Other authors simply did not report antemortem body temperatures of their subjects.

The author's 2013 study demonstrated that the temperature of the body-bulk between the core and skin played a significant role on the rate of cooling of the core. The suggestion from that study was that antemortem axial temperature must be approximated. In more general terms, the author's 2013 study highlighted the impact a more complete understanding of PMTP causes has on appreciation of other aspects of death-time estimation not previously considered to be sources of uncertainty.

By their nature, empiric methods of death-time estimation do not possess the capability for approximation of antemortem body temperature, hence their reliance on a pre-approximated core temperature value. Numerical methods, on the other hand, have to state the initial temperature field of the 3D computational phantom used as a human body – the initial condition – before simulation of postmortem cooling. Different authors of numerical methods employed varying strategies to perform this approximation.

In the heat-flow Finite Element Model (FEM) by Mall and Eisenmenger[41,42] the initial temperature distribution of the 3D computational geometry's skin was approximated from 37°C by a linear gradient down to 27°C on the surface layers of the distal extremities. The heat-flow FEM included 'internal power' as a boundary condition intended to represent a production of thermal energy within the body by supravital reactions in the phase of intermediary life. Production of thermal energy by supravital reactions in the phase of intermediary life was a concept theorised by Rainy[8], de Saram et al[11], Lundquist[27], Nokes et al[30], Nelson[31] and Smart[32] to be a cause of the PMTP, as stated in the previous sections. Although Mall and Eisenmenger did not explicitly use the word 'PMTP', the author of this thesis believes that 'internal power' and its calibrated decrease-rate reported to correlate with estimates by Lundquist were designed to induce a PMTP in the FEM.

To simulate the inhomogeneous temperature distribution that exists in life between the core and shell in their heat-flow FEM, Mall and Eisenmenger converted the approximated basal metabolic rate related to body mass into a power-density value – 60% of it was apportioned to the body core (mediastinum, lungs, upper abdominal organs, gastrointestinal organs, kidneys and pelvic organs); 18% to the muscle compartment; 17% to the brain and 5% to bone and connective tissues of the face and neck. They applied this approach as a process separate from that of 'internal power' and its calibrated decrease-rate.

Another numerical study in which antemortem temperature was approximated was performed by Schenkl et al[43]. They applied a second-order homogenous partial differential heat equation to define the initial temperature field at death of their CT-derived computer model.

Another numerical study that approximated antemortem temperature was described by Weiser et al[44]. They approximated the initial temperature field of a CT-derived phantom similar to that described by Schenkl et al by application of the Pennes bioheat equation, but without providing further information about resultant organ temperatures. Weiser also adopted the 'internal power' method described earlier by Mall and Eisenmenger to represent perimortem thermogenesis by supravital reactions. Numerical methods described by Mall and Eisenmenger[41,42], Schenkl et al[43] and Weiser et al[44] undertook numerical approximation of the initial temperature field of the body as a continuation of numerical simulation of postmortem cooling.

The numerical method of death-time estimation by Wilk et al[45] assigned a uniform initial body temperature of 37°C to the 3D computational phantom.

This thesis proposes formal separation of the two processes, as well as application of metabolic and blood-perfusion rates to individual organ domains using parameters from the literature to simulate antemortem thermogenesis. This thesis demonstrates that abrupt cessation of organ thermogenesis at death produces a nearly 4-hour long PMTP without simulation of any supravital or postmortem thermal reactions.

3.2.5 Effect of cooling surfaces on postmortem cooling

Types of ground surfaces on which postmortem cooling observed by authors were diverse. For example, typically reported postmortem cooling surfaces included wood[7,12,15,26,46], cement[11], metal[11,13,18,19], rubber[15] and bed[21,47]. Many other authors did not specify the type of cooling surface, while others simply stated that it was 'thermally neutral'. Even in studies that reported the cooling surface, the exact postmortem cooling conditions that preceded the study, which would have included the cooling surface, were always not reported.

Several other authors however appreciated the effect of the cooling surface on postmortem cooling. Taylor and Wilks[47] theorised that thermal conductivity of a ground-surface affected the rate of postmortem cooling. 'Standard conditions' of postmortem cooling, which were adopted in controlled observations, were defined as a naked body in the supine position on a thermally neutral surface in constant-temperature air with no wind and no strong thermal radiation[13,34,48,49]. The thermal neutrality of the surface was however not defined in terms of thermophysical properties, which of course influence the rate of heat transfer as some surfaces conduct heat better than others.

Empiric methods of death-time estimation such as the Cooling Formula and the Rectal Temperature Nomogram method do not incorporate thermophysical properties of a given cooling surface in their estimation of the PMI. Numerical methods of death-time estimation on the other hand deal with ground-surfaces in a variety of ways. The heat-flow FEM by Mall[41] modelled the temperature of ground-surface on which the 3D computational phantom was placed to be equal to ambient air temperature, but its thermophysical properties were not mentioned and the ground surface itself was not modelled. The 3D computational phantom was in contact with the ground-surface on its entire posterior aspects involving the head, chest, and abdominal regions, which were flattened. In the author's experience, a naked supine body comes into contact with a cooling surface only at body regions that exhibit contact-pallor. In applying the heat-flow FEM to five real-world cases[42], the ground was assumed to represent an infinite thermal reservoir that rapidly conducted the warmth coming from the body. That assumption was regarded as convenient because the cooling surface then didn't need to be modelled by finite elements itself, provided the nodes of the 3D computational phantom were kept touching the ground fixed at a constant environmental or ground temperature.

This thesis will demonstrate that the ground may not always be an infinite heat-sink and that its temperature and thermophysical properties may affect the rate of postmortem cooling as well as the location of the postmortem central isotherm. The two factors would both affect the measured single-point core temperature value and hence accuracy of the PMI estimated by empiric methods. To be safe, this thesis proposes numerical modelling of the ground-surface using appropriate material property values to an extent that is practically possible.

3.2.6 Non-standardisation of the relative rectal thermometry-depth

As stated in the previous subsections, several authors[10,25,28,50,51] pointed out the role body radius played in predicting the shape of the postmortem core cooling curve with reference to the PMTP. The author had hypothesised in 2013 that bodies of larger radius would exhibit a longer PMTP and vice versa. The author had also hypothesised that different thermometry-depths in a given body at a given PMI would yield different single-point temperature measurements, which would then result in different PMI estimates by empiric methods.

The literature indicates wide variation in thermometry-depth and anatomical sites of thermometry among various studies of postmortem cooling. The rectal thermometry-depth used by Schwarz and Heidenwolf[9] was 12cm. The rectal thermometry-depth used by de Saram et al[11] was 3 to 4 inches (7.62 to 10.16cm) into the anal sphincter. The rectal thermometry-depth used by Hensβe[34] was 8cm beyond the anal sphincter. The tracheal thermometry-depth used by Nokes et al[52] was 25cm into the nostril. The microwave thermometry method of Al-Alousi[18,19] had a wavelength of around 9cm and was said to be able to penetrate distances of several centimetres though the tissue.

Standardisation of relative thermometry-depth is evidently necessary to ensure uniformity among bodies of different radii. Neither empiric nor numerical methods of death-time estimation standardise thermometry-depth today. This thesis proposes a thermometry method that inherently standardises thermometry-depth. At the end of simulated postmortem cooling, numerical methods[41,42,43,44] routinely extract body temperature from the deep rectum of the 3D computational phantom for comparison with the rectal temperature measured from the dead body. However, numerical methods do not extract rectal temperature at the same body-radius thermometry depth used in the dead body.

This thesis proposes a device and numerical protocol for death-time estimation in which standardization of relative thermometry depth occurs automatically.

3.2.7 Anatomical fidelity of 3D computational phantoms of numerical methods

Numerical methods of death-time estimation apply 3D computational phantoms as human body avatars. Anatomical fidelity of these phantoms ensures representativity of the simulation to the physical postmortem heat transfer processes that affected a decedent's body. Anatomical fidelity of 3D computational phantoms used in numerical death-time estimation methods ranges from simplistic to highly complex.

The 3D computation phantom of the heat-flow FEM method[41,42] was manually meshed and of low anatomical fidelity, consisting of 8328 solid cuboidal elements and 10154 nodes. Elements and nodes increased with inclusion of the ground. The FEM phantom consisted of 14 tissue compartments whose anatomical segmentation into constituent organs was low.

The CT-derived 3D computational phantom proposed by Schenkl et al[43] and by Weiser et al[44] was obviously built from CT images of a human body. However, it too consisted of 14 tissue compartments whose anatomical segmentation into constituent organs was low.

The 3D computational phantom used by Wilk et al[45] for numerical death-time estimation using non-invasive thermometry had very low anatomical fidelity. It consisted of cones representing arms and legs, an ellipsoid representing the head, and cylinders representing the neck and torso. Its proportions were dictated by standardized anatomical measurements and it consisted of just 2 tissue compartments, namely body fat and non-adipose tissue.

This thesis proposes use of a class of high-fidelity, high-definition, anatomically segmented 3D computational phantoms of varying age, sex, weight, and height as human body surrogates for numerical death-time estimation.

3.2.8 Application of historical meteorological data in death-time estimation

Ambient air temperature affects the rate of postmortem heat transfer by thermal convection. Many studies of postmortem cooling often recorded the surrounding air temperatures during observations. In some instances, the air temperature was mechanically controlled in the mortuary environment. Almost all empiric methods of death-time estimation required an ambient temperature value. The Hensβe Rectal Temperature Nomogram method advised averaging of air temperature values from historical meteorological data of the nearest weather station. Averaging air temperatures faces two main challenges:

A. The interval over which air temperature values to be averaged existed is required. For a body found dead, this interval is the body's PMI. It is therefore illogical for the PMI of that body to be required for calculating an average air temperature that is then used to estimate that body's PMI. The PMI applied in the averaging calculation might as well be regarded as *the* PMI and the averaging and/or death-time estimation need not be carried out. The author therefore believed that certainty of an averaged air temperature value applied in an empiric method was not possible as long as the PMI was the unknown.

B. Averaging may erroneously be performed only for air temperature values and not of their duration. High air temperature values that existed for shorter periods would be over-represented.

This thesis proposes a method of applying historical meteorological air temperature measurements that existed between death and thermometry (i.e. during the PMI of a body found dead) in the correct sequence and duration they existed, without requiring prior knowledge of the very PMI being estimated.

3.2.9 Death-time estimation using single-point thermometry

With the exception of the skin-temperature numerical method by Wilk et al[45], nearly all empiric and numerical methods of death-time estimation make use of single-point thermometry from a small anatomical location. Single-point core thermometry is inconsistent with approximation of antemortem body temperature distribution hypothesised by the author to affect the rate of postmortem core cooling. This thesis demonstrates that the following sources of uncertainty are natural manifestations of single-point core thermometry and can be reduced by eliminating single-point core thermometry:

1) approximating the antemortem body temperature as 37°C rectal temperature,

2) the PMTP phenomenon,

3) the thermometry-depth problem, and

4) the ground-surface material properties' problem causing shifting of the body's central isotherm.

To eliminate uncertainties of single-point core thermometry requires exploitation of the vast potential of numerical methods. Despite the potential to be independent of single-point thermometry, numerical methods of today continue to estimate the PMI by using a single-point temperature extracted at the deep rectum of their 3D computational phantom. This makes them susceptible to all the uncertainties of single-point thermometry that affect empiric methods.

This thesis proposes a multipoint axial thermometry (MAT) numerical protocol that eliminates single-point thermometry uncertainties.

3.2.10 Validation of numerical methods using empiric methods

Despite having the potential to be independent of empiric methods, numerical methods discussed in previous sections[41,42,43,44,45] were validated using the Hensβe rectal temperature nomogram method, which made them susceptible to uncertainties of single-point core thermometry this thesis now demonstrates to affect empiric methods. This thesis proposes that numerical methods are validated independent of empiric methods using MAT and case work. Validation of the numerical protocol proposed in this thesis using the Hensβe rectal temperature nomogram method was not possible because the latter provided different PMI estimates depending on temperature-depth applied, which it currently does not standardize.

Bibliography and References Cited

1. Bate-Smith EC, Bendall JR (1949). Factors determining the time course of rigor mortis. Journal of Physiology, 47-65.

2. Saukko P, Knight B. Knight's Forensic Pathology 4th ed. New York. CRC press, Taylor and Francis Group, 2016.

3. Coe JI (1993). Postmortem chemistry update. Emphasis on forensic application. The American Journal of Forensic Medicine and Pathology, 14(2), 91-117.

4. Jaffe FA (1989). Stomach contents and the time of death. The American Journal of Forensic Medicine and Pathology, 10(1), 37-41.

5. Madea B, Henβge C (1990). Electrical excitability of skeletal muscle postmortem in casework. Forensic Science International, 47(3) 207-27.

6. Pittner S, Ehrenfellner B, Zissler A, Racher V, Trutschnig W, Bathke AC, Sänger AM, Stoiber W, Steinbacher P, Monicelli FC (2017). First application of protein-based approach for the time since death estimation. International Journal of Legal Medicine, 131(2); 479-483.

7. Davey J (1839). Observations on the temperature of the human body after death. Researches, Physiological and Anatomical. London, 323-333.

8. Rainy H (1868 – 1869). On the cooling of dead bodies as indicating of time that has elapsed since death. Glasgow Medical Journal, 323-330.

9. Schwarz F, Heidenwolf H (1953). Postmortem cooling and its relation to the time of death. International Criminal Police Review, 339-344.

---

10. Sellier K (1958). Determination of the time since death by extrapolation of the temperature decrease curve. Journal of Forensic Science, 46(2): 317-322.

11. de Saram GSW, Webster G, Kathirgamatamby N (1955). Postmortem temperature and the time of death, J. Crim. Law Criminol. 562-577.

12. Marshall TK, Hoare FE (1962). Estimating the time of death. The rectal cooling after death and its mathematical expression. Journal of Forensic Science, 56-81.

13. Henβge C (1982). Temperatur-Todeszeit-Nomogramm für Bezugsstandardbedingungen der Leichenlagerung (Temperature-death-time nomogram for reference to standard conditions of cadaver storage. German) Krim. Forensische Wiss., 109-115.

14. Newton I (1701). Scale graduum caliros. Calorum descriptiones & signa (Scale of the degrees of heat). Philosophical Transactions of the Royal Society. London 22(270), 824 – 829.

15. Lyle HP, Cleveland FP (1956). Determination of the time of death by heat loss. Journal of Forensic Science, 11-24.

16. Brinkmann B, Menzel G, Riemann U (1978) Postmortale Organtemperaturen unter verschiedenen Umweltbedingungen. (Postmortem organ temperatures under different environmental conditions. German, summary in English). International Journal of Legal Medicine, 207-216.

17. Simonsen J, Voigt J, Jeppeson N (1977). Determination of the time of death by continuous post-mortem temperature measurement, Med. Sci. Law 112-122.

18. Al-Alousi LM, Anderson RA (1986). Microwave thermography in forensic medicine. Police Surgeons, 30-42.

---

19. Al-Alousi LM, Anderson RA, Land DV (1994). A non-invasive method of temperature measurements using a microwave probe. Forensic Science International, 35-46.

20. Kanawaku Y, Kanetake J, Komiya A, Maruyama S, Funayama M (2007) Computer simulation for postmortem cooling processes in the outer ear. Legal Medicine, 55-62.

21. Burman JW (1880). On the rate of cooling of the human body after death. Edinburg Medical Journal, 993-1003.

22. Womack F (1887). The rate of cooling of the body after death. St Bartholomew's Hospital Reports, Volume 23, 193-200.

23. Rhodes WF, Gordon I, Turner R (1942). Medical Jurisprudence: a South African handbook. Stewart, Cape Town.

24. Simpson K (1946). Gaps in the scientific evidence for the prosecution. Science Progress, 718-720.

25. Shapiro H (1954). Medico-legal mythology: the time of death. Journal of Forensic Medicine, 1-159.

26. Fiddes FS, Patten TD (1958). A percentage method for representing the fall in body temperature after death: its use in estimating the time of death, J. Forensic Med. 2-15.

27. Lundquist F (1956). Physical and chemical methods for the estimation of the time of death. Acta Med. Leg. Soc. (Liegre) 9, 205-13.

28. Joseph A, Schickele A (1970). A general method of assessing factors controlling postmortem cooling. Journal of Forensic Sciences, 364 – 391.

---

29. Brown A, Marshall T (1974). Body temperature as a means of estimating time of death. Forensic Science International, 125-133.

30. Nokes LDM, Hicks B, Knight B (1985). The post-mortem temperature plateau—fact or fiction? Med. Sci. Law 263-264.

31. Nelson EL (2000). Estimation of short-term postmortem interval utilizing core body temperature: a new algorithm. Forensic Science International, 109: 31- 38.

32. Smart LJ, Kaliszan M (2012). The post-mortem temperature plateau and its role in the estimation of time of death. Legal Medicine, 55-62.

33. Mfolozi S (2013). Cooling rates of dummies under various degrees of air humidity, wind speed and air temperature. Masters dissertation. University of Cape Town.

34. Henβge C (1979). Die Prazision von Todeszeitchatzungen durch die mathematische Beschriebung der rektalen Leichenbkuhlung (Precision of estimating the time of death by mathematical expression of rectal body cooling. German, summary in English). Zeit. Rechtsmed., 83:45-67.

35. Henβge C (1992). Rectal temperature time of death nomogram: Dependence of corrective factors on body weight under stronger thermic insulation conditions. Forensic Science International, 54(1):51-66.

36 Henβge C, Madea B (2004). Estimation of the time since death in the early post-mortem period. Forensic Science International, 144:167-175.

37. Bisegna P, Henβge C, Althaus L, Giusti G (2008). Estimation of the time since death: Sudden increase of ambient temperature. Forensic Science International, 176:196-199.

38. Albrecht A, Gerling I, Henβge C, Hochmeister M, Kleiber M, Madea B, Oehmichen M, St. Pollak, Püschel K, Seifert D, Teige K (1990). Zur Anwendung des Rektaltemperatur-Todsedzeit-Nomogramms am leichenfundort (Use of rectal temperature-time of death nomograms at the scene of death. German, Summary in English). Z. Rechtsmed. 103(4): 257-278.

39. Althaus L, Henssge C (1999). Rectal temperature time of death nomogram: sudden change of ambient temperature. Forensic Science International, 99:171-178.

40. Baccino E, De Saint Martin L, Schuliar Y, Guilloteau P, Le Rhun M, Morin JF, Leglise D, Amice J (1996). Outer ear and time of death. Forensic Science International, 133-146.

41. Mall G, Eisenmenger W (2005). Estimation of time since death by heat-flow Finite-element model part I: method, model, calibration and validation. Legal Medicine, 1-14.

42. Mall G, Eisenmenger W (2005). Estimation of time since death by heat-flow Finite-element model part II: application to non-standard cooling conditions and preliminary results in practical casework. Legal Medicine, 69-80.

43. Schenkl S, Muggenthaler H, Hubig M, Erdmann B, Weiser M, Zachow S, Heinrich A, Güttler FV, Teichgräber U, Mall G (2017). Automatic CT-based finite element model generation for temperature-based death time estimation: feasibility study and sensitivity analysis. International Journal of Legal Medicine, 699-712.

44. Weiser M, Erdmann B, Schenkl S, Muggenthaler H, Hubig M, Mall G, Zachow S (2017). Uncertainty in temperature-based determination of time of death. Heat and Mass Transfer, 2815-2826.

---

45. Wilk LS, Hoveling RJM, Edelman GJ, Hardy HJJ, van Schouwen S, van Venrooij H, Aalders MCG (2020). Reconstructing the time since death using non-invasive thermometry and numerical analysis. Science Advances, 6(22): eaba4243, 1-7.

46. Marshall TK (1962). The use of body temperature in estimating time of death. Journal of Forensic Science, 211-221.

47. Taylor A, Wilks D (1863). On the cooling of the human body after death. Guy’s Hospital Report, 180-213.

48. Henβge C, Hahn S, Madea B (1986). Praktische Erfahrungen mit einem Abkühlungdummy. (Practical experience with a body-cooling dummy. German, summary in English). Beitr. Gerichtl. Med., 44:123-126.

49. Henβge C, Madea B, Schaar U, Pitzken C (1987). Die Abkühlung eines Dummy unter verschiedenen Bedingungen im Vergleich zur Leichenabkühlung (The cooling of a dummy under various conditions in comparison with body cooling. German, summary in English). Beitr Gerichtl Med., 45:145-149.

50. Hiraiwa K, Ohno Y, Kuroda F, Sebetan IM, Oshida S (1980). Estimation of the postmortem interval from rectal temperature by use of computer. Medicine Science and Law, 115-125.

51. Hiraiwa K, Kudo T, Kuroda F, Ohno Y, Sebetan IM, Oshida S (1981). Estimation of the post-mortem interval from rectal temperature by use of computer – Relationship between the rectal and skin cooling curves. Medicine Science and Law, 21(1) 4 – 9.

---

52. Nokes LDM, Hicks B, Knight B (1986). The use of trachea temperature as a means of determining the postmortem interval. Med. Sci. Law 199-202.

CHAPTER 4

Bibliographic review of bioheat modelling

Chapter 4

Bibliographic review of bioheat modelling

The subject of antemortem axial temperature distribution was described in chapter 2 as the author's hypothesised predictor of absence/presence of the PMTP. One of the objectives of this thesis was to apply bioheat modelling to predict antemortem temperature distribution. The aim of this chapter was to provide the context, perspective, and rationale for the choice of the bioheat model that is applied later in thesis. This thesis contributed towards a qualification in forensic pathology and not in mechanical engineering. Therefore, by reviewing bioheat modelling, the intention was not to purport the author as a heat-transfer expert.

Bioheat modelling has applications in heating, ventilation, and air-conditioning engineering (HVAC) to predict human thermal comfort for the automotive, clothing and aerospace industries. Bioheat modelling, much like death-time estimation, is a science whose history spans several centuries, with some authors dating it back to ancient Greece[1]. And like death-time estimation methods, bioheat modelling literature today can roughly be divided into classic and modern methods.

4.1 Classic Bioheat Models

Classic bioheat models are also often referred to as integer-order models without heat flux damping. They include the Penne’s bioheat model, the Wulff and Chen-Holmes continuum models, and the Weinbaum-Jiji-Lemons models.

4.1.1 The Surface Heat Flux Model

Prior to 1948, heat transfer from the body to the surroundings was quantified by the product of a thermal conductance and a measured temperature gradient between tissue and the surroundings[2]. This surface heat flux model could be mathematically expressed as:

$$Q_s = \omega_b \rho_b c_b L_t (T_b - T_s) + \frac{k_t}{L_t}(T_b - T_s) = K_e (T_b - T_s) \qquad (4.1)$$

where Q_s was the surface heat flux through tissue of a given unit area, ω_b was the volumetric blood flow to the tissue per unit volume of it $[(m^3/s_{blood})/m^3_{tissue}]$, $\rho_b$was blood density, c_b was thermal heat capacitance of blood, L_t was tissue thickness, k_t was thermal conductivity of said tissue, $T_b$was body core temperature, T_s was skin temperature. The first term of the equation represented the thermal energy transported by blood flow through the tissue layers of depth L_t while the second term was the Fourier law. K_e was the effective thermal conductivity that could be determined by experimental measurements of skin heat flux, skin temperature and body core temperature at a depth of L_t. The second term represented heat transport by conduction. Works by Gagge et al[3], Hardy et al[4,5], Bazett et al[6,7,8], Mendelson[9] and Burton[10] applied this method together with measurements of temperature gradients between the skin and the environment under varying environmental and metabolic conditions.

4.1.2 The Pennes BioHeat Model

In 1948 Pennes[11] was inspired by lack of rigorous analysis of the local thermal gradients inside human tissue and the effect of blood perfusion on the local heat transfer rate in deep tissue. He had realised that analytical differential heat transfer theory had not previously been applied to human tissue, and subsequently embarked on an experimental and rigorous theoretical study to examine the governing heat transfer principles in perfused tissue. He devised the Pennes bioheat equation (PBE) that calculated the transient temperature distribution of the human forearm in life and included radial thermal conduction, metabolic heat generation, thermal convection by circulating blood, and heat loss from skin surface by thermal convection, thermal radiation, and thermal conduction. The PBE can expressed in the form:

$$\rho_t C_t \frac{\partial T_{ti}}{\partial t} = \nabla \cdot (k_t \nabla T_{ti}) + \rho_b C_b \omega_b (T_b - T_{ti}) + Q_m \qquad (4.2)$$

where ρ_t was density of the tissue, C_t was the specific heat capacity of the tissue, t was time, k_{ti} was thermal conductivity of the tissue, ρ_{bl} was density of blood, C_{bl} was the specific heat capacity of blood, ω_b was the blood perfusion rate of the tissue, T_b was the convective temperature of blood, T_{ti} was temperature of the tissue and Q_m was the metabolic-heat generation rate of the organ. In eqn. (4.2) each tissue's metabolism constituted a continuous heat source that was assumed to be spatially homogeneous. Heat generated by each tissue was spread to adjacent tissues by thermal diffusion as well as blood perfusion. The mathematical representation of the latter acted as a homogeneous, tissue-specific heat-sink term. The combined effects of endogenous metabolic heat, heat transfer by blood flow, heat transfer between tissues by thermal conduction, and heat transfer between the skin and ambient air by thermal convection and thermal radiation determined the overall temperature filed of the tissue. Following its publication, the PBE was criticised for its simplistic assumption of uniform metabolic heat, perfusion rate and thermal conductivity. Some of these criticisms are discussed in the next sections.

4.1.3 The Wulff Continuum Model

Wulff[12] pointed out that the PBE in its original form contained both local and global control systems before assumptions were made about thermal equilibration of blood in the circulation, which was physically inconsistent. His second criticism was that the original PBE contained three unknown temperatures, i.e. tissue temperature, the entrance arterial temperature and the exit venous temperature. Wulff suggested that two more equations were therefore required to fully define the system both mathematically and physiologically. His third criticism of the PBE was the representation of heat transfer between the solid tissue and moving fluid blood stream. Wulff asserted that since blood moved through tissue, it could convect heat in any direction and not necessarily only in the direction of the local tissue temperature gradient, pointing out that the isotropic term in the PBE did not account for convective heat transfer. A fourth criticism of the PBE pointed out by Wulff was that presence of arterial and venous circulation within the solid tissue rendered impossible the existence of the continuous tissue temperature gradients by the conduction term in the PBE. Wulff presented his own Continuum Model as an alternative to the PBE, which could be expressed as:

$$\rho_b c_b \frac{\partial T_{ti}}{\partial t} = k_t \nabla^2 T_t - \rho_b \mathrm{v}_b c_b \nabla T_t + Q_m \qquad (4.3)$$

where $\rho_b c_b$ was the heat capacity product (equal to the negative gradient of the net energy flux into the control volume), ρ_b was blood density, ν_b was blood volume and $\rho_b v_b$ was the local blood mass flux. To derive the equation, Wulff made several assumptions of his own, namely that the gradient in blood temperature in eqn. (4.3) was equal to the gradient of the surrounding tissue temperature. Determination of the local blood mass flux value hindered practical application of the Wolff model.

4.1.4 The Klinger Continuum Model

The analytical model of heat diffusion presented by Klinger in 1974[13,14] was conceptually similar to the Wolff model. It described thermal clearance experiments in which tissue perfusion rate was related to the rate at which deep-tissue temperature changed during point-source heating. Klinger argued that the PBE neglected effects of non-unidirectional blood flow when used to interpret the clearance experiments, thereby introducing significant errors in the computed results. To correct for lack of directionality in the PBE, Klinger proposed that the convection field inside the tissue should be modelled on *in vivo* vascular anatomy by introducing the concept of convective multipoles that accounted for magnitude and direction of blood flow. The Klinger model assumed that tissue thermophysical properties were constant, and that blood flow was incompressible. The Klinger model introduced the concept of enhancement of tissue thermal conductivity due to the presence of blood flowing in the tissue via a conduction tensor. The model used the Green's function solution to quantify the significance of vessel number density, blood perfusion rate and vessel architecture on the enhancement of tissue conduction. Significant observations made by Klinger were:

a) that the temperature field was mostly influenced by the geometric arrangement of blood vessels,
b) that a co-current flow structure resulted in a mean velocity that was analogous to the D'Archy velocity that enhanced conductivity in the flow direction, while the enhancement was independent of vessel density, and

c) that a counter-current system of blood vessels influenced tissue conductivity anisotropically, the magnitude of which was inversely proportional to blood vessel density and proportional to the total volumetric blood flow rate in the tissue.

These results emphasised the significance of geometry and flow direction of the microcirculation, which was not considered by the PBE.

4.1.5 The Chen-Holmes Continuum Model

The model by Chen and Holmes[15] employed a continuum description of the tissue-blood control volume, like the models described by Wulff[12] and Klinger[13]. This was justified by the presence of many smaller blood vessels in a tissue volume, whose characteristic dimension was significantly larger than those of the individual blood vessels. That effect on the heat transfer on the tissue was based on statistical grouping of small blood vessels and was incorporated in the physical parameters that governed heat transfer. The Chen-Holmes model was thus a microvascular model in which effects of blood vessels of 1mm diameter or more were excluded from the energy balance equation, as they would have otherwise violated the continuum assumption that the length scale of the tissue temperature variations was much larger than the dimension of the individual blood vessels. The Chen-Holmes bioheat equation was expressed as:

$$\rho c \frac{\partial T_{\mathrm{t}}}{\partial t} = \nabla \cdot k_{\mathrm{t}} \nabla T_{\mathrm{t}} + \nabla \cdot k_p \nabla T_{\mathrm{t}} + \omega_{\mathrm{j}}^{*} \rho_{\mathrm{b}} c_{\mathrm{b}} (T_b^{*} - T_{\mathrm{t}}) - \rho_{\mathrm{b}} c_{\mathrm{b}} \mathrm{v}_{\mathrm{p}} \cdot \nabla T_{\mathrm{t}} + Q_m \qquad (4.4)$$

where ω_j^* was the tissue's total perfusion bleed-off from the micro-vessels past the j^*th generation of branching, T_b^* was the blood temperature at the j^*th generation of branching, k_p was the perfusion conductivity representing the effect of blood flow, T_{t} was the volume-weighted continuum temperature of the tissue and $\rho_{\mathrm{b}} \mathrm{v}_{\mathrm{p}}$ was the mass flux of blood flowing through the tissue. The second term of eqn. (4.4) on the right-hand side modelled the enhancement of thermal conduction in the tissue due to blood flow within blood vessels whose thermal equilibration lengths were of the same order of magnitude as the lengths of the blood vessels themselves. At first glance, the third term of eqn. (4.4) on the right-hand side was similar to the perfusion heat-source term of the PBE in eqn. (4.2). However, the ω_j^* in eqn. (4.4) differed from ω in eqn. (4.2) in that, in eqn. (4.2), ω included bleed-off from all generations of vasculature. Secondly, Chen and Holmes demonstrated that T_b^* was not equal to the initial arterial temperature of blood as it was ejected from the heart into the aorta. It was stated that the difference between the two temperatures could be 10-50%. To model bioheat transfer of larger blood vessels beyond the j^*th generation, Chen and Holmes proposed individual examination of such arteries and veins as macroscopic entities. The fourth term of eqn. (4.4) on the right-hand side was the usual convective transport term that accounted for the effects on tissue heat transfer of direction of blood flow within the tissue.

The concept by Chen and Holmes of introducing thermal equilibration length to account for bulk flow convection heat transfer instead of assuming thermal equilibration in all vessels of the circulation, as Wulff[12] had done, made the Chen-Holmes Continuum Model able to define an effective thermal conductivity in tissue by the convective transport associated with blood flow. This was similar to the approach by Klinger[13,14]. Also, the Chen and Holmes observed that thermal equilibration between blood and tissue occurred at the terminal branches of the arteries, thus demonstrating that the main assumption of the PBE, i.e. absence of precapillary heat transfer, was not possible.

Some observers[2] commented that the Chen-Holmes bioheat equation could be reduced to the Pennes bioheat equation in the absence of anatomical data to determine v_p, k_p and ω_j^*, especially considering that k_p was necessarily a complicated function of blood vessel geometry and architecture. Another criticism of the Chen-Holmes model was that it did not examine the effect of counter-current heat transfer between closely-spaced paired arteries and veins, something the Klinger model had done.

4.1.6 The Weinbaum-Jiji-Lemons Models

Weinbaum, Jiji et al[16,17,18,19,20,21,22,23,24,25] developed several bioheat model iterations over a number of years as an alternative to the PBE, citing its lack of directionality in the isotropic perfusion term and the neglect of the influencer of larger blood vessels embedded in the perfused tissue on tissue-blood heat transfer. They criticized the PBE for not accounting for the branching, tapered diameters of the paired counter-current artery-veins as they gradually became arterioles, venules, and capillary beds.

In 1979 Weinbaum and Jiji[20] presented a two-phase formulation consisting of a blood phase and a tissue phase. The schematic view of the circulation they used to analyse bioheat transfer consisted of an artery-vein pair running 1-3 cm beneath the skin surface and parallel to the skin surface. Terminal arteries periodically branched out of the supply artery normal to skin in the radial direction, undergoing up to 10 generations of branching and tapering that caused continuous reduction of their diameters in the process. Capillary beds were mostly located in a superficial shunt layer 1-3mm beneath the surface of the skin. From there, blood flowed into venules that drained into a superficial vein running just beneath the skin surface and parallel to it. This arrangement constituted a counter-current blood flow scheme. The blood phase was thus a mathematical model that accounted for variations in vessel number density of approximately six orders of magnitude, blood velocity and vessel diameter variations of two orders of magnitude, and vessel Reynaud numbers that decreased by four orders of magnitude at the inflow to the end of the vascular tree at the skin surface. The energy balance equations for arterial and venous temperature, as a function of the radial distance from the vessel axis were expressed, respectively, as:

$$\rho c_{\mathrm{b}} u_{\mathrm{a}}(x,r)\frac{\partial T_{\mathrm{a}}(x,r)}{\partial r}=\frac{k_{\mathrm{b}}}{r}\frac{\partial}{\partial r}\left(r\frac{\partial T_{\mathrm{a}}(x,r)}{\partial r}\right)-\mu\left(\frac{\partial u_{\mathrm{a}}}{\partial r}\right)^{2} \tag{4.5}$$

$$\rho c_{\mathrm{b}} u_{\mathrm{v}}(x,r)\frac{\partial T_{\mathrm{v}}(x,r)}{\partial r}=\frac{k_{\mathrm{b}}}{r}\frac{\partial}{\partial r}\left(r\frac{\partial T_{\mathrm{v}}(x,r)}{\partial r}\right)-\mu\left(\frac{\partial u_{\mathrm{v}}}{\partial r}\right)^{2} \tag{4.6}$$

where u_{a} was arterial blood flow velocity, u_{v} was venous blood flow velocity, T_{a} was bulk arterial blood temperature, T_{v} was bulk venous blood temperature, x was the axial coordinate, r was the radial coordinate, μ was blood viscosity, k_{b} was blood thermal conductivity, c_{b} was blood specific heat capacity, and ρ was blood density. The second term on the right-hand side thus represented heat transfer associated with viscous dissipation in blood vessels. The algebraic sign of u_{a} was positive while that of u_{v} was negative to indicate the counter-current nature of heat transfer in the artery-vein pair.

The tissue phase involved heat transfer in the tissue medium surrounding the artery-vein pair. Weinbaum and Jiji proposed that collateral blood flow in the plane normal to the artery-vein pair was unidirectional from artery to vein in the radial direction. They modelled this effect of blood flow as one-dimensional heat transfer through a porous medium. The counter-current nature of blood flow through the porous medium caused the artery-vein pair to have two regions-of-influence, one around each vessel, whose temperatures differed. The respective energy balance equations of these regions thus were expressed as:

$$c_{\mathrm{b}}\frac{ga_{\mathrm{a}}}{r}\frac{\partial\theta_{\mathrm{a}}}{\partial r}=k_{\mathrm{t}}\left(\frac{\partial^2\theta_{\mathrm{a}}}{\partial x^2}+\frac{1}{r}\frac{\partial}{\partial r}\left(r\frac{\partial\theta_{\mathrm{a}}}{\partial r}\right)\right)+Q_m \tag{4.7}$$

$$-c_{\mathrm{b}}\frac{ga_{\mathrm{v}}}{r}\frac{\partial\theta_{\mathrm{v}}}{\partial r}=k_{\mathrm{t}}\left(\frac{\partial^2\theta_{\mathrm{v}}}{\partial x^2}+\frac{1}{r}\frac{\partial}{\partial r}\left(r\frac{\partial\theta_{\mathrm{v}}}{\partial r}\right)\right)+Q_m \tag{4.8}$$

where c_{b} was blood specific heat capacity, g was the volumetric bleed-off rate per unit vessel surface area leaving arterial flow or entering venous flow, a was vessel radius, θ_{a} was arterial tissue temperature, θ_{v} was venous tissue temperature, k_{t} was tissue thermal conductivity, x was the axial coordinate, r was the radial coordinate and Q_m was the tissue metabolic rate of heat production per unit volume. The perfusion velocity was thus inversely proportional to the r-position in order to conserve mass in the collateral circulation. The minus sign on the left-hand side of eqn. (4.8) accounted for blood flow in terminal veins in the negative x-direction.

In addition to the two phases described above, the two-phase model by Weinbaum and Jiji also involved heat transfer in the cutaneous circulation in which the tissue temperature of the thin skin layer was determined by considering the vascular architecture in that region. Weinbaum and Jiji had experimentally observed that blood in the skin passed directly from arterioles to venules as part of the cutaneous thermoregulatory system. They modelled the effect of blood flow in the skin tissue layer as one-dimensional heat transfer through a porous medium, mathematically expressed as:

$$w_{\mathrm{b}}(x)c_{\mathrm{b}}\frac{d\theta_{\mathrm{s}}}{dx} = k_{\mathrm{t}}\frac{d^2\theta_{\mathrm{s}}}{dx^2} \qquad (4.9)$$

where w_b was blood perfusion flux in the tissue layer beneath the skin, defined in the region $L \le x \le (L + \varepsilon)$ where x was the axial coordinate and $x = (L + \varepsilon)$ was at the skin surface and θ_{s} was skin temperature.

In a follow-up study in 1984, Weinbaum et al[17,21] identified three different vascular structures corresponding to three different tissue-depth layers that were 1) a >4mm thick deep-tissue layer, 2) a 2-4mm thick intermediate layer and 3) a 0-2mm thick cutaneous layer. In the deep-tissue layer there were paired counter-current arteries and veins that were oriented oblique to skin surface. Their number density, radii, inclination angle, centre-to-centre spacing, and radius-of-influence all varied along the length of the counter-current network. Vessels branched as they approached the intermediate layer, remaining counter-current in the first five to six generations of branching. Heat exchange occurred between the artery-vein pair into the surrounding tissues of the deep layer both by conduction and capillary bleed-off. The governing equations of the deep-tissue layer, presented by Jiji et al[17], were derived by considering blood vessel geometry and capillary bleed-off on a continuous basis. The two nondimensionalized governing equations based on the total length of the counter-current network in the deep layer and on the flow Peclet number in the blood vessel at each location were:

$$\tilde{a}\mathrm{Pe}^{*}\frac{d}{d\tilde{s}}\left(\tilde{T}_{\mathrm{a}}-\tilde{T}_{\mathrm{v}}\right)=4v\left(\tilde{T}_{\mathrm{a}}-\tilde{T}_{\mathrm{v}}\right)+\frac{d}{d\tilde{s}}\left(\tilde{a}^{2}\tilde{R}^{2}\frac{d}{d\tilde{s}}\left(\tilde{T}_{\mathrm{a}}+\tilde{T}_{\mathrm{v}}\right)\right) \tag{4.10}$$

$$\tilde{a}\mathrm{Pe}^{*}\frac{d}{d\tilde{s}}\left(\tilde{T}_{\mathrm{a}}+\tilde{T}_{\mathrm{v}}\right)=\frac{-8\left(\tilde{T}_{\mathrm{a}}-\tilde{T}_{\mathrm{v}}\right)}{\cosh^{-1}\left(\tilde{l}_{\mathrm{s}}^{2}/2-1\right)} \tag{4.11}$$

where the dimensionless distances $\tilde{a}$, $\tilde{s}$, $\tilde{l}_{\mathrm{s}}$ and $\tilde{R}$ were the parameters a, s, l_{s} and R normalised by the total length of the counter-current network in the deep layer, respectively. l_{s} was the distance between centres of artery-vein pair, s was the distance coordinate along the artery-vein pair axis, a was vessel radius, R was the radius of cylinder-of-influence in the tissue around a vessel, T_{a} was the artery bulk temperature, T_{v} was the vein bulk temperature, and Pe^{*} was the modified Peclet number. The dimensionless perfusion parameter v was equal to $\rho_{\mathrm{b}}c_{\mathrm{b}}\,ag/k_{\mathrm{t}}$, where ρ_{b} was blood density, c_{b} was blood specific heat capacity, g was the volumetric bleed-off rate per unit vessel surface area leaving arterial flow or entering venous flow and k_{t} was deep-tissue thermal conductivity.

In the intermediate layer, the paired arterial and venous blood temperatures differed slightly (<0.2°C) due to a relatively larger spacing in the order of 0.5-1mm. The blood vessels themselves were small enough to allow nearly complete thermal equilibration between blood and the surrounding tissue near the blood vessel wall. Heat transfer occurred in the plane containing the transverse bleed-off vessels in the intermediate layer. The porous medium model presented by Weinbaum and Jiji[17,21] in 1979 was applied to describe heat transfer in this region. Eqns. (4.7) and (4.8) were thus nondimensionalised using $\tilde{x} = x/x_0$, where x_0 was the thickness of the intermediate tissue layer, $\tilde{r} = 2r/l_0$ where l_0 was the spacing between neighbouring transverse vessels, and θ_a and θ_v were the dimensionless temperatures of the tissues surrounding an artery and a vein, respectively, in an artery-vein pair:

$$\beta^2 \frac{\partial^2 \tilde{\theta}_\mathrm{a}}{\partial \tilde{x}^2} + \frac{\partial^2 \tilde{\theta}_\mathrm{a}}{\partial \tilde{r}^2} + (1 - v)\frac{1}{r}\frac{\partial \tilde{\theta}_\mathrm{a}}{\partial r} = -\lambda \qquad (4.12)$$

$$\beta^2 \frac{\partial^2 \tilde{\theta}_\mathrm{v}}{\partial \tilde{x}^2} + \frac{\partial^2 \tilde{\theta}_\mathrm{v}}{\partial \tilde{r}^2} + (1 + v)\frac{1}{r}\frac{\partial \tilde{\theta}_\mathrm{v}}{\partial r} = -\lambda \qquad (4.13)$$

where β was the ratio $l_0/2x_0$ and λ was the dimensionless metabolic heat source $Q_m l_0^2/(4k_\mathrm{t}(T_0 - T_\mathrm{s}))$. Eqns. (4.12) and (4.13) were then subject to several boundary conditions. An additional boundary region was described between the deep-tissue layer and the intermediate layer as a plane where small temperature gradients normal to the counter-current vessel axes coexisted with large temperature gradients normal to the skin surface.

The cutaneous layer was dominated by thermal conduction normal to the skin surface. Weinbaum et al[17,21] reported that arterial blood supply to the skin was physically separate from the arterial supply to muscle tissue, contrary to their earlier model[20] that had presumed that arterial blood was supplied to the skin via the last generation of branching in the muscle layer and that venous blood was drained either through the venous network in the muscle layer or through the venous network in the muscle. They observed that only a small fraction of arterial blood was directed directly towards the cutaneous layer cells for nutrition and oxygenation. Most of the blood in thermally significant blood vessels flowed directly from artery to vein through 20-40μm anastomoses in the cutaneous plexus. The effect of blood flow in this plexus was thus modelled as a distributed volumetric heat source. Weinbaum et al noted that arterial supply vessels were large with long thermal equilibration lengths, which meant that the temperature of arriving arterial blood supply would be higher than that of the surrounding tissue. They proposed that such an effect could be mathematically modelled as a uniformly distributed heat source, similar to the heat source term of the PBE. The dimensionless energy balance equation in the inner region of the cutaneous layer was expressed as:

$$\frac{d^2\tilde{\phi}_1}{d\tilde{y}^2} + W_{\mathrm{b}}^2\left(\tilde{\phi}_{\mathrm{b}} - \tilde{\phi}_1\right) = 0, \qquad 0 < \tilde{y} < \tilde{y}_1 \tag{4.14}$$

where W_{b}^2 was the dimensionless cutaneous perfusion parameter $2\pi\rho_{\mathrm{b}}c_{\mathrm{b}}a_{\mathrm{c}}n_{\mathrm{c}}\mathrm{g}_{\mathrm{c}}y_0^2/\widetilde{K}_1$ in which a_{c}, n_{c} and g_{c} were the radius, number density and perfusion bleed-off rate associated with small bleed-off vessels in this region;ρ_{b} was blood density, c_{b} was blood specific heat capacity, y_0 was the thickness cutaneous layer and $\widetilde{K}_1$ was the average thermal conductivity of cutaneous layer. In eqn. (4.14), $\tilde{\phi}_1$ was the dimensionless temperature distribution in the inner region of the cutaneous layer, $\tilde{\phi}_{\mathrm{b}}$ was the dimensionless average arterio-venous blood temperature in the cutaneous plexus, $\tilde{y}$ was the dimensionless cutaneous layer axial coordinate equal to y/y_0, and $\tilde{y}_1$ was the dimensionless thickness of the cutaneous plexus region.

Weinbaum et al regarded the outer region of the cutaneous layer as a simple one-dimensional conduction layer so that:

$$\frac{d^2\tilde{\phi}_2}{d\tilde{y}^2} = 0, \qquad \tilde{y}_1 < \tilde{y} < 1 \tag{4.15}$$

Eqns. (4.14) and (4.15) assumed that no metabolic heat originated from the cutaneous layer and were both subject to several boundary conditions.

In 1985 Weinbaum and Jiji[22] proposed a simplified version of the three-layer bioheat model that included imperfect counter-current heat exchange between artery-vein and blood-tissue in a single equation. The simplified version was derived from the three heat transfer equations for artery, vein, and tissue of the original three-layer model, but in addition contained tissue temperature and its spatial derivatives and an effective thermal conductivity that accounted for the imperfect heat exchange. The effective thermal conductivity was purely a function of vascular geometry and blood flow rate. Weinbaum and Jiji argued that the counter-current effect acted like a heat source or heat sink in the tissue. The simplified version included the effect of unidirectional capillary bleed-off normal to the axes of the paired counter-current vessels. The advantage of the simplified version was its relative ease of implementation in comparison to the three-layer bioheat model.

4.1.7 The Porous Medium Models

All the continuum models discussed in the previous section had some criticism of the PBE and attempt to improve its deficiencies. Each model was applicable to a certain type of living tissue, and whole-body generalisations proved difficult. As an alternative, several researchers[26,27,28,29,30,31,32] turned to the porous medium modelling approach that applied volume averaging theory in which biological tissue was divided into three compartments, namely blood vessels, cells and the interstitium. The latter was further divided into the extracellular matrix and interstitial fluid. For simplicity, however, only the vascular and extra-vascular regions were considered, in which the latter was regarded as solid matrix even though it consisted of extravascular fluid. The extra-vascular region was conveniently referred to simply as 'tissue'. The two regions were treated as a porous medium having specific porosity variations, effective heat conductivities and heat dispersion by blood flow. Porous medium bioheat models assume thermal energy transfer between blood flow and tissue to be in thermal non-equilibrium as described by Amiri and Vafai[33,34], Alazmi and Vafai[35], Lee and Vafai[36], Vafai and Sözen[37,38], and Sözen and Vafai [39,40]. The combined energy equations that represented heat transfer in the blood and solid matrix phases was expressed as:

$$[(\rho c)_{\mathrm{b}}\varepsilon + (1-\varepsilon)(\rho c)_s]\frac{\partial\langle T\rangle}{\partial t} + \varepsilon(\rho c)_b\langle\vec{V}\rangle^b \cdot \nabla\langle T\rangle$$

$$= \nabla[(\mathbf{k}_s^a + \mathbf{k}_b^a)\cdot\nabla\langle T\rangle] + q_m(1-\varepsilon) \tag{4.16}$$

where q_m was the metabolic heat generation rate in the tissue layer per unit volume, ρ_b and c_b were blood density and blood specific heat, respectively; and $\langle T\rangle^b$, $\langle T\rangle^s$, $\mathbf{k}_b^a$, $\mathbf{k}_s^a$, $\langle\vec{V}\rangle^b$, h_{bs}, and ε were the local volume-averaged arterial blood temperature, local volume-averaged solid-tissue temperature, blood effective thermal conductivity tensor, solid-tissue effective thermal conductivity tensor, blood velocity vector, interstitial convective heat transfer coefficient and porosity, respectively.

4.2 Modern BioHeat Modelling Methods

One of the criticisms levelled against bioheat models of Pennes[11], Wulff[12], Klinger[13,14], Chen-Holmes[15] and Nakayama[27,28,29] (porous medium method) was that they were based on Fourier Law, which led to parabolic equations that had an unphysically infinite speed of heat flux. In the physical world, temperature disturbances were said to be due to motion of particle-carriers such as electrons, and quanta such as photons, so that thermal disturbances propagate with a finite speed. In biological tissue, relaxation times were said to be in the order of 10-30s[41,42,43,44]. In some studies, muscle tissue revealed anisotropy under strong local heating conditions that could not be explained by Fourier Law alone[45,46,47]. These observations led to the formulation of so-called 'thermal-wave bioheat models'[48,49] that were based on thermal-wave propagation theory. Thermal-wave bioheat modelling consisted of single-phase lag (SPL) and double-phase lag (DPL) approaches, both of which led to hyperbolic equations that had finite speeds of the solution. Thermal-wave bioheat models were alternatively referred to as 'heat flux relaxation (damping)' bioheat models.

4.2.1 The Single-phase Lag (SPL) Approach

The SPL approach, also referred to as the Maxwell-Cattaneo approach[50,51] applied a heat flux relaxation time called a ‘phase-lag parameter’. After formal temporal translation and Taylor expansion, a hyperbolic heat equation was expressed as:

$$\lambda_{qp}\frac{\partial^2 T}{\partial t^2} + p\frac{\partial T}{\partial t} = k\frac{\partial^2 T}{\partial x^2} \tag{4.17}$$

whose solution was a weakly-damped wave equation. The SPL approach could be further expressed either with or without blood perfusion relaxation.

4.2.2 The Double-phase Lag Approach

The DPL approach was proposed by Tzou[52] as an extension of the Maxwell-Cattaneo approach that didn't work correctly when applied to a medium with microstructural interaction effects.

$$q + \lambda_q \frac{\partial q}{\partial t} = -k\frac{\partial T}{\partial x} - k\lambda_T \frac{\partial}{\partial t}\left(\frac{\partial T}{\partial x}\right) \tag{4.18}$$

where λ_q and λ_T were relaxation times.

4.2.3 The Ezzat Fractional Bioheat Model

Fractional bioheat models using time-fractional derivatives constitute a modern trend in modelling heat transport processes with relaxations. Fractionalization of the classical integer-order bioheat models by application of fractional Taylor series expansion was a feasible technique that resulted in simple time-fractional equations. Ezzat et al[53,54] applied fractional Taylor series expansion of the order with modified Reichmann-Liouville derivatives of Jumarrie[55] to Fourier Law to express the flux-temperature gradient. After a series of mathematical steps, the final Ezzat equation was expressed as:

$$\rho c\left(T+\frac{\tau^{\alpha}}{\alpha!}\frac{\partial^{\alpha}T}{\partial t^{\alpha}}\right)=k\nabla^{2}T+\left(Q+\frac{\tau^{\alpha}}{\alpha!}\frac{\partial^{\alpha}Q}{\partial t^{\alpha}}\right),\quad 0<\alpha<1 \qquad (4.19)$$

Eqn. (4.19) was the result of formal fractionalization of the PBE[11] by first-order fractional Taylor series expansion of the heat flux and by acceptance of the concept by Wulff[12] about the perfusion term in which the reference temperature was the arterial temperature.

4.2.4 The Damor Fractional Bioheat Model

The model by Damor et al[56] was a fractional version of the PBE by simple replacement of the time derivative with a fractional counterpart as a Caputo derivative of the order $\alpha \, \epsilon \, (0,1)$, with singular power-law kernel and the spatial derivative by a Reisz-Feller fractional derivative of the order $\beta \, \epsilon \, (0,2)$, as:

$$\rho_t C_t \frac{\partial^\alpha T_t(x,t)}{\partial t^\alpha} = k_{\alpha,\beta} \frac{\partial^\beta T_t(x,t)}{\partial x^\beta} + W_{\mathrm{b}} C_{\mathrm{b}} (T_a - T_t) + q_m,$$

$$0 < \alpha < 1, \quad 0 < x < L \tag{4.20}$$

where W_{b} and C_{b} were related to blood and T_t was tissue temperature. The approach by Damor et al of formal replacement of integer-order derivatives by fractional counterparts was criticised as being incorrect because it was simply not based on basic laws.

4.2.5 The Ferras Fractional Bioheat Model

Ferras et al[57] applied a timer-fraction Caputo derivative to the Pennes bioheat equation in the form:

$$\frac{\partial^\alpha T(x,t)}{\partial t^\alpha} = A\frac{\partial}{\partial x}\left(k(x)\frac{\partial T(x,t)}{\partial x}\right) - BT(x,t) + C, \quad 0 < t < T, \quad 0 < x < L,$$

$$0 < \alpha < 1 \tag{4.21}$$

where $A = \frac{1}{\rho_t C_t}\frac{1}{\tau^{\alpha-1}}$, $B = \frac{W_b C_b}{\rho_t C_t}\frac{1}{\tau^{\alpha-1}}$, $C = \frac{W_b C_b + q_m}{\rho_t C_t}\frac{1}{\tau^{\alpha-1}}$. A new parameter τ was added to ensure dimensional consistency, which was the same approach used by Ezzat[54] who applied multiplication by $\tau^\alpha/\alpha!$. The introduction of the τ parameter was criticised as being unphysical[58]. Also, the assertion by Ferras that 'a new relationship between heat flux and temperature gradient was established' was said to be untrue because Ferras had applied the fading-memory approach of Gurtin and Pipkon[59] incompletely. Ferras was criticised for using only the pseudo-elastic part of the heat flux and expressing it as a Reimann-Lioville derivative, which naturally produced a well-known time-fractional diffusion equation.

4.2.6 Justification for using the PBE in this thesis

As stated before, the method by integer-order bioheat models of applying Fourier Law through the energy balance equation resulted in a parabolic heat conduction equation that had an unphysically infinite speed of heat flux. This led to the development of different approaches of heat flux relaxation, i.e. fractionalization approaches and the fading-memory approach, applicable to the classical bioheat equations, e.g. by Pennes and Wulff.

In this thesis, the PBE is applied in numerical analyses to approximate antemortem body temperature distribution (chapter 6) in which the speed of heat flux is of no consequence. Subsequent studies of this thesis that investigate postmortem axial heat transfer (chapter 7) do not require bioheat modelling but apply approximated antemortem body temperature distribution in initial conditions. The anatomical segmentation of the 3D computational phantom used as a human body surrogate in this thesis was at organ level, so that bioheat models that operate at tissue level, e.g. the Weinbaum-Jiji-Lemons models, were deemed unnecessary. The diverse nature of organ geometry of the 3D computational phantom used as a human body surrogate in this thesis presented an added complication.

A range of bioheat models[60,61] alternative to the PBE have been proposed to increase realism or extend the application range. However, many require a large number of additional parameters that are rarely available or highly variable[2]. Such bioheat models were not appropriate for this study. Therefore, the PBE was the best model.

Bibliography and References Cited

1. Chato JC (1992). A view of the history of heat transfer in bioengineering. Advances in Heat Transfer, 1-18.

2. Charny CK. Mathematical models of bioheat transfer. Adv Heat Transf. (1992) 22:19–155.

3. Gagge AP, Winslow CA, Herrington LP (1938). The influence of clothing on the physiological reactions of the human body to varying environmental temperatures. Am. J. Physiol. 124, 30.

4. Hardy JD, DuBois EF (1938). Basal metabolism, radiation, convection, and vaporization at temperatures of 22 to 35°C. J. Nutr. 15, 477.

5. Hardy JD, Soderstrom GF (1938). Heat loss from the nude body and peripheral blood flow at temperatures of 22°C to 35°C. J. Nutr. 16, 493.

6. Bazett HC, McGlone B (1927). Temperature gradients in the tissues in man. Am. J. Physiol. 82,415.

7. Bazett HC, Love L, Newton M, Eisenberg L, Forster RE (1948). Temperature changes in blood flowing in arteries and veins in man. J. Appl. Physio. 1, 3.

8. Bazett HC, Mendelson ES, Love L, Libet B (1948). Precooling of blood in the arteries, effective heat capacity and evaporative cooling as factors modifying cooling of the extremities. J. Appl. Physiol 1, 169.

9. Mendelson ES (1936). Measurement of the superficial temperature gradient in man. Am. J. Physiol. 114, 642.

10. Burton AC (1934). The application of the theory of heat flow to the study of energy metabolism. J. Nutr. 7, 497.

11. Pennes HH (1948). Analysis of tissue and arterial temperatures in the resting human forearm. Journal of Applied Physiology, 93-122.

12. Wulff W (1974). The energy conservation equation of living tissues. IEEE Trans. Biomed. Eng. 21:494-5.

13. Klinger HG (1974). Heat transfer in perfused biological tissue. I. General theory. Bulletin of Mathematical Biology 36:403-15.

14. Klinger HG (1976). Heat transfer in perfused biological tissue. II. The macroscopic temperature distribution. Bull. Math. Biol. 38, 183.

15. Chen MM, Holmes KR (1980). Microvascular contributions in heat tissue transfer. Annals of the New York Academy of Science, 355:137-50.

16. Dagan Z, Weinbaum S, Jiji LM (1986). Parametric studies on the three-layer microcirculatory model for surface tissue energy exchange. ASME Journal of Biomechanical Engineering 108, 89.

17. Jiji LM, Weinbaum S, Lemons DE (1984). Theory and experiment for the effect of vascular microstructure on surface tissue heat transfer. Part II. Model formulation and solution. ASME J. Biomech. Eng. 106, 331.

18. Song WJ, Weinbaum S, Jiji LM (1987). A theoretical model for peripheral tissue heat transfer using the bioheat equation of Weinbaum and Jiji. ASME J. Biomech. Eng. 109, 72.

---

19. Song WJ, Weinbaum S, Jiji LM, Lemons DE (1988). A combined macro and microvascular model for whole limb heat transfer. ASME J. Biomech. Eng. 110, 259.

20. Weinbaum S, Jiji LM. A two phase theory for the influence of circulation on the heat transfer in surface tissue. In “1979 Advances in Bioengineering” (Wells MK, ed.), pp. 179-182. American Society of Mechanical Engineers, New York, 1979.

21. Weinbaum S, Jiji LM, Lemons DE (1984). Theory and experiment for the effect of vascular microstructure on surface tissue heat transfer. Part I. Anatomical foundation and model conceptualization. ASME J. Biomech. Eng. 106, 321.

22. Weinbaum S, Jiji LM (1985). A new simplified bioheat equation for the effect of blood flow on local average tissue temperature. ASME J. Biomech. Eng. 107, 131.

23. Weinbaum S, Jiji LM (1987). Discussion of papers by Wissler and Baish et al concerning the Weinbaum-Jiji bioheat equation. ASME J. Biomech. Eng. 109, 234.

24. Weinbaum S, Jiji LM (1989). The matching of thermal fields surrounding countercurrent microvessels and the closure approximation in the Weinbaum-Jiji equation. ASME J. Biomech. Eng. 111, 271.

25. Zhu M, Weinbaum S, Lemons DE (1988). On the generalization of the Weinbaum-Jiji equation to microvessels of unequal size: The relation between the near field and local average tissue temperatures. ASME J. Biomech. Eng. 110, 74

26. Khanafer K, Varfai K. Synthesis of mathematical models representing bioheat transport. In: Minkowycz W, Sparrow E, Abraham J, editors. Advances in Numerical Heat Transfer, Vol. 3. CRC Press (2009),1-28.

27. Nakayama A, Sano Y, Yoshikawa K (2010). A rigorous derivation of the bioheat

---

equation for local tissue heat transfer based on a volume averaging theory. Heat Mass Transf. 46:739–46.

28. Nakayama A, Kuwahara F (2008). A general bioheat transfer model based on the theory of porous media. Int J Heat Mass Trans. 51:3190–9.

29. Nakayama A, Kuwahara F, Liu W. A general set of bioheat transfer equations based on the volume averaging theory. In Vafai K, editor. Porous Media, Applications in Biological Systems and Biotechnology. Boca Raton, FL: CRC Press (2010). p. 1-44.

30. Bejan A, Dincer I, Lorente S, Miguel A, Reis A. Porous and Complex Flow Structures in Modern Technologies. New York, NY: Springer-Verlag (1984).

31. Khaled ARA, Vafai K (2003). The role of porous medium in modeling flow and heat transfer in biological tissues. Int J Heat Mass Trans, 46:4989–5003.

32. Khanafer K, Vafai K (2006). The role of porous media in biomedical engineering as related to magnetic resonance imaging in drug delivery. Heat Mass Trans, 42:939–53.

33. Amiri A, Vafai K (1994). Analysis of dispersion effects and nonthermal equilibrium, non-Darcian, variable porosity incompressible-flow through porous media, Int. J. Heat Mass Trans, 37:939–954.

34. Amiri A, Vafai K (1998). Transient analysis of incompressible flow through a packed bed. Int. J. Heat Mass Trans, 41:4259–4279.

35. Alazmi B, Vafai K (2002). Constant wall heat flux boundary conditions in porous media under local thermal non-equilibrium conditions. Int. J. Heat Mass Trans, 45; 3071–87.

---

36. Lee DY, Vafai K (1999). Analytical characterization and conceptual assessment of solid and fluid temperature differentials in porous media, Int. J. Mass Trans, 42; 423-35.

37. Vafai K, Sözen M (1990). An investigation of a latent heat storage packed bed and condensing flow through it. ASME J. Heat Trans, 112;1014-22.

38. Vafai K, Sözen M (1990). A Comparative analysis of multiphase transport models in porous media. Ann. Rev. Heat Trans, 3;145-62.

39. Sözen M, Vafai K (1991). Analysis of oscillating compressible flow through a packed bed. Int. J. Heat Fluid Flow, 12;130-6.

40. Sözen M, Vafai K (1990). Analysis of the non-thermal equilibrium condensing flow of a gas through a packed bed, Int. J. Heat Mass Trans, 33;1247-61.

41. Liu KC, Cheng PJ (2008). Finite propagation of heat transfer in multilayer tissue. J Thermophys Hear Transf, 22:775-82.

42. Kaminski W (1990). Hyperbolic heat conduction equation for materials with a nonhomogenous inner structure. J Heat Transf, 112:555-60.

43. Luikov AV. Analytical Heat Diffusion Theory. New York, NY: Academic Press (1968).

44 Mitra K, Kumar S, Vedavarz A, Moalemi MK (1995). Experimental evidence of hyperbolic heat conduction in processed meat. J Heat Transfer, 117:568-73.

45. Davidov EV, Lubashevsky IA, Milyaev IA, Musin RF (2001). Nondiffusive heat transfer in muscle tissue. Preliminary results. arXiv.

46. Banerjee A, Ogale AA, Das C, Mitra K, Subramanian C (2005). Temperature distribution in different material due to short pulse laser. Heat Transf Eng, 26:41-9.

---

47. Xu F, Lin M, Lu TJ (2010). Modelling skin thermal pain sensation: role of non-Fourier thermal behaviour in transduction process of nociceptor. Comp Biol Med, 40:478-86.

48. Liu J, Chen X, Xu LX (1999). New thermal wave aspects on burn evaluation of skin subjected to instantaneous heating. IEEE Trans Biomed Eng, 46:420-8.

49. Yang WH (1993). Thermal (Heat) shock biothermomechanical viewpoint. J Biomed Eng, 115:617-21.

50. Fabrizio M, Franchi F. Delayed thermal models: stability and thermodynamics. J Ther Stress, 37:160–73.

51. Cheng L, Xu M, Wang L (2008). From Boltzmann transport equation to single phase-lagging heat equation. Int J Heat Mass Transf, 51:6018–23.

52. Tzou DY. Macro- to Microscale Heat Transfer: The Lagging Behaviour. Washington, DC: Taylor and Francis (1997).

53. Ezzat MA, Al-Sowayan NS, Al-Muhiameed ZIA, Ezzat SM (2014). Fractional modelling of Pennes' bioheat transfer equation. Heat Mass Transf, 50:907–14.

54. Ezzat MA, El-Barry AA, Al-Sowayan NS (2016). Tissue responses to fractional transfer heating with sinusoidal heat flux condition on skin surface. Anim Sci J. 10:1304-11.

55. Jumarrie GD (2010). Derivation and solutions of some fractional Black-Sholes equations in coarse-grained space and time, applications of Merton's optimal portfolio. Comput Math Appl, 59:1142-64.

56. Damor RS, Kumar S, Shukla AK (2016). Solution of fractional bioheat equation in terms of Fox's H-function. SpingerPlus, 5:111.

---

57. Ferrás LL, Ford NJ, Morgado ML, Nóbrega JM, Rebelo MS (2015). Fractional Pennes’ bioheat equation: theoretical and numerical studies. Frac Cal Appl Anal, 18:1080-06.

58. Hristov J (2019). Bio-heat models revisited: concepts, derivations, nondimensionalization and fractionalization approaches. Front Phys 7:198.

59. Gurtin ME, Pipkin AC (1968). A general theory of heat conduction with finite wave speeds. Arch Rat Mech Anal, 31:113-26.

60. Neufeld E, Paulides MM, Rhoon G. C. v., Kuster N (2013). Numerical Modeling for Simulation and Treatment Planning of Thermal Therapy, in Imag. Med. Diag. Ther, Taylor & Francis, 119-138.

61. Arkin H, Xu LX, Holmes KR (1994). Recent developments in modeling heat transfer in blood perfused tissues. IEEE Trans. Biomed. Eng, 41(2), 97-107.

CHAPTER 5

Research Materials and Methods

Chapter 5

Research materials and methods

Research materials and methods used in this thesis were guided chiefly by the aims and objectives stated in chapter 3, balanced with availability of materials, time constraints, financial constraints, logistical constraints, and access to supplementary expertise/services, to mention a few. The preferred research method for this thesis was numerical analysis of heat-transfer, and materials and methods chosen had to be consistent with this method.

5.1 Research Materials

5.1.1. 3D Computational Phantoms

As stated in chapter 3, one of the objectives of this thesis was to use as a human surrogate a 3D computational phantom that expressly consisted of multiple anatomically-segmented organs. Human 3D phantoms suitable for numerical analysis are obtainable from a number of sources and are applied predominantly as finite elements models for a wide variety of applications. Such phantoms are often applied either as the full human body or as regions or organ systems depending on the aims and objectives of the study concerned. 3D computational phantoms that met requirements of this thesis were four high-resolution 3D phantoms of an adult male, an adult female, a prepubescent female child, and a male child, collectively known as the version 3.0 Virtual Family[1], see Fig. 5.1. The phantoms were sourced from IT'IS Foundation, Switzerland (https://itis.swiss/virtual-population/virtual-population/vip3/) and were built from magnetic resonance images (MRIs) of healthy, living volunteers. These phantoms were part of a larger group of phantoms called The Virtual Population (ViP). Table 5.1 indicates the name, age, height, weight, sex, and body mass index (BMI) for each phantom. Organs were segmented to a high resolution by separation of their constitutional sub-parts, resulting in >200 anatomically named organs domains.

5.1.2 Verification and Validation of 3D Computational Phantoms

Credibility assessment of simulations include verification and validation, among other aspects such as applicability analysis and quality assurance[2]. Verification enquires whether the 3D computational phantom was applied correctly or as intended, while validation enquires whether the correct 3D computational phantom was applied[2]. According to the ASME V&V40[3], the objective of verification is to ensure that a 3D computational phantom is implemented correctly and then accurately solved. The objective of validation is to assess the accuracy of the prediction as compared to real world experimental data. Definitive verification and validation of 3D computational phantoms occurs along a simulation and in the context of an application, mainly as part of the assessment of model form and model inputs, e.g. anatomical geometries, tissue properties, and solution verification such as discretization errors[2]. Verification of the Virtual Family phantoms used in this thesis, as released in the quality assurance report[4], provides an assessment of the MRI image segmentation quality and processes by anatomical experts. Assessment of the fidelity of extracted surfaces and simplified surfaces of the 3D computational phantoms is described by Gosselin et al[1].

Ideally, validation of the 3D computational phantoms requires human experimentation as well as, in the case of this thesis, both living and deceased persons. The best-case validation scenario for this thesis was to use the same human subjects whose MRI scans were used to build the 3D computational phantoms. However, that was not possible due to a number of practical and obvious reasons.

The next best-case validation scenario was to use human subjects whose age, race and anthropometric features were comparable to human subjects of the 3D computational phantoms. Unfortunately, this too was not possible due to various logistical or legal reasons. The third best-case validation scenario was to compare simulation predictions with measurements obtained from an experimental setup that represents the use-case scenario. The third scenario would be a compromise between being as close as possible to the real application and context-of-use (to reduce the necessary leap-of-faith and safety margin) and offering optimal experimental control, validation sensitivity, and data richness, at an affordable effort/cost[2]. For the third scenario, this thesis used a cooling dummy as a physical human thermal phantom representing a decedent, discussed in detail in chapter 8. For the antemortem study, simulation results are compared to comparable empiric data from the literature (chapter 6).

The chosen 3D computational phantoms were verified by numerous experimental studies: Liorni et al[5] proposed a novel method and procedure for evaluating compliance of sources with strong gradient magnetic fields, such as wireless power transfer systems, which mitigates overestimation of human exposure while maintaining simplicity of the testing procedure using the ViP phantoms Duke, Billie, Nina and Fats. Nadakuduti et al[6] described a compliance testing methodology for wireless power transfer systems using the four Virtual Family phantoms. Kyriakou et al[7] applied Duke’s head to model full-wave acoustic and thermal transcranial ultrasound propagation. Murbach et al[8] modelled radio frequency exposure on pregnant female 3D computational phantoms.

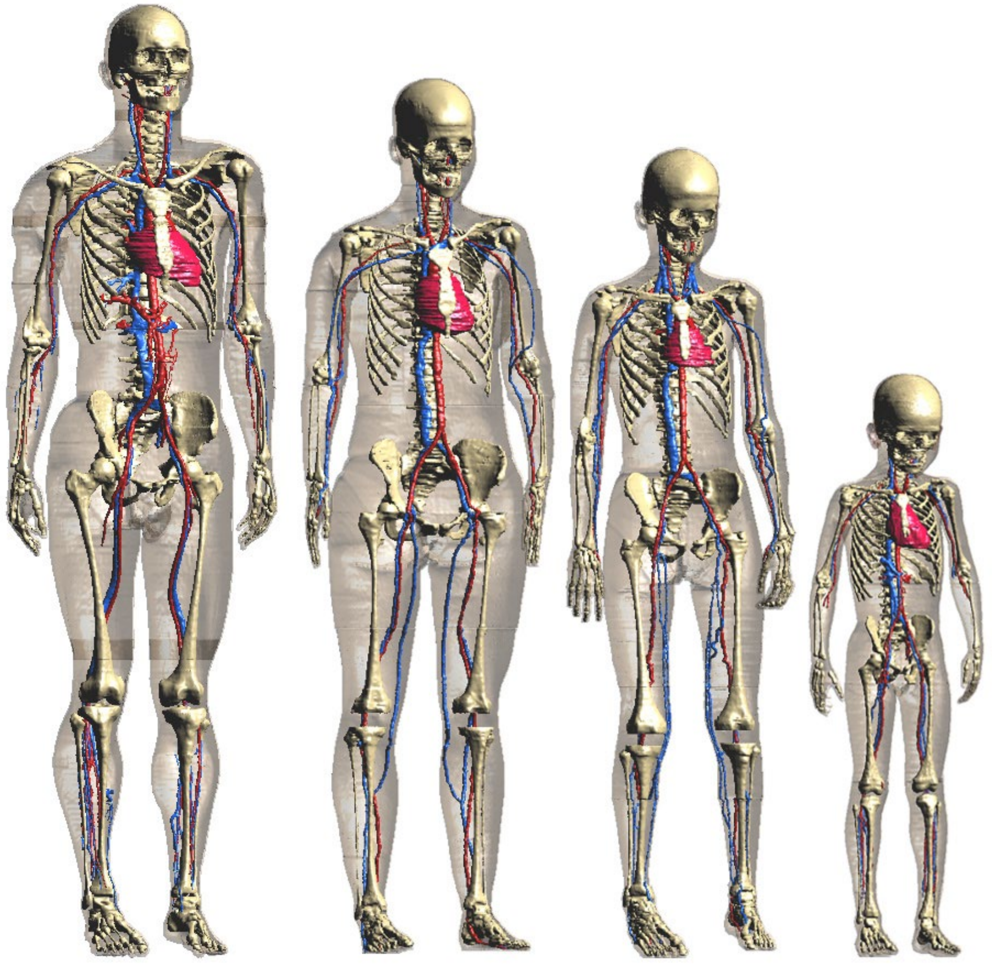

Fig. 5.1 The Virtual Family V3.0 phantoms (left to right): Duke, Ella, Billie, and Thelonious

Table 5.1 The name, weight, height, age, and BMI of each Virtual Family computational phantom.

Phantom	Weight	Height	Age	Sex	BMI
Duke	70.2kg	1.77m	34 years	M	22.4 kgm^{-2}
Ella	57.3kg	1.63m	26 years	F	21.6 kgm^{-2}
Billie	34.0kg	1.49m	11 years	F	15.3 kgm^{-2}
Thelonious	18.6kg	1.16m	6 years	M	13.8 kgm^{-2}

5.1.2 Thermal analysis software

A thermodynamic solver is computer software that solves heat transfer problems involving specified geometries based on physical laws that govern heat transfer by thermal conduction, thermal convection, and thermal radiation. Such geometries may be a novel prototype or an untested design that is either too expensive to build in the physical world or too complex for detailed laboratory analysis. Many thermal solvers are commercially available for licensed application. The thermodynamic solver used in this thesis was P-Thermal® and was an integral part of a larger bio-physics simulation platform called Sim4Life®[9] from Zurich MedTech, Switzerland (https://zmt.swiss/sim4life/). The P-Thermal® solver was based on Poisson differential equation and enabled modelling of heat transfer in living tissue with a set of flexible boundary conditions.

5.1.3 Validation and Verification of the Thermodynamic Solver

Validation of the P-Thermal® solver is contained in a validation benchmark report[10] in which theoretical solutions and corresponding simulation results of four scenarios are reported. The P-Thermal® solver was verified in experimental studies by comparison with analytically solvable cases, experimental measurements under controlled conditions and *in vivo* measurements. For example, Murbach et al[11] demonstrated the application of the P-Thermal® solver in modelling magnetic resonance imaging (MRI) radiofrequency (RF)-exposure induced tissue heating for safety assessment, considering local thermoregulation by vasodilation. They provided comparison against in *vivo* measurements and provided detailed uncertainty assessment considerations. In another verification study, Nuefeld et al[12] applied the P-Thermal® solver to the investigation of RF-exposure related to heating in the presence of implants, with a particular focus on wires and leads. In that study, a thin structure model, previously verified by Nuefeld[13], was used to facilitate the modelling of setups featuring thin, highly thermo-conductive wires. This verification study also provided detailed uncertainty assessment considerations. The staircasing-effect correction approach used in the P-Thermal® solver and its implantation was verified by Nuefeld et al[14].

Other studies that verified the P-Thermal® solver include design and optimization of ultrasonic therapy[7], assessment of medical device safety in MRI[15], RF-hyperthermia liver tumour treatment simulation[16], prediction of tumour temperature in regional hyperthermia by using LED luminance[17], temperature impact on neuronal dynamics[18], etc. The transient thermal solver of the P-Thermal® solver used in this thesis assumed that a transient state existed in the 3D computational phantom, which required all tissue domains to have non-zero thermal conductivity or non-zero heat transfer rates. Several versions of Sim4Life® were used over the course of this study.

5.1.4 Computer hardware

Simulations were carried out in a 2015-model Apple Mac Pro computer that had a 12-core 3.5GHz processor, a 128GB RAM and ran 64-bit Windows 8.1-10. Simulation data were stored in a 10TB external hard drive.

5.2 Research Methods

The numerical approach applied in this thesis was the finite difference time domain (FDTD) method, whose detailed explanation is beyond the scope of this thesis.

5.2.1 Bioheat modelling to approximate body temperature at death

In this thesis, bioheat modelling was applied in a transient/unsteady-state thermal analysis to model antemortem temperature distribution in the four 3D computational phantoms after thermal equilibration with the external environment. Transient or unsteady-state analysis is a numeric approach used to determine either the interval of heat transfer required for temperature equilibration between objects of different temperatures, or to predict the temperature-field of an object after thermal equilibration with another object of different temperature, or to predict the temperature-field of an object after a specified interval of heat-transfer with another object of a different temperature. The bioheat model selected for this thesis was that described by Pennes[19], as already discussed in chapter 4. The PBE was to be applied to each organ-domain in a 3D computational phantom. Heat generated by each organ-domain via the metabolic heat generation rate would spread to adjacent organs by thermal diffusion as well as blood perfusion. The combination of endogenous metabolic heat production, heat transfer by blood flow, heat conduction between different solid organs, and heat transfer from skin to the surrounding air by thermal convection, radiation and/or conduction would thus determine the final overall temperature filed of the 3D computational phantoms. The Pennes bioheat model required thermophysical and biothermal parameters in the governing equation for each organ-domain. Thermophysical parameters were density, specific heat, and thermal conductivity. Biothermal parameters were metabolic heat generation rates and blood perfusion rates. These parameters are obtainable from several sources, and for this thesis were obtained from IT'IS Foundation, Switzerland[20] (Appendix 1). The parameters included non-tissue constituents such as urine, respiratory tract air, bile, and gastrointestinal contests, all of which coexist with the body under normal circumstances during antemortem and postmortem heat transfer. Mean values were applied in this study.

On the skin, boundary conditions that specified the thermal conditions were applied, namely the Dirichlet (far field air has a fixed temperature), Neumann (heat transfer from body to air is purely due a heat transfer coefficient), and Mixed (Dirichlet plus Neumann) boundary conditions. In a Mixed boundary conditions the convective heat flux is the product of the heat transfer coefficient and local temperature difference between skin and air temperatures. Mixed boundary condition work well for modelling effects of stagnant convection, i.e. in the absence of wind and natural convection. In a Mixed boundary condition, the convective heat flux is the product of the heat transfer coefficient (e.g. radiative heat flux) and local temperature difference between skin and air temperatures. A mixed boundary condition is expressed mathematically as:

$$\frac{kdT_s}{dn} + h(T_s - T_a) = F_{Boundary} \qquad (5.1)$$

where T_s represents skin temperature, T_a represents ambient temperature and h the heat transfer coefficient. Exchange of the radiative heat is derived from the Stefan and Boltzmann equation, in the form:

$$\sigma(T_s^4 - T_a^4) \tag{5.2}$$

where σ is the Stefan-Boltzmann constant (5.670373 x 10^{-8} Wm^{-2} K^{-4}). Eqn. (5.2) can be expressed as:

$$\sigma(T_s^4 - T_a^4) = \sigma(T_s - T_a)(T_s + T_a)(T_s^2 + T_a^2) \tag{5.3}$$

For small temperature differences, eqn. (5.3) can be approximated as:

$$4\sigma(T_s - T_a)T_a^3 \tag{5.4}$$

and prescribed as part of the mixed boundary condition as:

$$h = 4\sigma T_a^3 \tag{5.5}$$

5.2.2 Transient analysis to study postmortem axial heat transfer

In this thesis, the Pennes bioheat model was also applied in transient numerical analysis studies to model axial postmortem heat transfer, but in which the metabolic heat generation rates and blood perfusion rates (biothermal parameters) were set to zero to simulate a state of death, and in which the antemortem axial temperature distribution predicted earlier was applied in initial conditions. Assigning zero values to the biothermal parameters, the PBE [eqn. (4.2)] reduces to:

$$\rho_t C_t \frac{\partial T_{ti}}{\partial t} = \nabla \cdot (k_t \nabla T_{ti}), \tag{5.6}$$

where:

$$\nabla = \frac{\partial}{\partial x}\widehat{ix} + \frac{\partial}{\partial y}\widehat{iy} + \frac{\partial}{\partial z}\widehat{iz} \tag{5.7}$$

Eqn. (5.7) is written in 'strong' form as it holds in a point. To apply it in numerical analysis we however cast it into the 'weak' form by integrating over a volume V(e.g. a cube around a voxel):

$$\int \rho_t C_t \frac{\partial T_{ti}}{\partial t} dV = \int_V \nabla \cdot (k_t \nabla T_{ti})\, dV \tag{5.8}$$

As V does not change in position or size over time, we can rewrite the left-hand side of eqn. (5.8) as:

$$\int \rho_t C_t \frac{\partial T_{ti}}{\partial t} dV = \frac{\partial}{\partial t}\int_V \rho_t C_t \frac{\partial T_{ti}}{\partial t}\, dV \tag{5.9}$$

For cell-centred finite-volume (e.g. the FDTD method used in Sim4Life®), all properties at cell centres can be further approximated as:

$$\frac{\partial}{\partial t}\int_V \rho_t C_t \frac{\partial T_{ti}}{\partial t}\, dV \approx \frac{\partial}{\partial t}(\rho_t C_t T_{ti})V \tag{5.10}$$

for a specific voxel. Because thermophysical properties remain constant with time, then eqn. (5.10) can further be simplified to:

$$\frac{\partial}{\partial t}(\rho_t C_t T_{ti})V = \rho_t C_t \frac{\partial T_{ti}}{\partial t} V \tag{5.11}$$

where ρ_t and C_t have been removed from the temporal derivative. To deal with the spatial term, we looked at the 'weak' form by integrating over a volume V (e.g. a cube around a voxel) and applying the divergence theorem:

$$\int_V \nabla \cdot (k_t \nabla T_{ti}) dV = \int_A k_t \nabla T_{ti} \cdot n_\wedge \, dA \,\ldots. \tag{5.12}$$

where:

$$n_\wedge = n_x \hat{e}_x + n_y \hat{e}_y + n_z \hat{e}_z \tag{5.13}$$

is a unit vector normal to the surface A enclosing V:

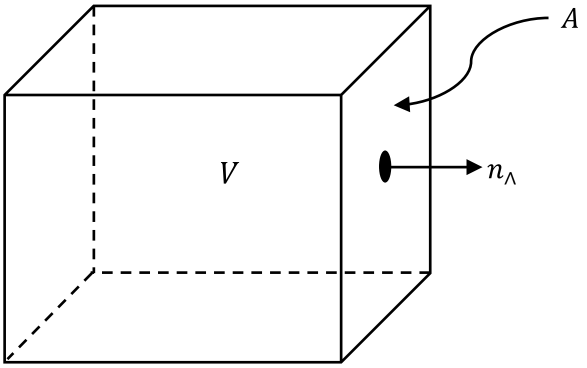

where A is the particular face segment of V, of which there are six for a voxel. Eqn. (5.12) may be expressed as:

$$\int_V \nabla \cdot (k_t \nabla T_{ti}) dV = \int_A Q\, dA \tag{5.14}$$

where Q is heat flux per square meter (W/m^2). There are two types of surface areas:

1) A surface area between two voxel tubes, in which the heat flux can be expressed as:

$$Q = k_t \nabla T_{ti} \cdot n_{\wedge} = \frac{\partial T_{ti}}{\partial n_{\wedge}} \tag{5.15}$$

2) A surface area which sits on the skin, in which the heat flux can be expressed as:

$$Q_c = h_c(T_{air} - T_{skin}) \tag{5.16}$$

or as

$$Q_r = \sigma(T_{air}^4 - T_{skin}^4) \approx h_r(T_{air} - T_{skin}) \tag{5.17}$$

where Q_c is heat flux by thermal conduction, Q_r is heat flux by thermal radiation, h_c is the convective heat transfer coefficient, h_r is the radiative heat transfer coefficient, σ is the Stefan-Boltzmann constant (5.670373 x 10^{-8} Wm^{-2} K^{-4}), T_{air} is temperature of the air in contact with the skin, and T_{skin} is temperature of the skin in contact with the air. Integrating eqns. (5.15) and (5.16) for convective heat transfer therefore gives:

$$Q_c = k_t \frac{\partial T_{ti}}{\partial n_{\wedge}} = h_c(T_{air} - T_{skin}) \tag{5.18}$$

and integrating eqns. (5.15) and (5.17) for radiative heat transfer gives:

$$Q_c = k_t \frac{\partial T_{ti}}{\partial n_{\wedge}} = h_r(T_{air} - T_{skin}) \tag{5.19}$$

When both convective and radiative heat transfer are present on the skin:

$$Q = (h_c + h_r)(T_{air} - T_{skin}) \tag{5.20}$$

which represents a mixed boundary condition if and are both specified.

5.2.3 Simulation Sequence

Each numerical simulation undertaken in this thesis consisted of the following ten sequential steps:

5.2.3.1. **Phantom Import:** in which the desired 3D computational phantom was loaded into the thermal solver and its orientation could be edited.

5.2.3.2. **Simulation Interval:** in which the length of the simulation was set.

5.2.3.3. **Sensors:** represented points along the simulation interval at which the simulation could be examined during post-processing.

5.2.3.4. **Organ Parameters:** in which thermophysical and biothermal values of each organ-domain or model-object were defined.

5.2.3.5. **Initial Conditions:** in which the overall temperature of an organ-domain or model-object was specified. The temperature distribution solved by another simulation could be set as the initial condition.

5.2.3.6. **Boundary Conditions:** in which the applicable boundary condition was specified as either Dirichlet, Neumann or Mixed (Dirichlet plus Neumann). The heat transfer coefficient and surrounding temperature were specified in this step.

5.2.3.7. **Grid Design:** in which a gird was designed around an organ-domain or model-object, whose refinement could be define between **extremely fine**, **very fine, fine, normal, coarse,** and **very course**. In this study, grid design was generally undertaken using an automated tool of the thermal solver.

5.2.3.8. **Voxels Creation:** in which the surface triangle mesh of each organ-domain and the grid were used together to generate voxels for each organ-domain. A voxel is a single data point that contained scalar values of thermophysical and biothermal parameters for each organ-domain. For organ-domain volume, the mesh was assumed to be closed. For organ-domain surface, the mesh was assumed to be opened in which stair approximation was generated. In this study, voxel creation was generally undertaken using an automated tool of the thermal solver.

5.2.3.9. **Simulation Run:** in which the simulation was initiated.

5.2.3.10. **Post-processing:** in which the simulation solution was analysed at specific sensor-points with the help of several thermal solver tools.

Bibliography and References Cited

1. Gosselin M, Neufeld E, Moser H, Huber E, Farcito S, Gerber L, Jedensjö M, Hilber I, Di Gennaro F, Lloyd B, Cherubini E, Szvzerba D, Kainz W, Kuster N (2014). Development of a new generation of high-resolution anatomical models for medical device evaluation: the Virtual Population 3.0. Physics in Medicine and Biology, 5287-5303.

2. Kainz W, Neufeld E, Bolch WE, Graaf CG, Kim CH, Kuster N, Lloyd B, Morrison T, Segars P, Yeom YS, Zankl M, Xu XG, Tsui BMW (2009). Advances in Computational Human Phantoms and Their Applications in Biomedical Engineering – A Topical Review. IEEE Trans Radiat Plasma Med Sci. 3(1): 1-23.

3. ASME V&V 40, "Assessing credibility of computational models through verification and validation: application to medical devices," [Online]. Available: http://go.asme.org/VnV40Committee.

4. Farcito S, Lloyd B, Kuster N (2017). "Verification Report VIP001AA201704: Virtual population models V3.x verification of anatomy, physiology and segmentation/generation procedures," IT'IS Foundation, Zurich, Switzerland.

5. Liorni I, Lisewski T, Capstick M, Kühn S, Neufeld E, Kuster N (2019). Novel method and procedure for evaluating compliance of sources with strong gradient magnetic fields such as wireless power transfer systems. IEEE Transactions on Electromagnetic Compatibility, 56(5): 1027-1034.

---

6. Nadakuduti J, Douglas M, Lu L, Christ A, Guckian P, Kuster N ((2015). Compliance testing methodology for wireless power transfer systems. IEEE Transactions on Power Electronics, PP(99):1-1

7. Kyriakou A, Neufeld E, Werner B, Székely, Kuster N (2015). Full-wave acoustic and thermal modeling of transcranial ultrasound propagation and investigation of skull-induced aberration correction techniques: a feasibility study. Journal of therapeutic ultrasound 1-18.

8. Murbach M, Neufeld E, Samaras T, Córcoles J, Robb FR, Kainz W, Kuster N (2017). Pregnant women models analyzed for RF exposure and temperature increase in 3T RF shimmed birdcages. Magnetic Resonance in Medicine, 2048-2056.

9. ZMT Zurich MedTech AG (2020). Sim4Life Documentation Release 5.2. Sim4Life Application and Support Team.

10. Szolnoki L, Neufeld E, Kuster N (2018). Foundation for Research on Information Technologies in Society. Sim4Life and SEMCAD Thermal Solver (Verification Report TS002AA201812).

11. Murbach M, Neufeld E, Capstick M, Kainz W, Brunner DO, Samaras T, Pruessmann KP, Kuster N (2013). Thermal tissue damage model analyzed for different whole-body SAR and scan durations for standard MR body coils. Magnetic Resonance Medicine 1-11.

12. Neufeld E, Kühn S, Szekely G, Kuster N (2009). Measurement, simulation and uncertainty assessment of implant heating during MRI. Phys. Med. Biol. 54, 4151-4169.

13. Neufeld E (2008). High resolution hyperthermia treatment planning phd thesis eth no. 17947: Swiss Federal Institute of Technology.

14. Nuefeld E, Chavannes N, Samaras T, Kuster N (2007). Novel conformal technique to reduce staircasing artifacts at material boundaries for FDTD modeling of the bioheat equation. Phys. Med. Biol. 52(15):4371.

15. Kabil J, Belguerras L, Trattning S, Pasuier C, Felblinger J, Missoffe A (2016). A Review of Numerical Simulation and Analytical Modeling for Medical Devices Safety in MRI. Yearb Med Inform (1): 152-158.

16. Prasad B, Ha YH, Lee SK, Kim JK (2016). Patient-specific simulation for selective liver tumor treatment with noninvasive radiofrequency hyperthermia. Journal of Mechanical Science and Technology 30(12), 5837-5845.

17. Lee J, Seol Y, Oh T, An NY, Han K, Hwang J, Jang HS, Choi BO, Kang Y (2020) Prediction of Tumor Temperature in Regional Hyperthermia by Using LED Luminance. Journal of the Korean Physical Society, 77, 524-529.

18. Nuefeld E, Kuster N (2014). Platform for the modeling of in vivo effects relevant to implant em exposure safety. IEEE International Symposium on Electromagnetic Compatibility, 230-233.

19. Pennes HH (1948). Analysis of tissue and arterial temperatures in the resting human forearm. Journal of Applied Physiology, 93-122.

20. Hasgall PA, Di Gennaro F, Baumgartner C, Neufeld E, Lloyd B, Gosselin MC, Payne D, Klingenböck A, Kuster N. IT'IS Database of thermal and thermomagnetic parameters of biological tissue. Version 4.0 May 15, 2018. DOI: 10.13099/VOP21000-04-0. itis.swiss/database.

CHAPTER 6

Numerical approximation of antemortem body temperature

Chapter 6

Numerical approximation of antemortem body temperature

The hypothesised effect of antemortem axial temperature distribution on postmortem cooling were discussed in chapter 1 of this thesis. This chapter discusses numerical approximation of antemortem body (and thus axial) temperature under natural convection by assigning metabolic heat production and blood perfusion rates to individual organ-domains.

6.1 Transient Simulation Setup

6.1.1 Phantom Import

The 3D computational phantoms Duke, Ella, Billie, and Thelonious were used in this chapter, bringing the number of simulations undertaken to four. The phantoms were placed standing in a neutral position with no contact with any external solid surface.

6.1.2 Simulation Interval

Simulation intervals long enough to simulate complete thermal equilibration between each 3D computational phantom and surrounding air were not known in advance and were consequently established iteratively. Final simulation intervals applied are discussed under the results subheading.

6.1.3 Sensors

Two sensors were placed in each simulation, one at the beginning and the other at the end.

6.1.4 Organ Parameters

This study applied average/mean values of thermophysical and biothermal parameters from Annexure 1[1]. Each 3D computational phantom consisted of non-thermogenic organ-domains whose metabolic heat generation rates and blood perfusion rates were zero by default, viz. air, bile, blood, bronchi lumen, cerebrospinal fluid, cornea, lens, oesophagus lumen, non-infiltrated fat, heart lumen, large intestine lumen, pharynx, small intestine lumen, stomach lumen, trachea lumen, tooth and vitreous humour. The total mean metabolic heat generation rate for the 3D phantom Duke (70.2kg) was 154W, which was the equivalent of a 70kg individual jogging on level ground at 9 km/hr[2].

6.1.5 Initial Conditions

All the organ-domains were assigned an arbitrary initial temperature of 37°C for the four 3D phantoms.

6.1.6 Boundary Condition

The boundary condition type chosen for the four studies was 'mixed', the surrounding air temperature was 22°C and the heat transfer coefficient[3] was set at 3.4 $Wm^{-2}°C^{-1}$.

6.1.7 Grid Design

Discretization to transform the 3D computational phantoms to rectilinear meshes was performed using Sim4Life®'s rectilinear non-uniform gridding algorithm, which used ray-tracing and robust intersection testing, identified relevant structural features of the 3D computational phantom and then suggested a Cartesian grid that could neatly and properly resolve it. This ensured mesh-independent solutions. The grid refinement level applied was **normal**. The resolution of 3D computational phantoms was 10mm in the *xyz* axes. Final grid sizes for the four 3D computational phantoms are indicated in Table 6.1. Fig. 6.1 indicates the grid constructed around the 3D phantom named Duke.

3D phantom	Total cells (x10^7)	*x*-cells	*y*-cells	*z*-cells
Duke	3.4595	142	279	899
Ella	2.9675	142	253	826
Billie	2.2476	130	226	765
Thelonious	1.1863	109	187	582

Table 6.1 Grid sizes generated for each 3D computational phantom.

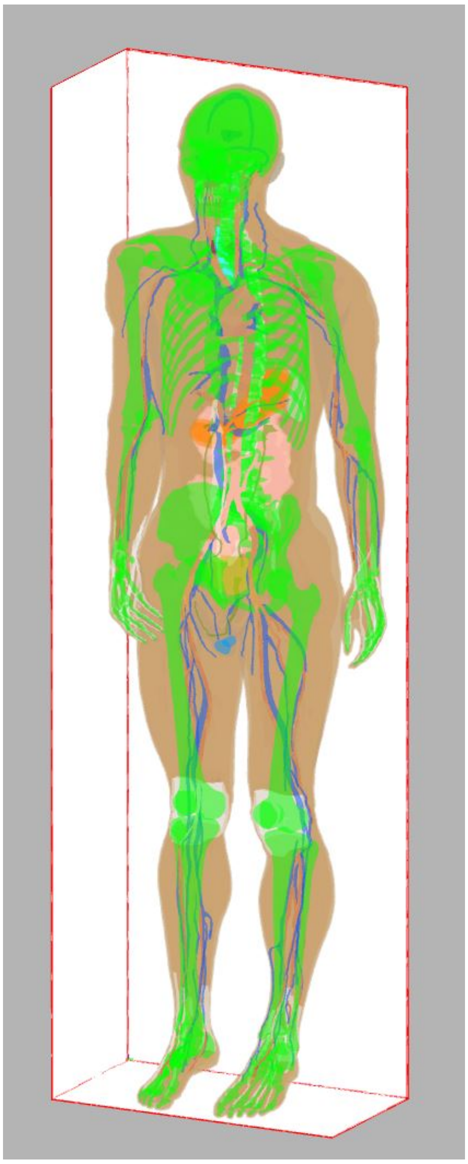

Fig. 6.1 The grid generated around Duke

6.2 Results and Discussion

6.2.1 Approximated organ temperature

Thermal equilibration was achieved after 9000s simulation interval. The predicted temperature fields of all organs showed spatial inhomogeneity, varying in the *xyz* coordinates. The inhomogeneity was also demonstrated in the predicted skin temperature whose vast surface area, external location and ready accessibility made it the organ of choice for comparison with normal skin temperatures cited in the literature. Figs. 6.2 to 6.5 indicate the predicted skin temperature of the 3D phantoms Duke, Ella, Billie, and Thelonious, respectively. The simulated inhomogeneity of skin temperature was consistent with that observed by infrared thermography[4]. Quantitative comparison of skin temperature predicted by these simulations against antemortem skin temperature distribution as described in the literature could not be undertaken due to wide range in which normal skin temperature flatulates as a result of the physical exertion, ambient temperature, skin moisture, clothing and prevailing thermoregulatory mechanisms. However, human skin temperature in air during exercise on a treadmill and at rest is also known to be inhomogeneously distributed[5]. Skin temperature of the adult male 3D phantom ranged from 20.6°C to 41°C, which were deemed within acceptable limits. Skin temperature in these simulations were predicted without being approximated by a linear gradient from 37°C at the vertex to 27°C at the distal ends of the limbs, as was done by Mall[6].

Although the meaning of ‘outer shell’ and ‘inner core’ may be colloquially understood in physiology and forensic pathology literature, the transition from one to the other was less clearly defined because anatomical landmarks or temperature limits did not form part of their definition. Literature on antemortem temperature of internal organs, for comparisons with our simulation results, proved scant. As of 2019, magnetic resonance thermal imaging (MRtI) was the only non-invasive modality found capable of measuring 3D temperature of individual internal organs in the living. However, literature on normal 3D temperature variations of internal organs at rest or during exercise (increased metabolism and blood flow) could not be found. Thus, comparative analysis of 3D temperatures of internal organs predicted by the numerical simulation in this chapter was precluded.

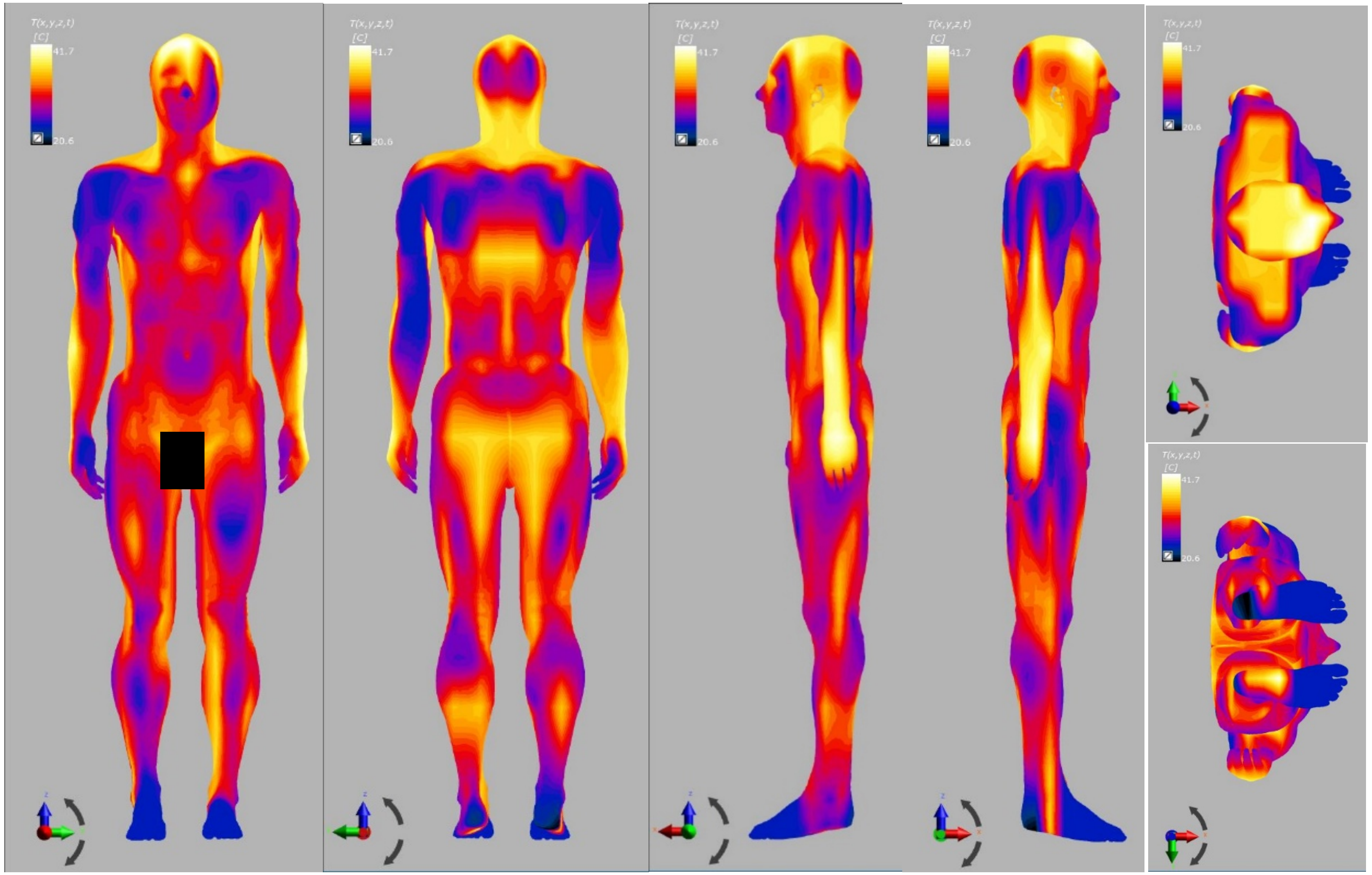

Fig. 6.2 Duke’s predicted skin temperature using average organ metabolic and perfusion rates (154W). From left to right: anterior, posterior, left, right, top (far-right top) and bottom (far-right bottom).

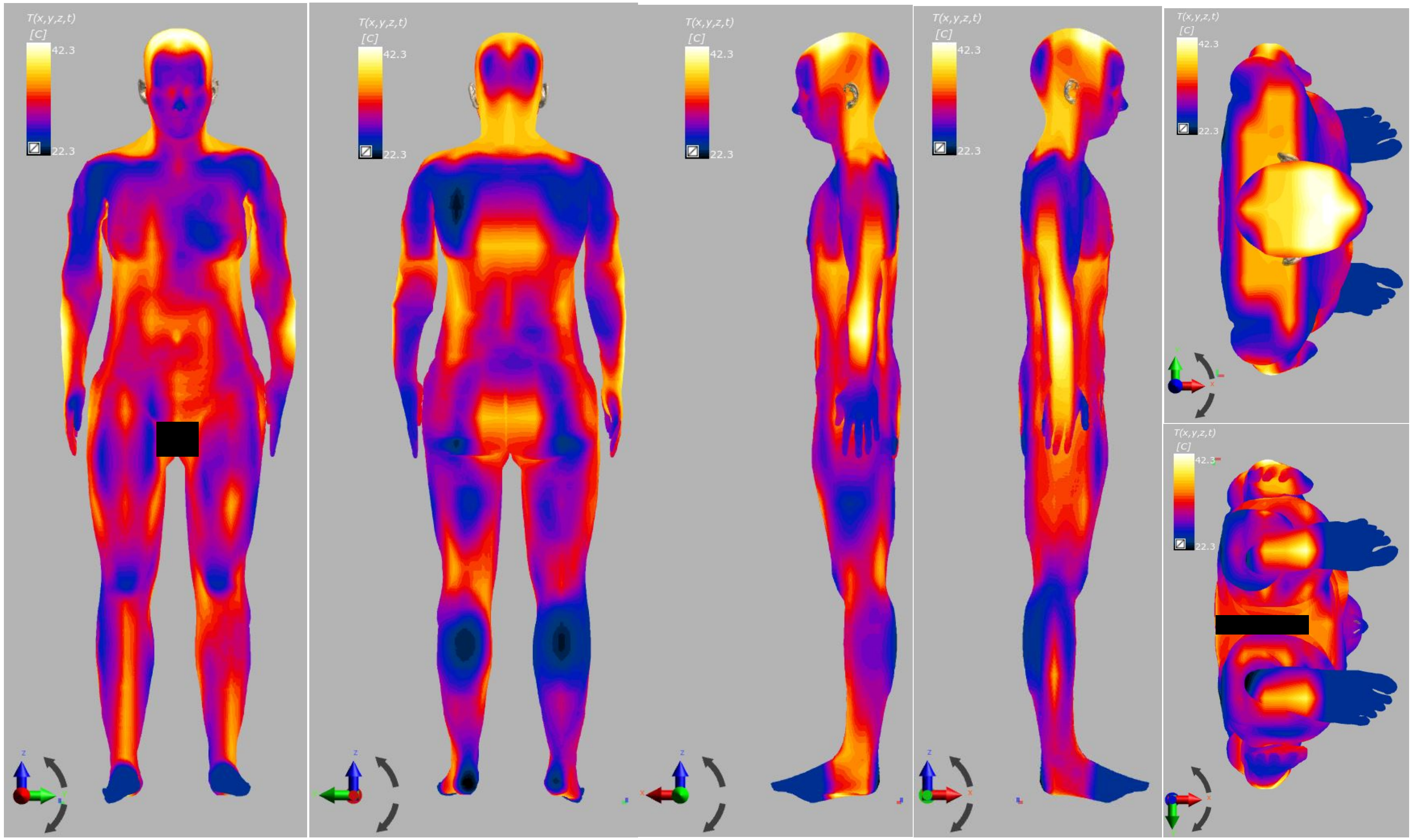

[redacted]

[redacted]

Fig. 6.3 Ella’s predicted skin temperature using average metabolic and perfusion rates. From left to right: anterior, posterior, left, right, top (far-right top) and bottom (far-right bottom).

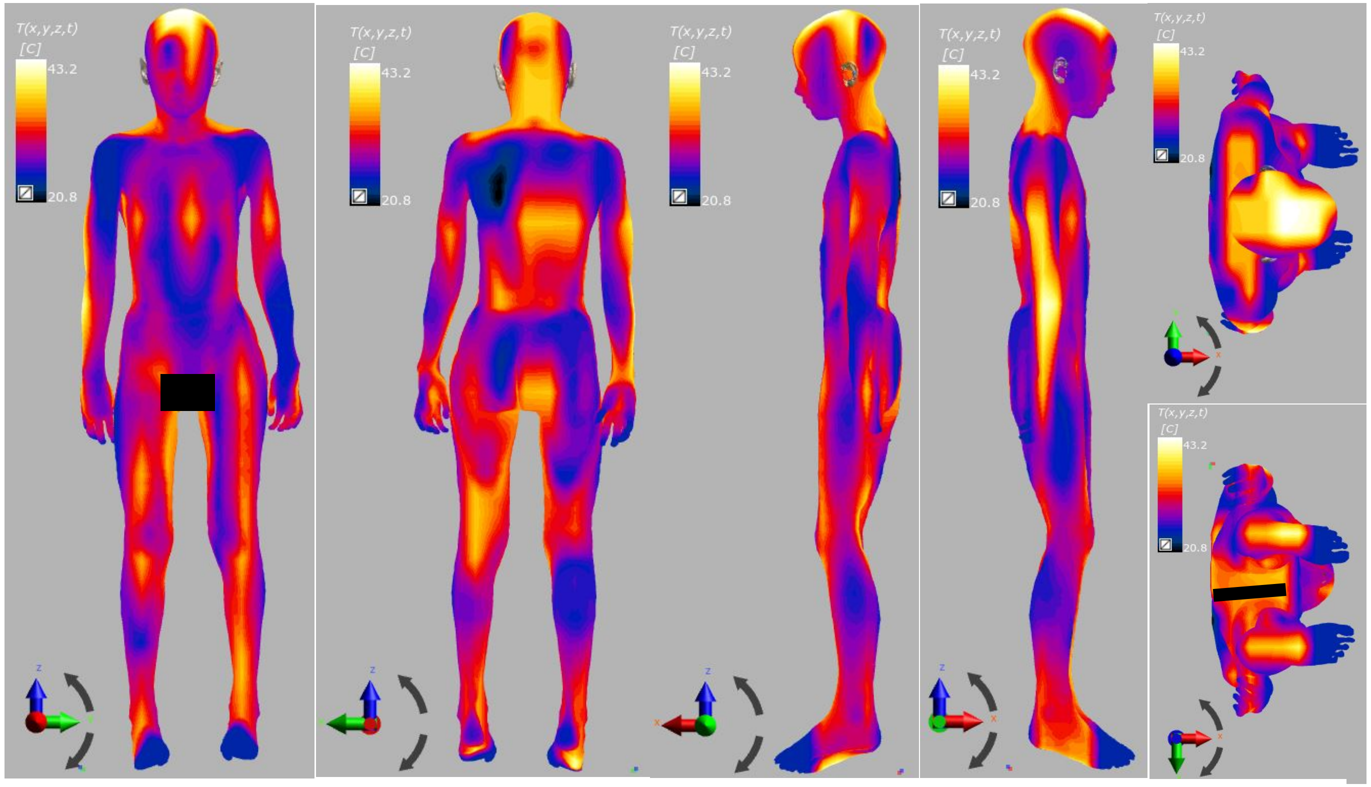

[redacted]

[redacted]

Fig. 6.4 Billie’s predicted skin temperature using average metabolic and perfusion rates. From left to right: anterior, posterior, left, right, top (far-right top) and bottom (far-right bottom).

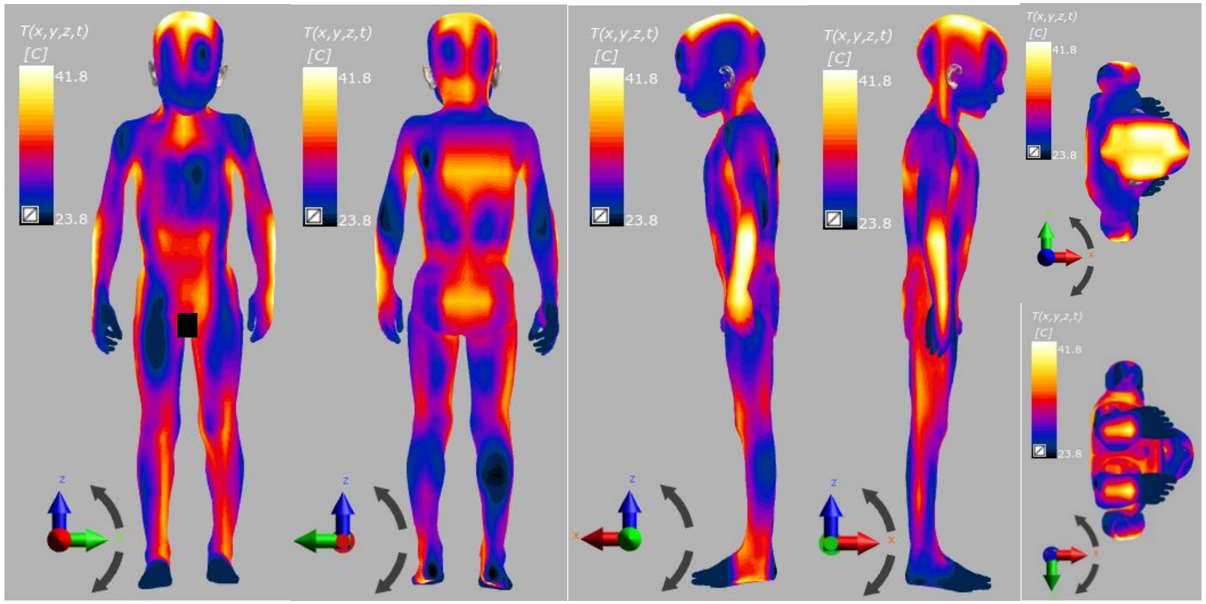

Fig. 6.5 Theolonues' predicted skin temperature using average metabolic and perfusion rates. From left to right: anterior, posterior, left, right, top (far-right top) and bottom (far-right bottom).

4.3.2 Approximated axial temperature distribution

Results from these simulations were consistent with the generally accepted principle that the living human body consists of a cooler ‘outer shell’ and a ‘hot core’. At any given axial section, the location and size of the central isotherm (hot core) appeared to be determined by the location, shape, and size of the most thermogenic organ there. For example, the organ domain that exhibited the highest temperature in the 3D phantom Duke at the chest level (1327mm from the ground) was **heart muscle,** while **heart lumen** and **aorta lumen** (both representing blood, a heat-sink term in the Pennes bioheat model) exhibited the lowest temperature, see Fig 6.6. Thus, the transcorporal one-dimensional (1D) axial temperature through the chest was nonlinear and differed and depended on the coronal (*yz*) and/or (para)sagittal (*xz*) plane selected for examination. Fig. 6.7 indicates 1D axial temperature curves of the chest plotted at various planes.

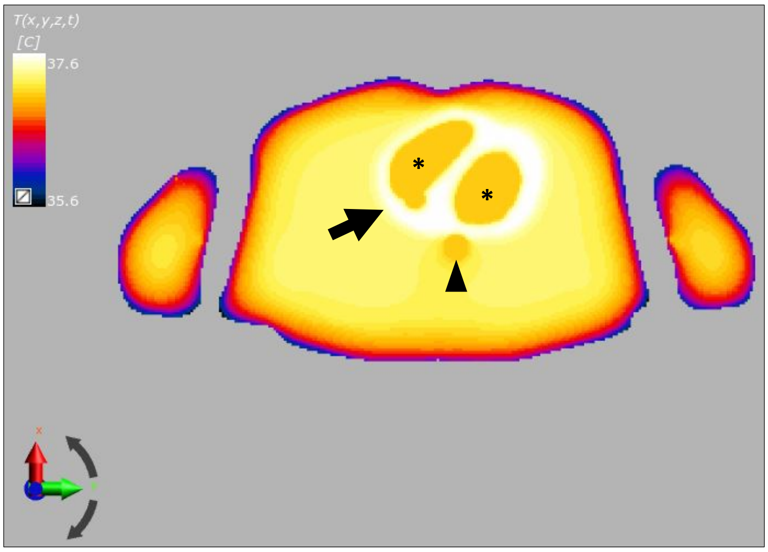

Fig. 6.6 The antemortem axial temperature distribution of Duke at the chest level. The arrow indicates **heart muscle**, the arrowhead indicates **blood** in descending thoracic aorta and the Asterix indicates **heart lumen**.

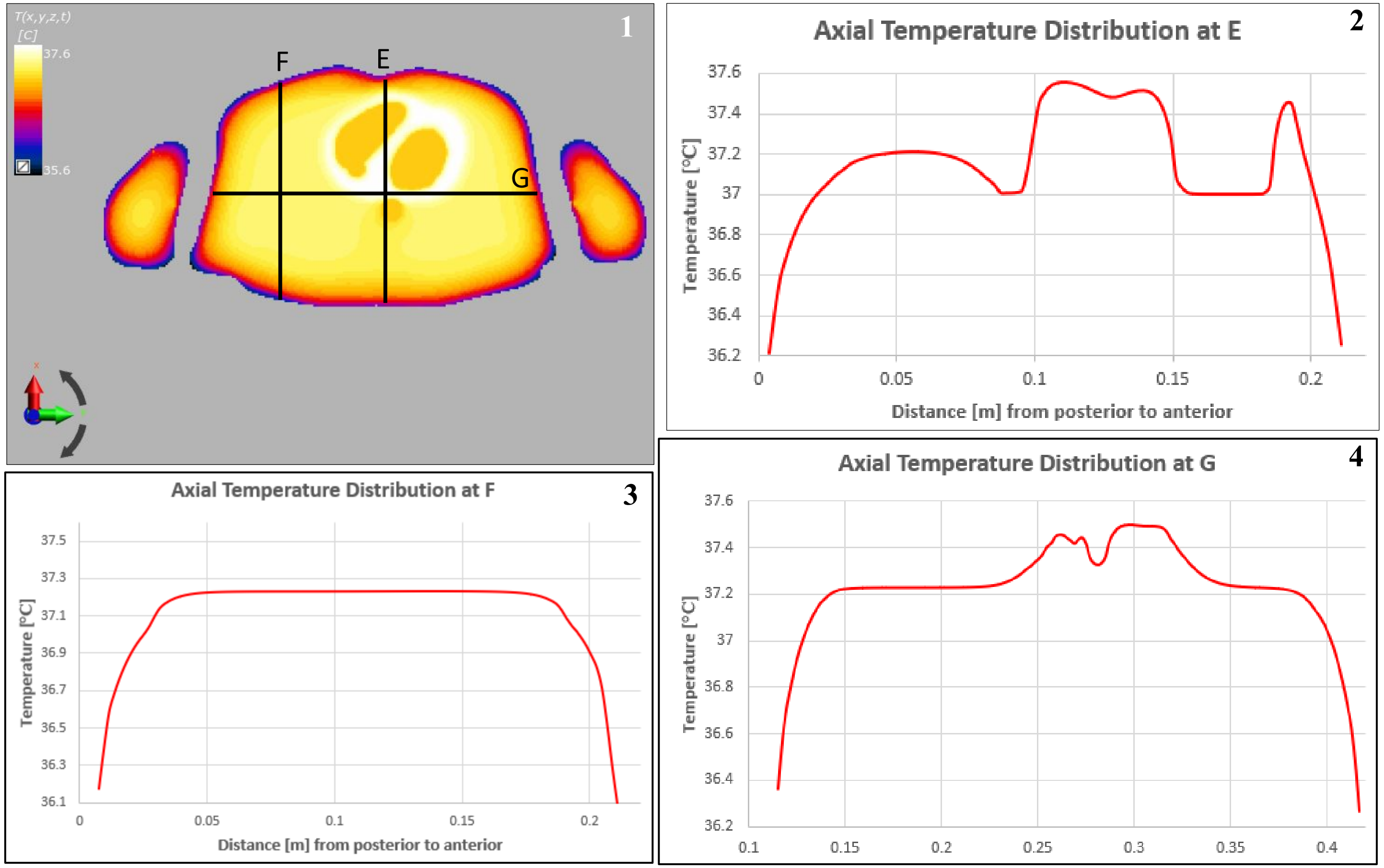

Fig. 6.7 One-dimensional antemortem axial temperature curves of Duke at the chest level. Fig. 6.7.1 indicates positions of 1-demsniosnal fields. Figs. 6.7.2 to 6.7.4 indicate 1D axial temperature curves from planes E, F and G, respectively.

At the lower abdominal level (1091mm), the organ-domain that exhibited the highest temperature was the **kidney**, characterised by two symmetrical posteriorly-located isotherm, see Fig 6.8. Here too, 1D axial temperature distribution differed according to the coronal (*yz*) and/or (para)sagittal (*xz*) plane selected for examination. Fig. 6.9 indicates 1D axial temperature curves of the lower abdomen plotted at various planes.

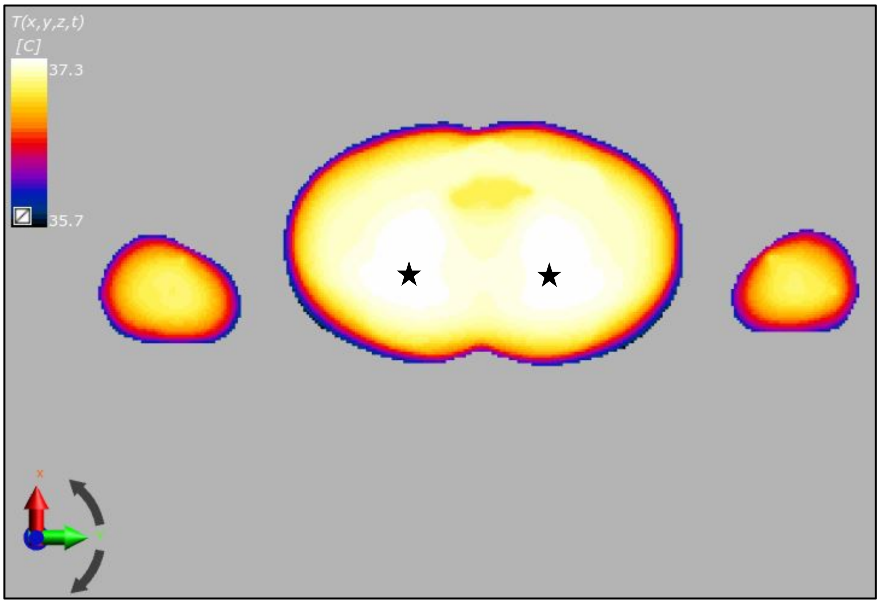

Fig. 6.8 The antemortem axial temperature distribution of Duke at the lower abdominal level. Stars indicate position of kidneys.

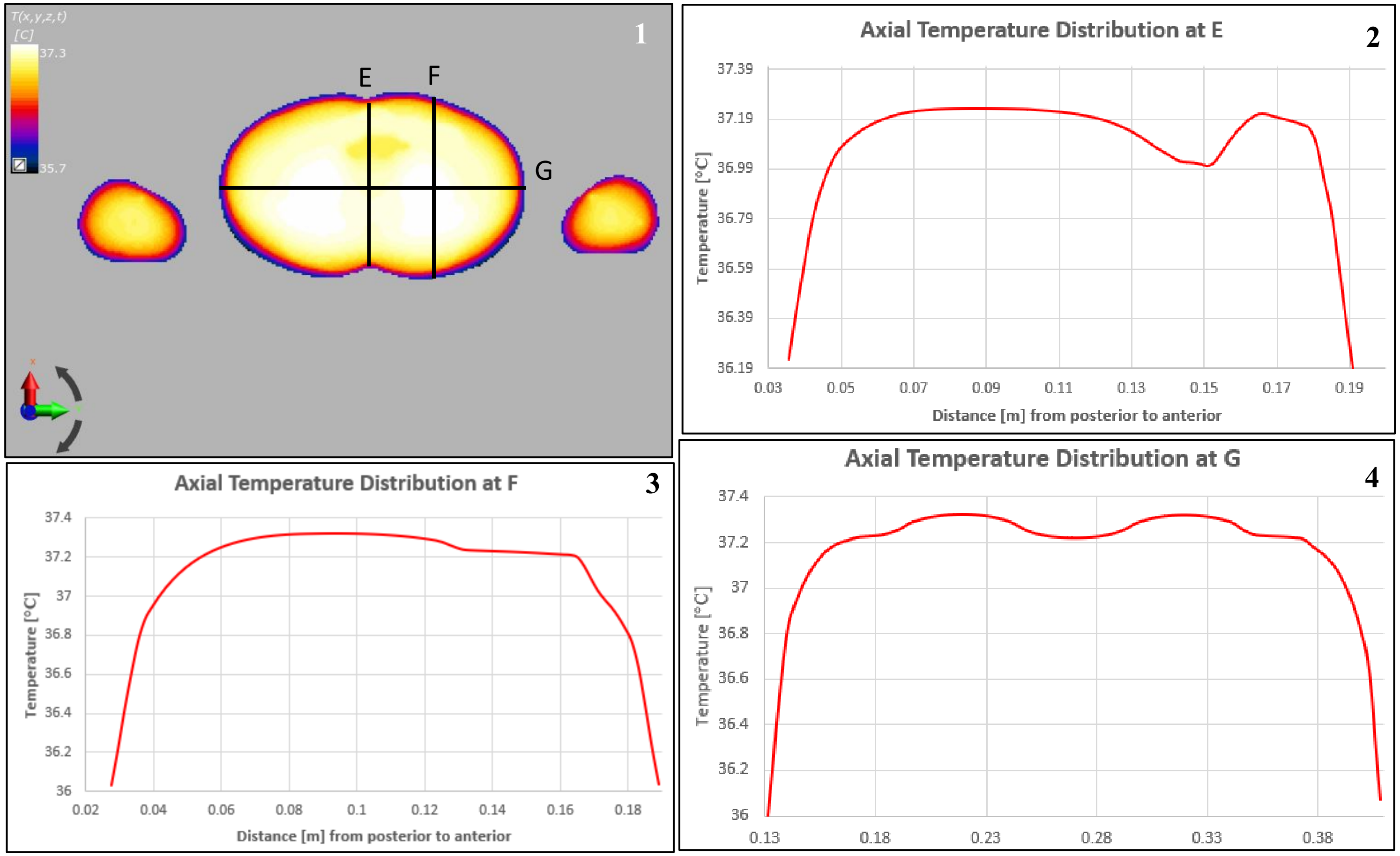

Fig. 6.9 – 1D antemortem axial temperature curves of Duke at the lower abdominal level. Fig. 6.9.1 indicates positions of 1D fields. Figs. 6.9.1 – 6.9.4 indicate 1D axial temperature curves from E, F and G, respectively. Note the depression in Fig. 6.9.2 caused by urine and the two peaks in Fig. 6.9.4 caused by the kidneys.

At the pelvis, the organ-domain that exhibited the highest temperature at the axial level of the rectosigmoid junction where the tip of a rectally inserted thermometer would halt (951.7mm from the floor) was **skeletal muscle** outside of the pelvic girdle, characterised by two symmetrical central isotherms. Therefore, the suggestion was that rectal temperature was not representative of deep core temperature, at least in the antemortem period. Fig. 6.10 indicates the axial temperature distribution at the pelvic level. As was found at the chest and abdomen, 1D axial temperature distribution differed according to the coronal (*yz*) and/or (para)sagittal (*xz*) plane selected for examination. Fig. 6.11 indicates 1D axial temperature curves of the pelvis plotted at various planes.

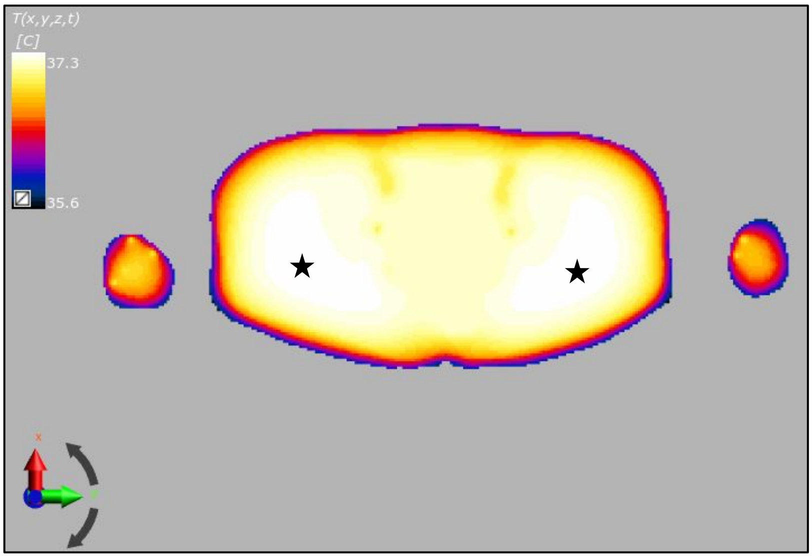

Fig. 6.10 The antemortem axial temperature distribution of Duke at the pelvis. Stars indicate position of skeletal muscle.

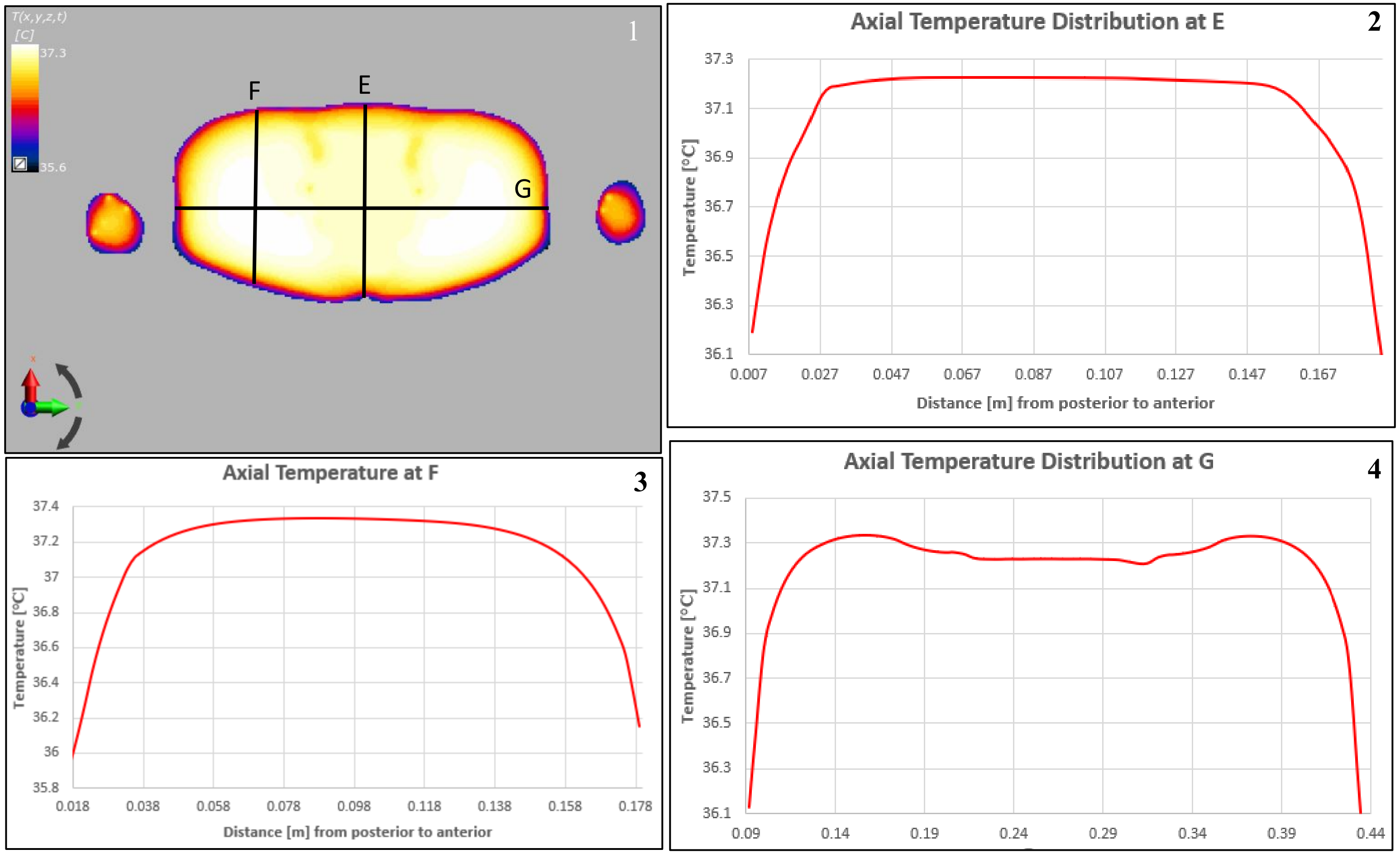

Fig. 6.11 – 1D antemortem axial temperature curves of Duke at the pelvis. Fig. 6.11.1 indicates positions of 1D fields. Figs. 6.11.2 – 6.11.4 indicate 1D axial temperature curve from E, F and G, respectively. Note the two peaks in Fig. 6.11D caused by extrapelvic muscles.

6.3 Conclusions

Several variables affect accuracy of death-time estimation methods, one of which is the axial temperature distribution at death. Literature review conducted in chapter 3 indicated that empiric methods of death-time estimation did not define total-body or axial temperature at death but used a single-point temperature approximation. It also indicated that numerical methods of death-time estimation applied varying bioheat modelling strategies on 3D computational phantoms of varying anatomical fidelity. This chapter proposes a numerical method of approximating antemortem total-body temperature distribution field at death using organ-specific metabolic heat generation and blood perfusion rates in a high-fidelity 3D computational phantom. Skin is the organ through which postmortem heat-transfer occurs to the external environment, therefore accurate estimation of its temperature at death cannot be overstated. In conclusion, this study:

4.4.1 Proposes numerical approximation of body temperature distribution at death using a high-fidelity 3D computational phantom and organ-specific heat generation and blood perfusion parameters.

4.4.2 Proposes separation of numerical approximation of body temperature distribution at death from numerical simulation of postmortem cooling.

4.4.3 Suggests that the antemortem central isotherm (hot core) is a nonhomogeneous field whose morphology varied according to the anatomical plane of examination.

Bibliography and References Cited

1. Hasgall PA, Di Gennaro F, Baumgartner C, Neufeld E, Lloyd B, Gosselin MC, Payne D, Klingenböck A, Kuster N. IT'IS Database of thermal and thermomagnetic parameters of biological tissue. Version 4.0 May 15, 2018. DOI: 10.13099/VOP21000-04-0. itis.swiss/database.

2. Jette M, Blümchen G (1990). Metabolic Equivalents (METS) in Exercise Testing, Exercise Prescription, and Evaluation of Functional Capacity. Clin. Cardiol. 13, 555-565.

3. de Dear R, Arens E, Zhang H, Hui Z, Oguro M. (1997). Convective and radiative heat transfer coefficients for individual human body segments. Int J Biometeorol, 141-156.

4. Fourmet D, Redortier B, Havenith G (2012). A method of whole-body skin temperature mapping in humans. Thermology International. 2(4), 157-159.

5. Tanda G (2018). Total body skin temperature of runners during treadmill exercise. J Therm Anal Calorim, 1967-1977.

6. Mall WEG (2005). Estimation of time since death by heat-flow Finite-Element model. Part I: method, model, calibration and validation. Legal Medicine, 1-14.

CHAPTER 7

Postmortem axial heat transfer

Chapter 7

Postmortem axial heat transfer

The previous chapter demonstrated numerical approximation of total-body temperature distribution in a high-definition, anatomically-segmented 3D computational phantom. This chapter examines numerical analysis of postmortem axial heat transfer in the human body using the same human phantom as a surrogate. The idea is that antemortem total-body temperature distribution, whose estimation was conducted in the previous chapter, would typically constitute initial conditions in simulation of postmortem axial heat transfer discussed in this chapter. An in-depth understanding of the behaviour of internal temperature fields during postmortem cooling would inform on the best anatomical site and method of thermometry while allowing accuracy and sensitivity of existing anatomical sites and method of thermometry used in death-time estimation. Ultimately, these steps lead to improvement in accuracy of death-time calculation methods.

As stated in chapter 1, Mfolozi[1] in 2013 hypothesized that the postmortem central isotherm (hot core) was a dynamic entity different to its antemortem counterpart. He speculated that its position responded to the temperature and thermophysical properties of a cooling surface on which the body rests by shifting either away or towards the cooling surface. If correct, such a shift would have material consequences to the value of a single-point core temperature measurement. That would obviously constitute a source of uncertainty in a death-time estimate. The bibliographic review in chapter 3 indicates that such an effect was not described in the literature. It was therefore mandatory to prove/disprove the hypothesis in this chapter.

7.1 Materials and Methods

The numerical analysis of postmortem cooling discussed in this chapter applied the same FDTD method, transient thermal analysis method, thermal analysis software, and computer hardware discussed in chapter 3. However, only the adult male 3D phantom Duke was selected for these analyses, to streamline the work. In this chapter, three postmortem cooling scenarios were simulated: 1) postmortem cooling in free-air, which constituted the baseline study, 2) postmortem cooling in the supine position on a simulated unheated concrete ground-surface, and 3) postmortem cooling in the supine position on a heated floor.

7.1.1 Simulation Setup – Postmortem Cooling in Free-air

7.1.1.1 **Simulation interval**

The simulated postmortem cooling interval was 5 hours (18000s) using a 1s time-step.

7.1.1.2 **Sensors**

Solutions were recorded every 3 minutes (180 seconds).

7.1.1.3 **Organ Parameters**

Biothermal parameters of all organ-domains were set to zero to simulate death.

Average/mean thermophysical parameters were applied to all organ-domains.

7.1.1.4 **Initial Conditions**

The antemortem body temperature approximated for the adult male 3D phantom Duke in chapter 6 constituted the initial condition.

7.1.1.5 **Boundary Conditions**

The ambient temperature selected for this analysis was 14°C, the boundary type was 'mixed' and the heat transfer coefficient[2] used was $3.4\text{Wm}^{-2}\text{K}$.

7.1.1.6 **Grid Design**

The grid settings were identical to those applied in chapter 6. The grid refinement applied was **normal.** The grid consisted of 3.4595×10^7 cells.

7.1.1.7 **Voxel Building**

The voxel settings were identical to those applied in chapter 6.

7.1.2 Simulation setup – Postmortem Cooling on Cold Concrete

7.1.2.1 **The cold concrete model-object**

A model-object 300mm x 600mm x 2000mm that represented a concrete block was built in the simulation software (Fig. 7.1). It had a slightly concave top surface from head to toe, a best-fit profile to the 3D computational phantom thought to have occurred during MRI scanning. Contact points with the 3D computational phantom's skin in the supine position were the occiput, shoulder blades, buttocks, the posterior surface of the thighs, hamstrings, and the posterior surface of the heels. The concrete block was assigned the following thermophysical properties:

- Density was for M50-grade concrete[3], 2400kg m^{-3}..
- Conductivity[4] was 0.8W $\mathrm{m}^{-1}\mathrm{K}^{-1}$.
- Specific heat capacity[5] was 960J $\mathrm{kg}^{-1}\mathrm{K}$.

7.1.2.2 **Simulation interval**

The simulated postmortem cooling interval was 5 hours (18000 seconds) using a time-step factor of 1s.

7.1.2.3 **Sensors**

Solutions were recorded every 3 minutes (180 seconds).

7.1.2.4 **Organ Parameters**

Biothermal parameters of all organ-domains were set to zero to simulate death.

Average/mean thermophysical parameters were applied to all organ-domains.

7.1.2.5 **Initial Conditions**

The initial temperature field of the adult male 3D phantom Duke was derived from the simulation undertaken in chapter 6. The initial temperature field of the concrete block was 14°C.

7.1.2.6 **Boundary Conditions**

The ambient temperature selected for this analysis was 14°C, the boundary type was ‘mixed’ and the heat transfer coefficient[6] used was $3.4\mathrm{Wm}^{-2}\mathrm{K}$.

7.1.2.7 **Grid Design**

The grid settings were identical to those applied in chapter 6. The grid refinement applied was **normal.** The grid consisted of 5.9374×10^{7} cells.

7.1.2.8 **Voxel Building**

The voxel settings were identical to those applied in chapter 6.

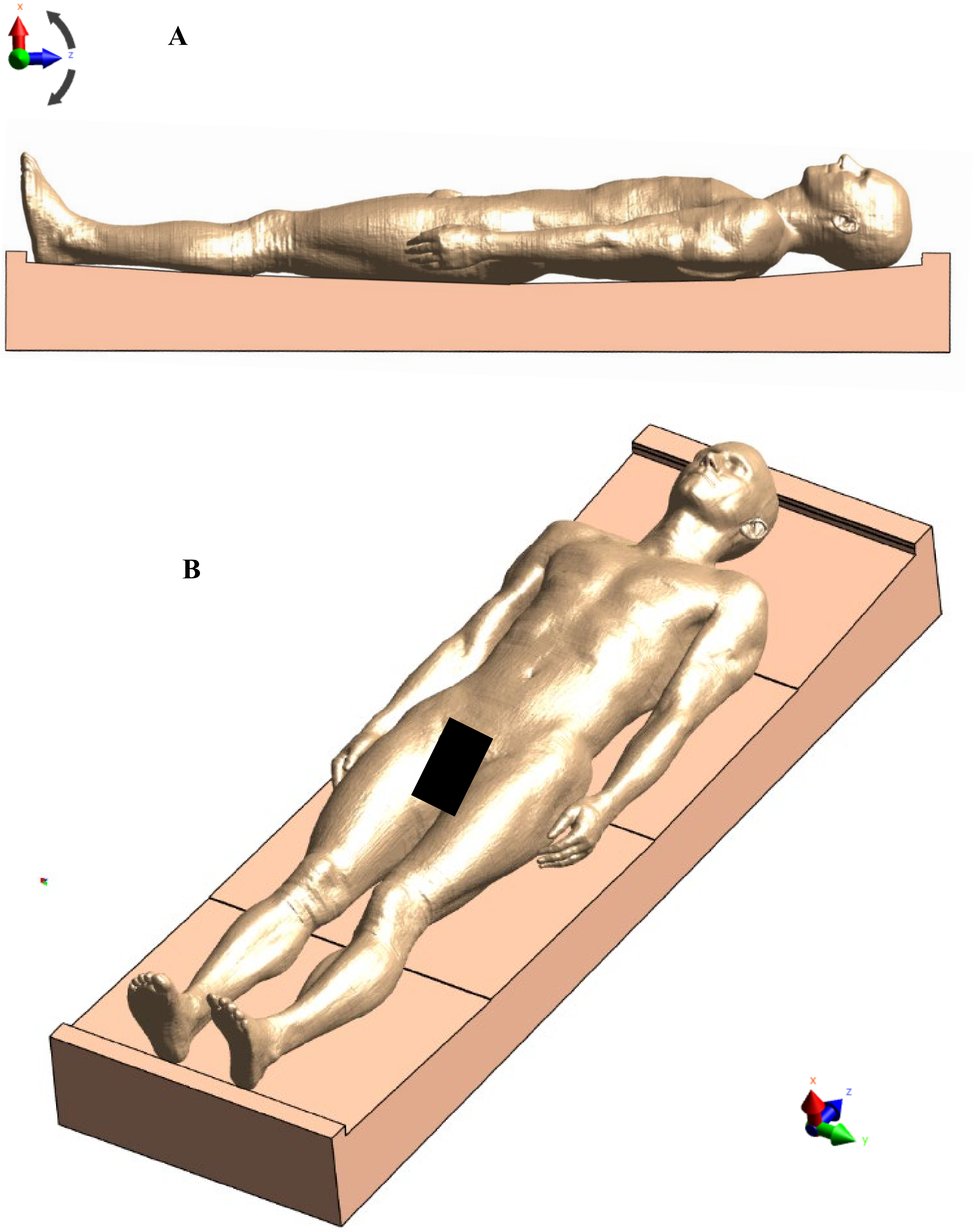

Fig. 7.1 – The concrete surface on which Duke was placed. **A** is lateral view and **B** is oblique view.

7.1.3 Simulation Setup – Postmortem Cooling on Heated Floor

7.1.3.1 **The heated floor model-object**

A 20mm x 2000mm x 600mm model-object that represented a heated floor was built in the simulation environment and placed on top of the concrete surface mentioned earlier as illustrated in Fig.7.2. The 3D human computational phantom was placed supine on the heated surface. Skin contact points against the heated surface were identical to those on concrete mentioned in the previous subsection. The heated floor was assigned a Neumann boundary condition to enable it to be a heat source. Being a boundary-condition, the heated floor was therefore not assigned material properties but was assigned a heat-flux value whose mathematical sign indicated whether it was a heat source (+ sign) or a heat sink (– sign). The assigned heat-flux value was +40 Wm^{-2}.

7.1.3.2 **The cold concrete model-object**

The concrete surface beneath the heated surface was assigned the same thermophysical values mentioned earlier.

7.1.3.3 **Simulation interval**

The simulated postmortem cooling interval was 5 hours (18000 seconds) using a time-step factor of 1s.

7.1.3.3 **Sensors**

Solutions were recorded every 3 minutes (180 seconds).

7.1.3.4 **Organ Parameters**

Biothermal parameters of all organ-domains were set to zero to simulate death.

Average/mean thermophysical parameters were applied to all organ-domains.

7.1.3.5 **Initial Conditions**

The initial temperature field of the adult male 3D phantom Duke was derived from the simulation undertaken in chapter 6. The initial temperature field of the heated floor was 25°C. The initial temperature field of the concrete block was 14°C.

7.1.3.6 **Boundary Conditions**

The ambient temperature selected for this analysis was 14°C, the boundary type was 'mixed' and the heat transfer coefficient[7] used was $3.4\text{Wm}^{-2}\text{K}$.

7.1.3.7 **Grid Design**

The grid settings were identical to those applied in chapter 6. The grid refinement applied was **normal.** The grid consisted of 6.2278×10^7 cells.

7.1.3.8 **Voxel Building**

The voxel settings were identical to those applied in chapter 6.

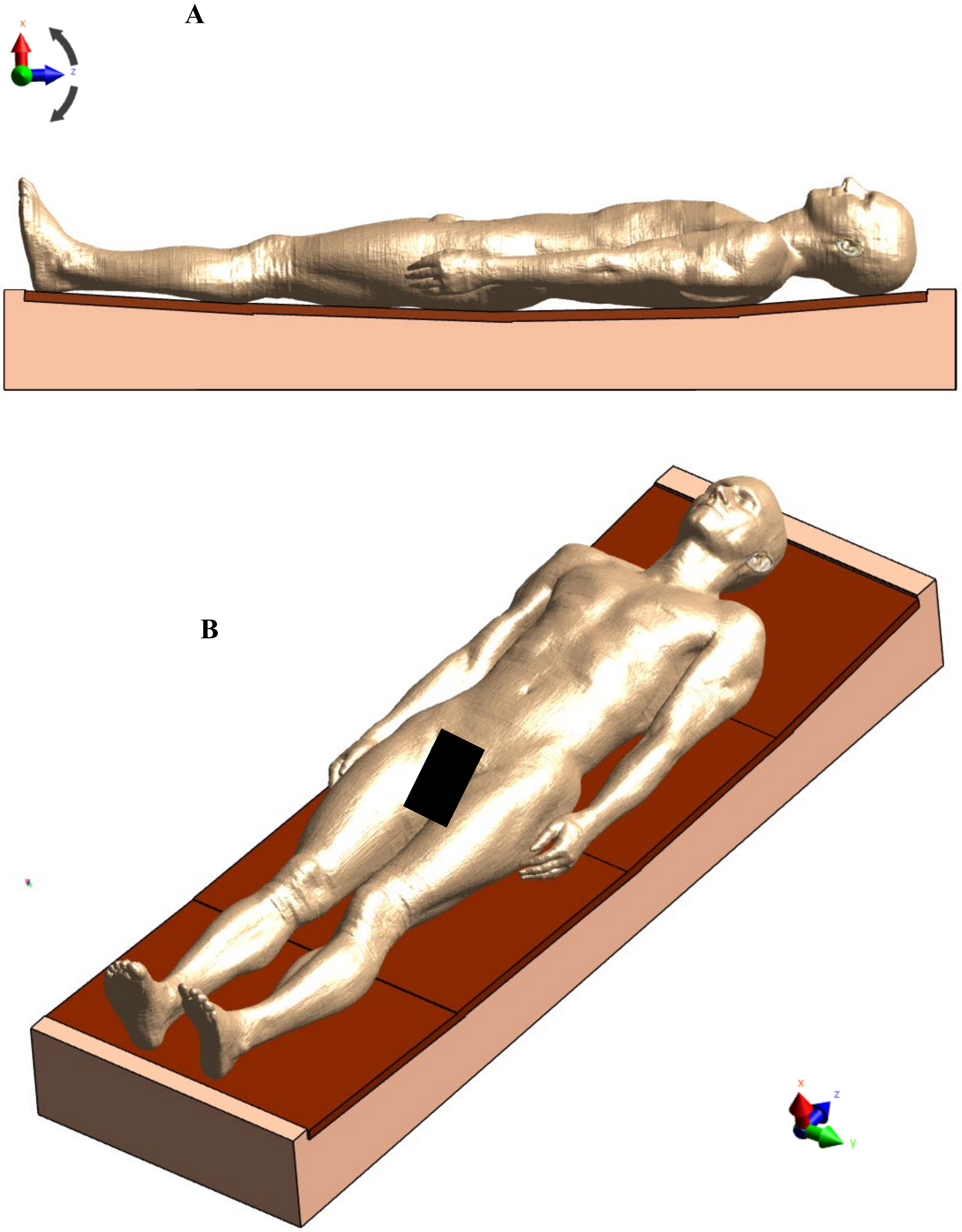

[redacted]

Fig. 7.2 The heated floor (red-brown) between the concrete surface (beige) and Duke. **A** indicates the lateral view and **B** indicates the oblique view.

7.2 Results

Because death-time estimation applies temperature measurements obtained from the body, the results sections in the rest of this thesis are from the perspective of simulated temperature fields and not necessarily mathematical analyses of heat transfer processes causing temperature fields.

7.2.1 Free-air Postmortem Cooling

Predicted skin temperature during postmortem cooling in free-air, which was inhomogeneous at the beginning of cooling, remained inhomogeneous for the chosen duration of postmortem cooling. This observation strengthened the assertion of the significance of realistic prediction of skin temperature at death. Skin areas starting off with lower initial temperature remained cool, while other skin areas warmed slightly for a while before eventually cooling again. Skin areas with relatively high initial temperatures eventually cooled, as expected. Fig. 7.3 indicates the predicted skin temperature 5 hours after death (compare with Fig. 5.4).

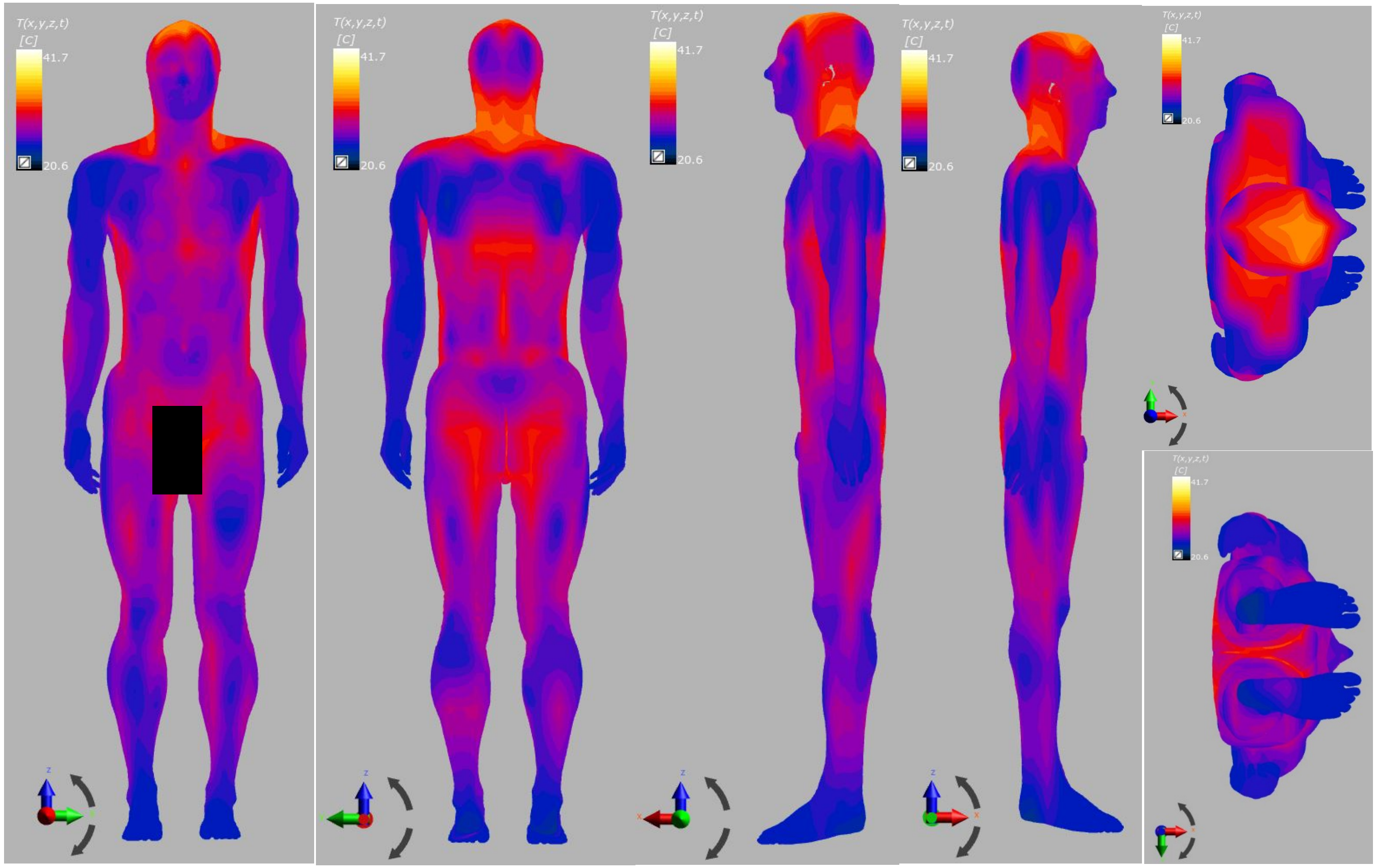

Fig. 7.3 – Predicted skin temperature of the adult male geometry 18000s after death in free-air cooling. From left to right are views: anterior, posterior, left lateral, right lateral, top (far-right top) and bottom (far-right bottom).

The axial section selected to illustrate postmortem heat transfer was at the abdomen at the level of the liver, 1241mm above the heel. Video 7.1 that accompanies this thesis in a USB disc demonstrates the evolution of axial thermal fields in free-air cooling over the 5 hours. One second of playback-time represents 300s of simulated cooling. Fig. 7.4 demonstrates nine screengrab images from Video 7.1 at selected PMIs. The temperature of skin or 'outer shell' at death was 36.5°C while that of the 'inner core' was 37.4°C. Then, the following observations were made:

- At ±180s after death, an isotherm of 36.5°C previously confined to the skin slightly thickened in its inner surface and pushed the central isotherm of 37.4°C, causing the latter to shrink slightly.
- At ±360s after death, a new isotherm of 36.3°C had developed on the outer surface of the skin. It surrounded and moved the 36.5°C isotherm inward, which at this stage had become circular. In turn, the isotherm of 36.3°C further pushed the central isotherm of 37.4°C, causing it to shrink further.
- At ±2340s after death, another isotherm of ~36.1°C had developed on the outer surface of the skin. It too surrounded and moved the 36.3°C isotherm inward, which in turn shifted the 36.5°C isotherm inward, which in turn moved towards the central antemortem isotherm and caused it to shrink even further.
- This cycle was repeated every few hundred seconds or so, in which new cooler circular axial isotherms developed on the skin, while pre-existing ones propagated inwards towards the core, gradually reducing in diameter along with the central isotherm.

- At 13860s (3hrs 51mins) after death, the 37.4°C antemortem central isotherm that had progressively been shrinking finally disappeared. Thereafter, the 36.5°C isotherm that had immediately surrounded it became the first ‘postmortem’ central isotherm. It had a substantial initial radius and it too persisted for many minutes as it gradually shrunk to well beyond the 5-hour limit of the simulation.
- In the abdomen, all newly-formed axial isotherms on skin initially assumed the exact circumferential contour of the skin. But as they shrunk and propagated towards the core, they gradually became ovoid and were perfectly oval by the time they each became the central isotherms. Axial sections in all other parts of the body including the thighs (not shown in this thesis) also displayed propagating circular axial isotherms and shrinking central isotherms. In the arms, the antemortem central isotherm lasted 1620s (27 minutes) on the left and 1980s (33 minutes) on the right.

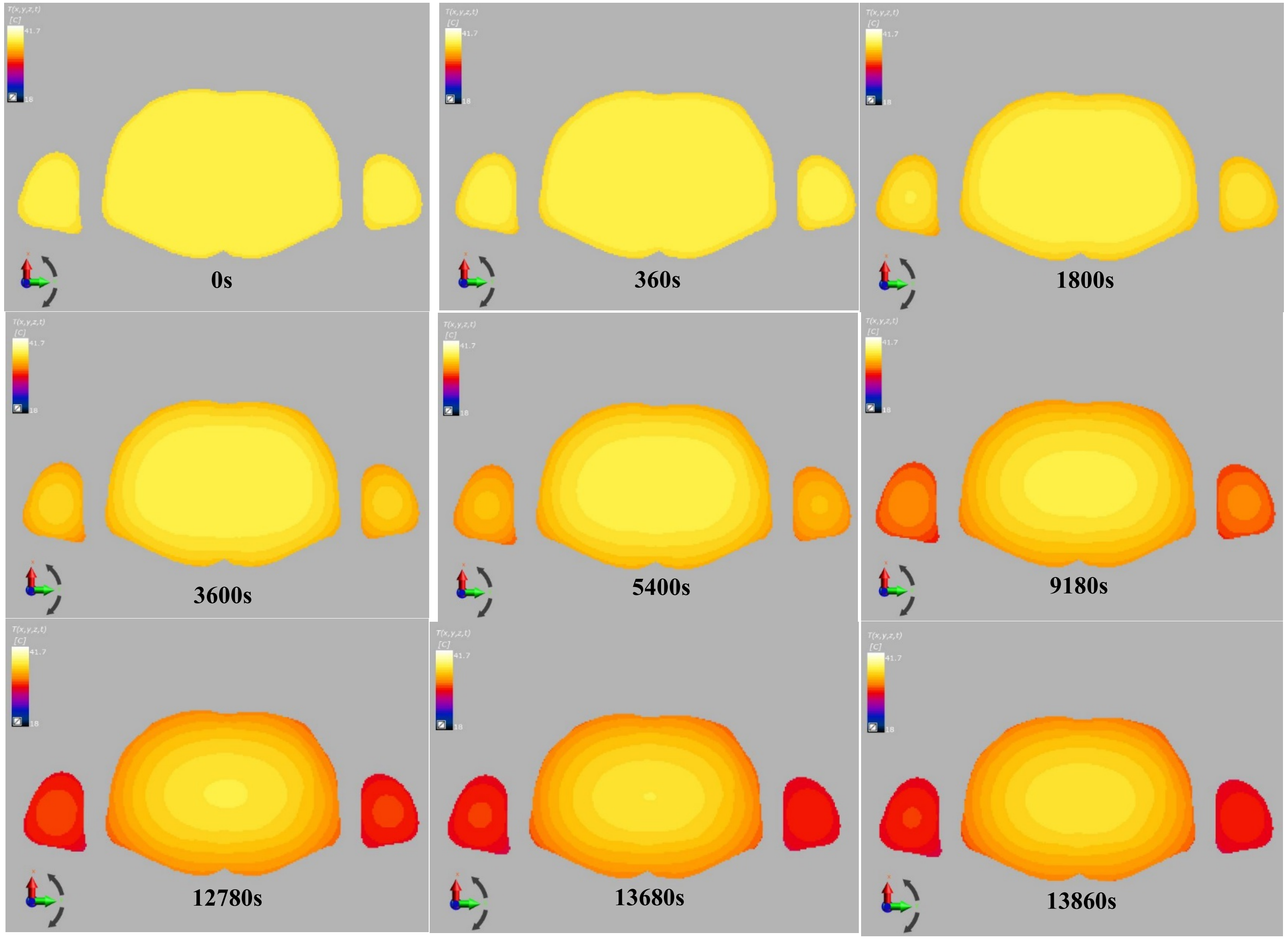

Fig. 7.4 – Axial isotherms during free-air postmortem cooling. Note specificity of each isotherm profile to the PMI. The central antemortem isotherm lasted from 0s to 13680s. Note the rapid cooling of the arms due to their smaller radius than the trunk.

7.2.2 Postmortem Cooling on Cold Concrete

The supine position of the 3D phantom on cold concrete resulted in skin contact-points through which heat transfer occurred by thermal conduction. The occiput showed a round contact-point, the posterior surface of the upper chest and shoulders showed a large V-shaped contact-point, and the buttocks, posterior thighs, calves, and heels all showed oval contact-points. All contact-points corresponded to surfaces normally observed having contact pallor on supine bodies at the mortuary, which were a small fraction of the total skin surface. The skin temperature on the posterior aspect of the body changed dynamically. Contact points showed persistently lower temperatures than the rest of skin during the entire simulation interval, indicating accelerated heat transfer by thermal conduction there than by thermal convection elsewhere on the skin. The rate of cooling of skin on the anterior surface of the body was slow.

Skin at the chosen axial level was in contact with concrete. Simulated postmortem cooling at the chosen axial levels showed similarities that of free-air cooling. Video 7.2 (accompanying this thesis in a USB disc) demonstrates the evolution of thermal fields in postmortem cooling on concrete over the 5 hours. One second of playback-time represents 300s of cooling. Noteworthy differences were:

- ➢ Increased rate of heat loss by thermal conduction at contact points with cold concrete floor caused a large temperature gradient between the central isotherm and concrete compared to other parts along the body circumference at an axial level. The result was an apparent shift of the central isotherm away from concrete towards the anterior surface of the body. Fig. 7.5 demonstrates nine screengrab images from Video 7.2 at selected PMIs. This shift was the cause of the relatively sluggish rate of cooling of the skin observed on the anterior aspect of the body.

- The antemortem central isotherm existed for a comparatively shorter period in simulated postmortem cooling on the cold concrete (about 9000s or 2hrs 30mins) compared to air. This was because the antemortem central isotherm radius was smaller at death due to the larger temperature gradient between itself and the concrete floor.
- Overall, heat transfer to cold concrete was accelerated compare to free air because of concrete’s material properties and temperature.

The simulation indicated that internal temperature of the concrete block evolved throughout the simulation interval. Heat transfer from the body to the concrete block caused semi-circular axial isotherms inside the concrete block that propagated radially away from contact-points into the bulk of the block, causing a gradual rise in its temperature.

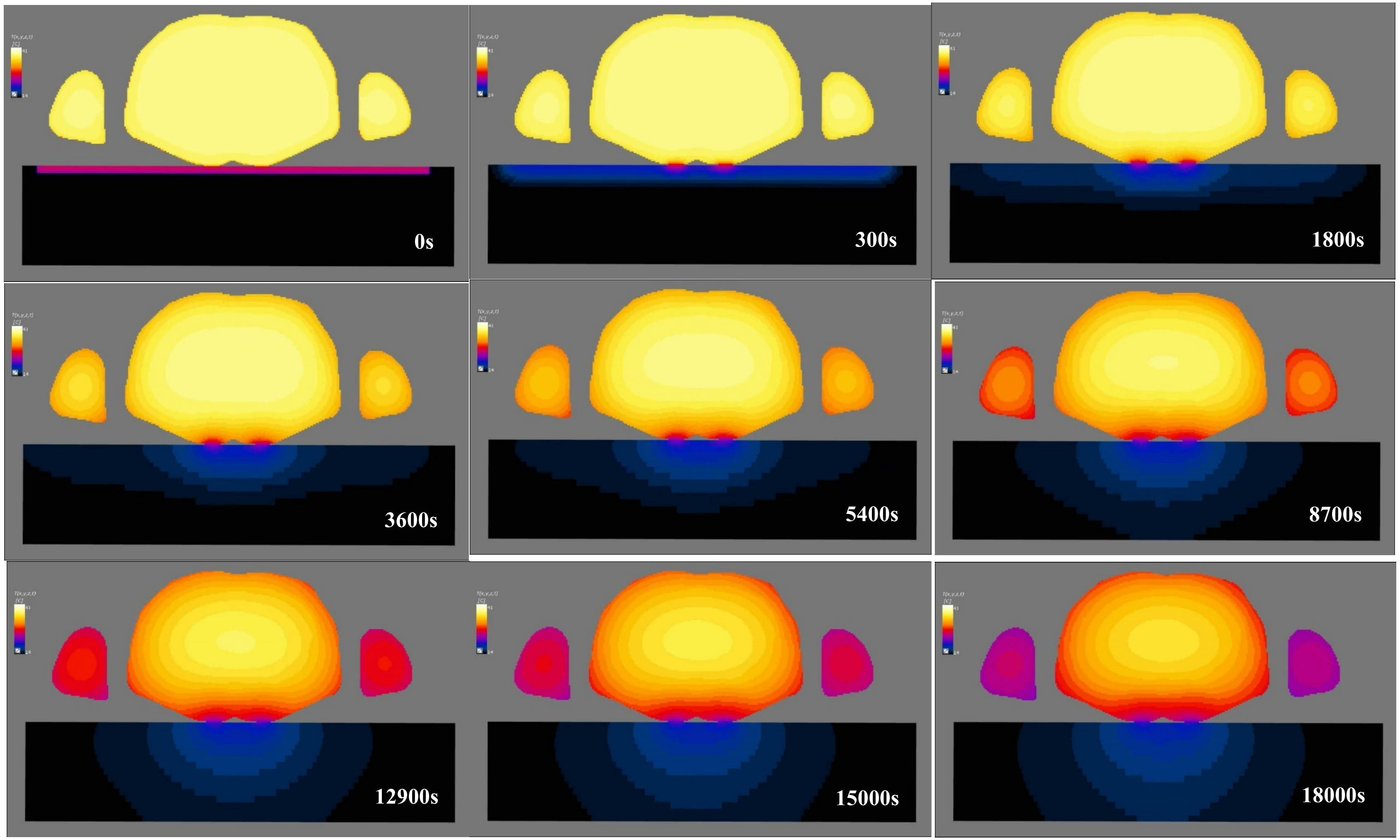

Fig. 7.5 – Circular isotherms and central isotherms during postmortem cooling on concrete (black rectangle). Note the persistently lower skin temperature at contact points, dense circular isotherms deep to contact points, anteriorly-shifted central isotherms and semi-circular isotherms inside the concrete block (blue).

7.2.3 Postmortem Cooling on Heated Floor

Skin on the anterior aspect of the body had a narrow temperature distribution of 25°C at the beginning of cooling, which remained relatively constant throughout the simulated PMI. Distal aspects of limbs closer to the torso showed progressive cooling. Contact-skin at the shoulders and buttocks showed a constant temperature of 28°C throughout the simulated PMI, while surrounding non-contact skin progressively cooled. Temperature evolution at the chosen axial section was more complex. At death, the central isotherm was located posteriorly and closest to the heated surface, causing the lowest temperatures to be on the skin of the anterior aspect of the body. See Fig. 7.6. The temperature gradient between the central isotherm and anterior skin was 12.5°C, more than any observed over such a short axial distance. On commencement of cooling, that temperature gradient expanded into multiple distinct isotherms, the inner-most of which propagated towards the central isotherm, resulting in its shrinkage as expected. The outer-most isotherms showed paradoxical retrograde propagation towards the skin for a short period. Intermediate circular axial isotherms stagnated for a prolonged period, which explained the constant temperature of 25°C observed on the anterior surface of the body for the 5-hour duration of simulated postmortem cooling. The antemortem central isotherm lasted 5400s (1 hour 30 minutes). This is significantly shorter than that seen in free air cooling and cooling on concrete discussed earlier. Its posterior location reduced the distance travelled by the first circular isotherm from the posterior skin to the core. Video 7.3 (accompanying this thesis in a USB disc) demonstrates the evolution of thermal fields in postmortem cooling on a heated surface over the 5 hours. One second of playback-time represents 300s of cooling.

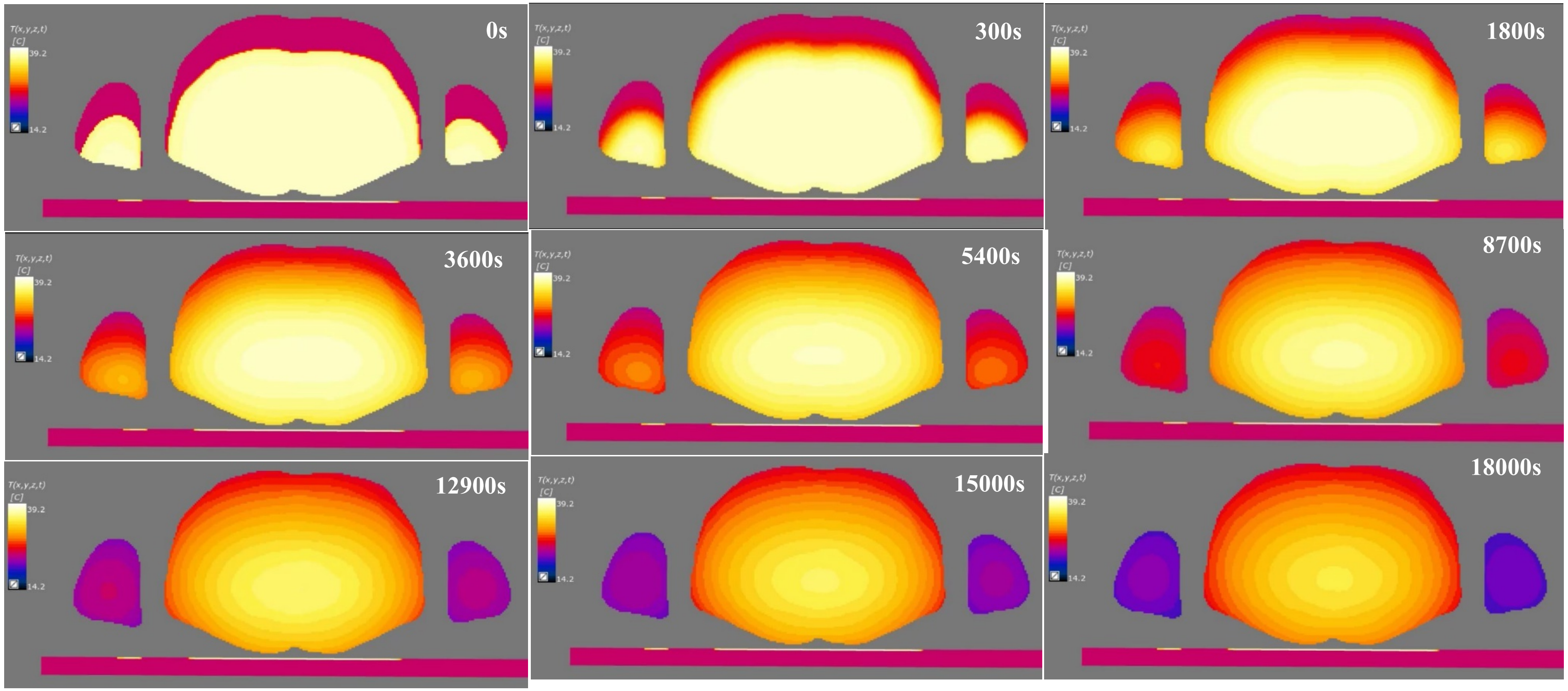

Fig. 7.6. – Circular isotherms and central isotherms during postmortem cooling on a heated surface (magenta rectangle) at abdomen. Note lower skin temperature towards the anterior, dense isotherms deep to anterior skin, and posteriorly-shifted central isotherms.

7.3 Discussion

7.3.1 Free-air Postmortem Cooling

Although the author understood that the direction of heat transfer was from the deep core to the skin, visualisation of axial isotherms provided a unique perspective of postmortem heat transfer. Isotherms (and not heat transfer or heat flux per se) are what thermometers measure from a body during postmortem thermometry for death-time estimation. It was therefore more important for purposes of this thesis to understand isotherms to help explain experimental observations described by authors in the field. The optimal temperature scale that visualised postmortem isotherms during post-processing was from 14°C to 40°C.

From Video 7.1 it became evident to the author that:

a) The antemortem central isotherm was in fact the elusive PMTP. Similar internal isotherms in human surrogates appear in studies by Kanawaku et al[8] and Schenkl et al[9], although no mention of their propagation or relationship to the PMTP was made,

b) The periphery of the antemortem central isotherm was the entity hypothesised by Mfolozi in 2013 to propagate from the skin to the centre of the body, resulting in cooling of successive body layers as it travelled.

c) A thermometer placed in the centre of the antemortem central isotherm in this 3D computational phantom would measure 37.4°C for an uninterrupted 3hrs 51mins after death before registering any temperature change there – the definition of a PMTP. This observation highlighted the inherent inability for single-point core thermometry to differentiate a 37.4°C core-body temperature measured at death from a 37.4°C core-body temperature measured 3hrs 51mins after death in a body found dead. This was thought to be one of the reasons empiric death-time estimation methods that employ single-point core thermometry express their PMI estimate as a range rather than a single value. For example, application of the Rectal Temperature Nomogram method to estimate the PMI in this scenario using 37.4°C as the measured body temperature predicted a PMI of 2hr 20min ± 2hr 48min (i.e. 0hrs to 5hrs 8min) using a corrective factor of 1.

d) A thermometer placed at the beginning of postmortem cooling between the skin and the centre of the antemortem central isotherm would measure a PMTP shorter than the full 3hrs 51minutes.

e) A temperature gradient always existed between the skin and the centre of the body at all indicated PMIs.

f) The temperature value measured by single-point thermometry at a given PMI would depend on thermometry-depth used. A higher temperature would be recorded by a deeply inserted thermometer, and vice versa. This effect of thermometry-depth, also referred to as the '*location factor*' or radius by Joseph and Schickele[10] is a recognised source of uncertainty in death-time estimation and was hypothesised by Mfolozi in 2013.

g) A thermometer placed for the first time at the centre of the antemortem central isotherm (PMTP) some time after postmortem cooling commences, for example at a PMI of 5400s (1hr 30 mins), would register the remainder of the antemortem central isotherm's life/PMTP. In other words, the measured PMTP would only be 8460s (2hr 21mins) long. This, once more, proved Mfolozi's hypothesis that the time between death and thermometry (which, in the case of a dead body for which death-time estimation is performed, is the PMI of that body by definition) was a variable that affected the PMTP length independent of the other variables already discussed.

h) The antemortem central isotherm, and therefore the PMTP, existed for longer in the abdomen than in the arms because the radius – the axial distance travelled by the antemortem central isotherm as it shrunk – was more in the abdomen than in the arms, while the rate of shrinking was the same in both. This corresponded to the effect of the *size-factor* as discussed by several authors[11,12] and once more proved Mfolozi's 2013 hypothesis that body radius (circumference) was an independent variable affecting the PMTP length.

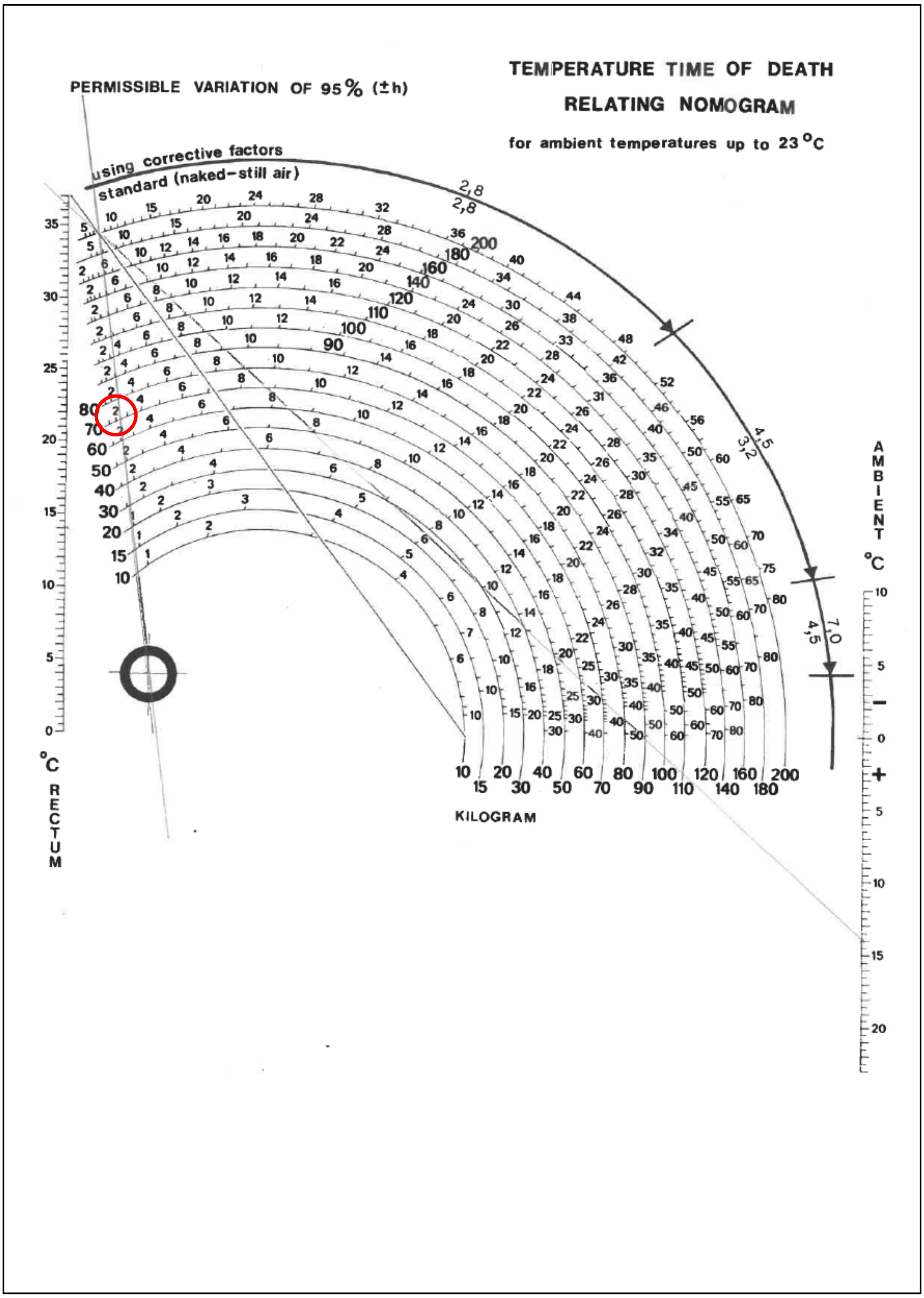

Fig. 7.7 – The Rectal Temperature Nomogram method used to estimate Duke’s PMI using a core temperature of 37.4°C. Air temperature was 14°C and body mass was 70kg. The red circle indicates the PMI estimate.

The fact that metabolic-heat generation rates of all organs were set to zero in numerical simulations in this chapter indicated that no postmortem metabolism or any other biological phenomena, as suggested by several erstwhile authors discussed in chapter 3, was required to produce the PMTP. Unlike Mall's heat-flow FEM[13,14], zeroing of metabolic-heat generation rates in this study was performed simultaneously and abruptly in all organs without using a decrease-rate of internal power to artificially induce the PMTP.

Varying combinations of the above factors in erstwhile postmortem cooling experiments were thought to be responsible for the unpredictable nature of the PMTP. This study also demonstrated that 'postmortem' central isotherms formed after the disappearance of the antemortem central isotherm also existed for nearly as long as the antemortem counterpart, accounting for the sluggish rate of core cooling measured after the PMTP that some authors incorporated into the PMTP definition. The temperature of central isotherms (antemortem and postmortem) measured by single-point thermometry and applied in today's methods of death-time estimation is therefore not specific to identify the amount of time lapsed after death that results in that isotherm temperature.

7.3.2 Postmortem Cooling on Cold Concrete

This study demonstrated that temperature and thermophysical properties of a cold ground-surface such as concrete affected postmortem cooling by shifting the location of the postmortem central isotherm, consistent with the author's 2013 hypothesis. The shift was not drastic but was nonetheless noticeable and would have obviously affected the value of a measured single-point core temperature and subsequent death-time estimation calculation by empiric methods. Central isotherms shifted away from the cold concrete ground-surface because the latter was cooler than the body. Their shift towards the anterior of the body was due to the body's supine position on the ground. The final position of the central isotherm in a given body found dead would thus be determined by that temperature and material properties of a ground-surface as well as the position of the body, i.e. supine, lateral, or prone.

This study also demonstrated that a cold ground-surface such as concrete may not always be an infinite heat-sink as assumed in the heat-flow FEM by Mall[13,14]. This was because the temperature of concrete continually increased as a result of heat transfer to it, which independently resulted in progressive slowing of subsequent heat transfer rates. The rate of heat transfer to concrete by thermal conduction was demonstratively higher than the rate of heat transfer to air by thermal convection and thermal radiation, despite air and concrete having identical initial temperatures of 14°C during the simulated cooling interval. The shift of the central isotherm caused by thermophysical properties of the ground-surface was an additional variable responsible for the unpredictability of the PMTP, was a function of single-point thermometry.

7.3.3 Postmortem Cooling on Heated Floor

Postmortem cooling on a heated floor produced several unexpected observations:

a) Firstly, the antemortem central isotherm existed for a shorter duration compared to postmortem cooling in free air. The PMTP during postmortem cooling on heated floor was thus shorter, whereas the author's expectation had been that it would be longer because less heat transfer had been expected to occur to the heated floor because it was already heated.
b) Secondly, the temperature of the heated floor increased at contact points in the early stages of postmortem cooling, indicating that heat transfer by thermal conduction occurred from the body to the floor despite the floor being heated. The area of the heated floor on which the temperature increase occurred assumed a silhouette of the body whose temperature was higher than its original temperature of 25°C as indicated in Fig. 7.8. This observation was thought to occur because the original 25°C of the heated floor was lower than the original body core temperature of 37.4°C at death. That difference created a temperature gradient towards the heated floor, which heat transfer then followed. Heat transfer to the heated floor would cease once the body, air and heated floor temperatures equilibrated.

One postmortem cooling condition in which use of the Rectal Temperature Nomogram method is not advised is presence of strong thermal radiation, which a heated floor is an example of. This study succeeded in numerically demonstrating heat transfer from the body to a heated ground-surface during postmortem cooling.

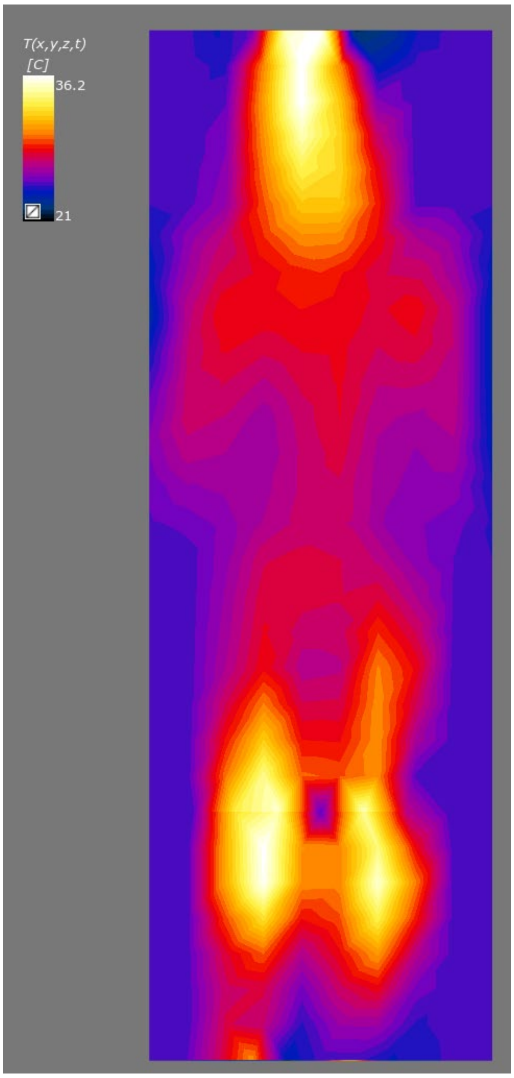

Fig. 7.8 – The effect of heat transfer from the phantom (not shown) on the heated floor.

7.3.4 Shifted Postmortem Central Isotherm

The shifting phenomenon of the central isotherm caused by thermophysical properties and temperature of ground-surfaces is illustrated in Fig. 7.9 using side-by-side comparison of axial views of the three cooling scenarios at comparable PMI's.

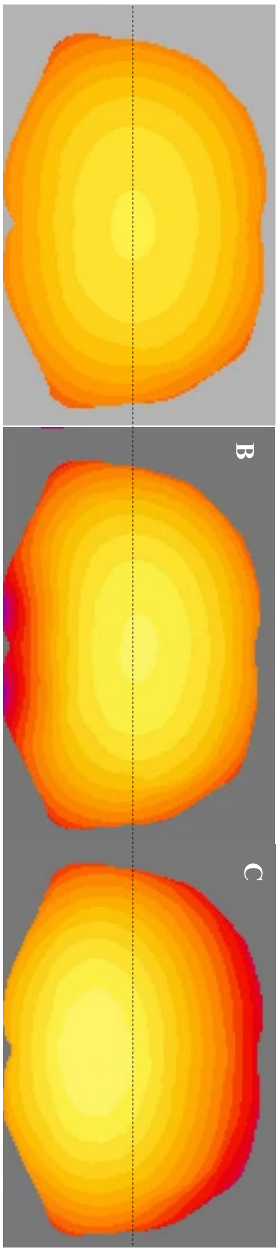

Fig. 7.9 – Side-by-side comparison of shifted central isotherms at comparable PMI. Figs.7.9A-C indicate cooling in free-air at 12780s, cooling on concrete at 12900s and cooling on heated floor at 12900s, respectively. The dotted line passes through the centre of the central postmortem isotherm in free-air cooling.

7.3.5 The PMTP phenomenon

The single most important lesson learnt from this thesis was that the PMTP phenomenon was a manifestation of a much more fundamental problem at the centre of uncertainty in thermometric death-time estimation. This root problem is the standard practice of measuring postmortem core temperature from a single point within the body core, already referred to in this thesis as ‘single-point core thermometry’. It is application of single-point thermometry that results in:

a) Misrepresentation of antemortem temperature distribution as a single-point rectal temperature of 37°C,
b) Detection of the PMTP,
c) Variations of measured temperatures among different bodies if relative thermometry-depth is not standardised, and
d) Variations of temperature measurements among different bodies if thermophysical properties and temperature of ground-surfaces are not accounted for.

7.4 Conclusions

Contributions made by this study to death-time estimation therefore are that:

7.4.1 The standard single-point core thermometry technique used in death-time estimation measures only the temperature of a central isotherm, which this study demonstrated to be nonspecific to a single PMI value.

7.4.2 The postmortem axial thermal profile in the human body continuously changed from the TOD until the end of postmortem cooling, i.e. it has high specificity for any given PMI value, which would be useful for death-time estimation.

7.4.3 Multipoint axial thermometry (MAT) if applied in death-time estimation, could eliminate single-point uncertainties as discussed in this thesis that cause:

    7.4.3.1 the PMTP phenomenon,

    7.4.3.2 variations of core temperature measurements due to non-standardization of thermometry-depth,

    7.4.3.3 variations of core temperature measurements due to shifted central isotherms as a result of temperature and thermophysical properties of ground-surfaces and of variations in body position.

7.4.4 By extension:

    7.4.4.1 Modelling ground-surfaces in numerical analyses of postmortem cooling is advisable to account for its effects in shifting the central isotherm, 7.4.4.2 effort must be made to establish the ground-surface temperature at the death scene, and this must be modelled in numerical analyses as well,

7.4.4.3 effort must be made to establish thermophysical properties of ground-surfaces and these must be modelled, and

7.4.4.4 body position must be established at the death scene, and this must be modelled representatively to accurately represent central isotherm shifting.

Bibliography and References Cited

1. Mfolozi S (2013). Cooling rates of dummies under various degrees of air humidity, wind speed and air temperature. Masters dissertation. University of Cape Town.

2. de Dear R, Arens E, Zhang H, & et al. (1997). Convective and radiative heat transfer coefficients for individual human body segments. Int. J. Biometeorol.141-156.

3. Kitouni S, Houari H (2013). Lightweight concrete with Algerian limestone dust. Part I: Study on 30% replacement to normal aggregate at early age. Cerâmica 600-608.

4. Young HD (1992). University Physics, 7th Ed., Addison Wesley Publication Company, Reading, Massechusetts.

5. Engineering ToolBox (2003). *Specific Heat of Solids*. https://www.engineeringtoolbox.com/specific-heat-solids-d_154.html.

6. de Dear R, Arens E, Zhang H, & et al. (1997). Convective and radiative heat transfer coefficients for individual human body segments. Int. J. Biometeorol.141-156.

7. de Dear R, Arens E, Zhang H, & et al. (1997). Convective and radiative heat transfer coefficients for individual human body segments. Int. J. Biometeorol.141-156.

---

8. Kanawaku Y, Kanetake J, Komiya A, Maruyama S, Funayama M (2007) Computer simulation for postmortem cooling processes in the outer ear. Legal Medicine, 55-62.

9. Schenkl S, Muggenthaler H, Hubig M, Erdmann B, Weiser M, Zachow S, Heinrich A, Güttler FV, Teichgräber U, Mall G (2017). Automatic CT-based finite element model generation for temperature-based death time estimation: feasibility study and sensitivity analysis. International Journal of Legal Medicine, 699-712.

10. Joseph A, Schickele A (1970). A general method of assessing factors controlling postmortem cooling. Journal of Forensic Sciences, 364 – 391.

11. de Saram GSW, Webster G, Kathirgamatamby N (1955). Postmortem temperature and the time of death, J. Crim. Law Criminol. 562-577.

12. Brown A, Marshall T (1974). Body temperature as a means of estimating time of death. Forensic Science International, 125-133.

13. Mall G, Eisenmenger W (2005). Estimation of time since death by heat-flow Finite-element model part I: method, model, calibration and validation. Legal Medicine, 1-14.

14. Mall G, Eisenmenger W (2005). Estimation of time since death by heat-flow Finite-element model part II: application to non-standard cooling conditions and preliminary results in practical casework. Legal Medicine, 69-80.

CHAPTER 8

Multipoint axial thermometry

Chapter 8

Multipoint axial thermometry

Chapter 7 of this thesis demonstrated that the standard single-point core thermometry technique applied in empiric and numerical death-time estimation methods today measures only the temperature of the central isotherm, which has very low specificity for any given PMI value. The axial thermal profile of the human body, on the other hand, was demonstrated to be very specific for any given PMI value under a specific set of circumstances. The suggestion was that MAT could be used for death-time estimation and would eliminate those single-point core thermometry uncertainties discussed previously in this thesis. This chapter demonstrates MAT using a proposed custom-made MAT device. MAT was undertaken in empiric and numerical studies of postmortem cooling under natural convection conditions.

8.1 Materials for Empiric Multipoint Axial Thermometry

8.1.1 A multipoint thermometry device

After it became clear that the axial thermal profile of a body showed high specificity for a given PMI compared to single-point thermometry, the author designed and commissioned fabrication of a MAT device prototype. Fig. 8.1 depicts the prototype in different formats during its development. The device was regarded as a practical output of this thesis. As shown, it was T-shaped and consisted of a handle part and a long shaft part. The shaft part consisted of a 350mm-long clear Perspex tube of 5mm inner radius and 6mm outer radius. The tube housed a 1.6mm high, 8.5mm wide and 350mm long printed circuit-board on which 64 square-shaped MAX30205 human body temperature sensor-chips[1], each 3mm x 3mm x 1mm, were located. The temperature sensor chips were spaced 5mm apart and had a resolution of 0,0001°C. The printed circuit-board was fixed onto a 325mm-long, 5mm radius, semi-circular grade-316 stainless-steel cylinder to provide mechanical strength during insertion into the body. A 35mm-long arrow-shaped introducer with a conical head, also fashioned out of grade-316 stainless-steel, was fitted into the open end of the Perspex tube to protect the printed circuit-board and temperature sensors from moisture damage and to facilitate skin perforation and insertion into the body. Two rubber gaskets having a 4mm inner radius and a 5mm outer radius were fitted in two grooves on the introducer against the Perspex tube for waterproofing. The distance from the tip of the introducer to sensor-chip #1 was 43mm.

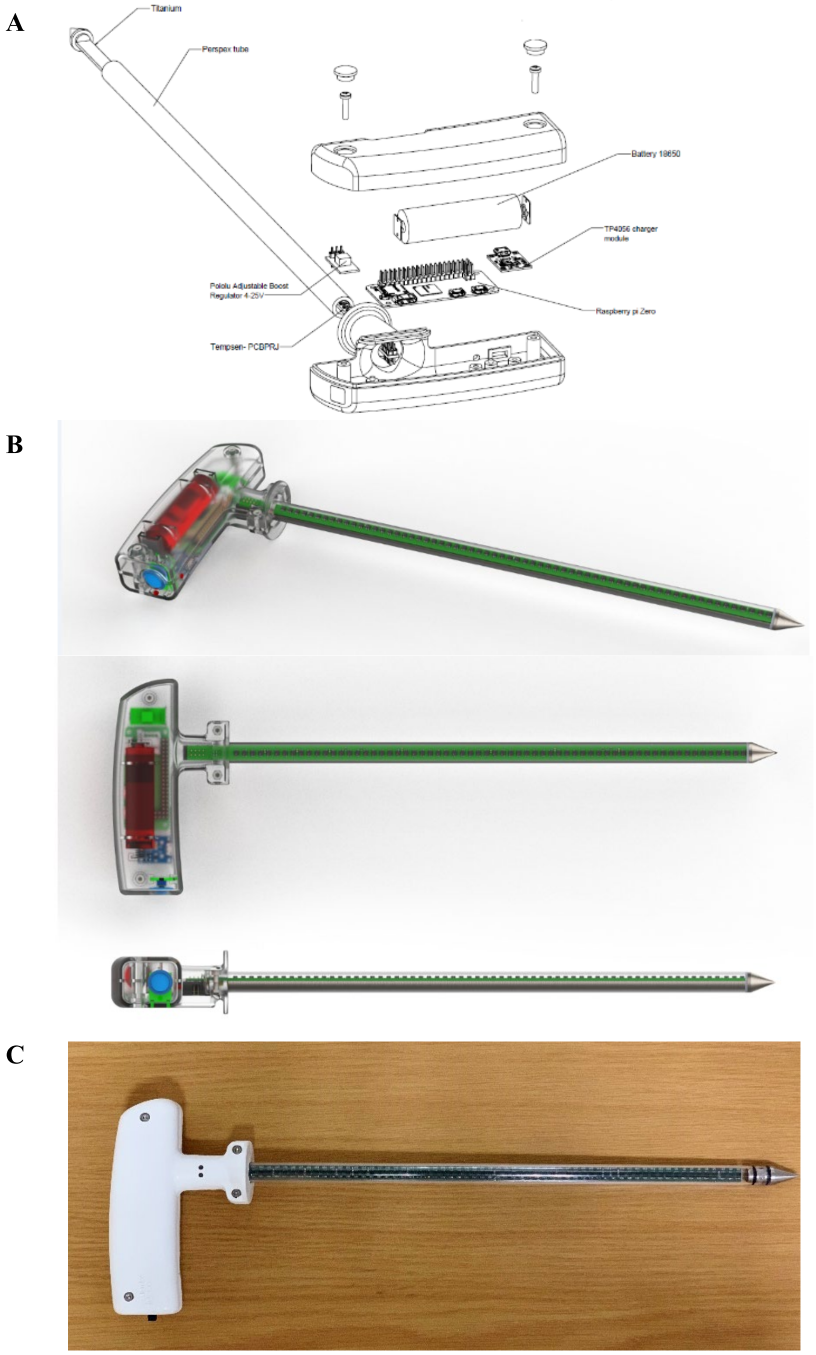

Fig. 8.1 – The multipoint axial thermometry device prototype. **A** indicates schematic drawings. **B** indicates photorealistic computer renditions with a translucent cover. **C** indicates the final fabricated prototype.

The T-shaped handle part was 3D-printed using polyamide (nylon). It housed an on-off toggle switch, a rechargeable Samsung ICR18650 Li-ion battery[2], a 32GB mini-SD card[3], a mini-USB charging port and a Raspberry Pi Zero[4]. The latter was a mini-processor that created a Wi-Fi hot-spot around the device to which a laptop, smartphone or tablet could be connected using a password. The user could type the device's webpage address on any web-browser and real-time temperature measurements from the 62 sensor-chips would be displayed. A feature on the webpage allowed recording of temperature measurements at 1-second intervals for a total of 180s per measurement event. Thereafter, a .cvs file was automatically created for each measurement event containing 11160 values (62 sensor-chips x 180s), the times of their measurement, and the corresponding sensor-numbers. An icon pop-up menu would then be displayed to either download or email the cvs file. The device could store several .cvs files at a time. A patent application is pending[5].

8.1.2 The Cooling Dummy

Due to legal and logistical constraints regarding access to and measurement of axial isotherms from corpses, which would have been the ideal gold-standard, a cooling dummy was built by filling a 771mm long cylindrical polyvinylchloride punching bag with 70L of a special gel solution consisting of 47.5% glycerol, 47.5% distilled water and 5% agar. This formula had been used to build cooling dummies in past studies[6,7,8,9,10,11,12]. The cooling dummy is depicted in Fig. 8.2. Its diameter was 340mm, comparable to that of the abdomen of a large adult. The cooling dummy mass was 80.0kg.

Fig. 8.2 – The cooling dummy suspended during free-air cooling.

8.2 Methods for Empiric Multipoint Axial Thermometry

8.2.1 Postmortem cooling in free air

The cooling dummy was heated to 37°C in an incubator and, upon its removal, tied by its suspension belts to legs of the metal trolley used to transport it. The cooling dummy was placed on a small blanket on the metal trolley for insulation during transportation. The trolley was then placed outdoors in open air and tilted vertically to suspend the cooling dummy.

8.2.2 Multipoint axial thermometry

The multipoint thermometry device was first calibrated in ice-water at 0°C. Thereafter the device was inserted normal to the long axis and surface of the suspended cooling dummy at a height of 360mm. The intention was to have sensor-chips traverse the full diameter of the cooling dummy. After full insertion, sensor-chips 61 and 62 were at the level of the skin and outside the cooling dummy, respectively, while the rest of the sensor-chips were inside the cooling dummy. The tip of the stainless-steel introducer penetrated the opposite end of the cooling dummy and protruded by ~4mm. Thereafter, the multipoint thermometry device's date and time were calibrated via a laptop connected to the device's Wi-Fi. Postmortem axial isotherms were measured after the device had reached thermal equilibrium with the cooling dummy.

8.3 Results of Empiric Multipoint Axial Thermometry

During any postmortem thermometry, the thermometer is often at ambient temperature so that heat-transfer first occurs between it and the body over a variable period as their temperatures equilibrate. This thermal equilibration interval is unique to every thermometry scenario and, in this study, its length was unknown and therefore had to first be established by a series of sequential measurements while the multipoint thermometry device remained in-situ. Axial isotherm measurements began 3hrs 46 minutes postmortem and continued 3, 7, 12, 16, 19, 23, 28, 36, 40, 43 and 47 minutes thereafter. During that entire interval, measurements from the 62 temperature sensors were observed to be in constant but slight fluctuation from second-to-second while they were simultaneously gradually increasing. Thermal equilibration was only observed 50 minutes after the first measurement, i.e. 4hrs 32 minutes postmortem. The final temperature measurements used were therefore at 4hrs and 32minutes and not 3hrs 46minutes postmortem.

The length of the device probe was shorter than the diameter of the cooling dummy. Consequently, postmortem isotherms could not be measured through the entire diameter of the cooling dummy. Plotted measurements of all isotherms (Fig. 8.2) exhibited a parabolic curve that showed data missing on one end due to the length / diameter discrepancy. Measurements from sensor-chip 61 and 62 were thus omitted in the analysis.

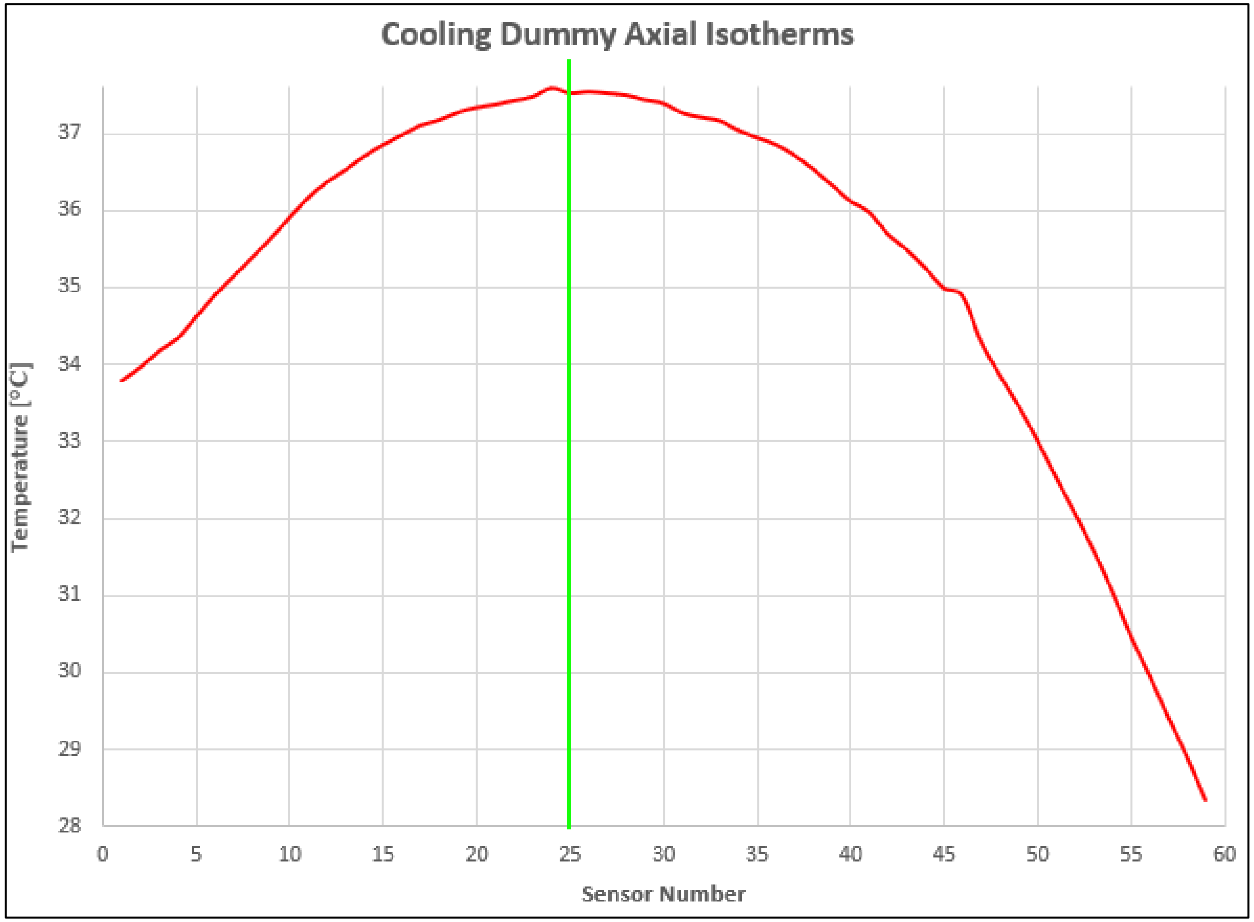

Fig. 8.4 – Axial isotherms measured from the cooling dummy 4 hours and 32 minutes after death. Abscissa indicates the centre of the body. The green abscissa represents the centre of the cooling dummy

8.4 Discussion – Empiric Multipoint Axial Thermometry

The parabolic nature of the curve in Fig. 8.4 was consistent with the existence of isotherms symmetrical around the centre of the cooling dummy. The highest recorded temperature was 37.5°C measured by sensor-chips 24 to 28. This represented the central isotherm whose diameter was at least 25mm (sensor-chips were spaced 5mm apart). This central isotherm was suspected of being the one that existed antemortem, i.e. the PMTP, caught as it was about to disappear. Further, the author was of the opinion that it was entirely plausible that a body with a 175mm radius could have an antemortem central isotherm lasting 4 hrs 32 min when cooling in natural convection. Axial core thermometry at 175mm from the skin using a traditional single-point thermometer at this PMI would obviously measure the PMTP despite significant cooling of the dummy having occurred that radial depth. It was easy to appreciate how variations in core-thermometry depth using a traditional single-point thermometer would result in measurement of different values, a source of uncertainty of death-time estimation discussed in earlier chapters of this thesis.

8.5 Materials – Numerical Multipoint Axial Thermometry

8.5.1 The 3D computational phantom, thermal solver, and computer hardware

The 3D computational phantom, thermal solver and computer hardware used in simulation of postmortem axial isotherm measurement were identical to those used in chapters 6 of this thesis.

8.5.2 A virtual multipoint thermometry device

The business end of the device consisting of the introducer and shaft was modelled as realistically as possible in Sim4Life® using its known design features, see Fig 8.3. Thermophysical properties individually assigned to its 68 parts are indicated in Table 8.1.

Material	**Density (kgm^{-3})**	**Thermal conductivity (W/m/K)**	**Specific Heat (J/kg/K)**
316-grade stainless-steel	8000	16.3	500
Perspex	1051	0.2	1.8
Printed circuit board	2700	9	396
Rubber (gaskets)	1522	0.16	1050
Sensor-chip	2700	383	380

Table 8.1 Thermophysical parameters assigned to components of the virtual multipoint axial thermometry device.

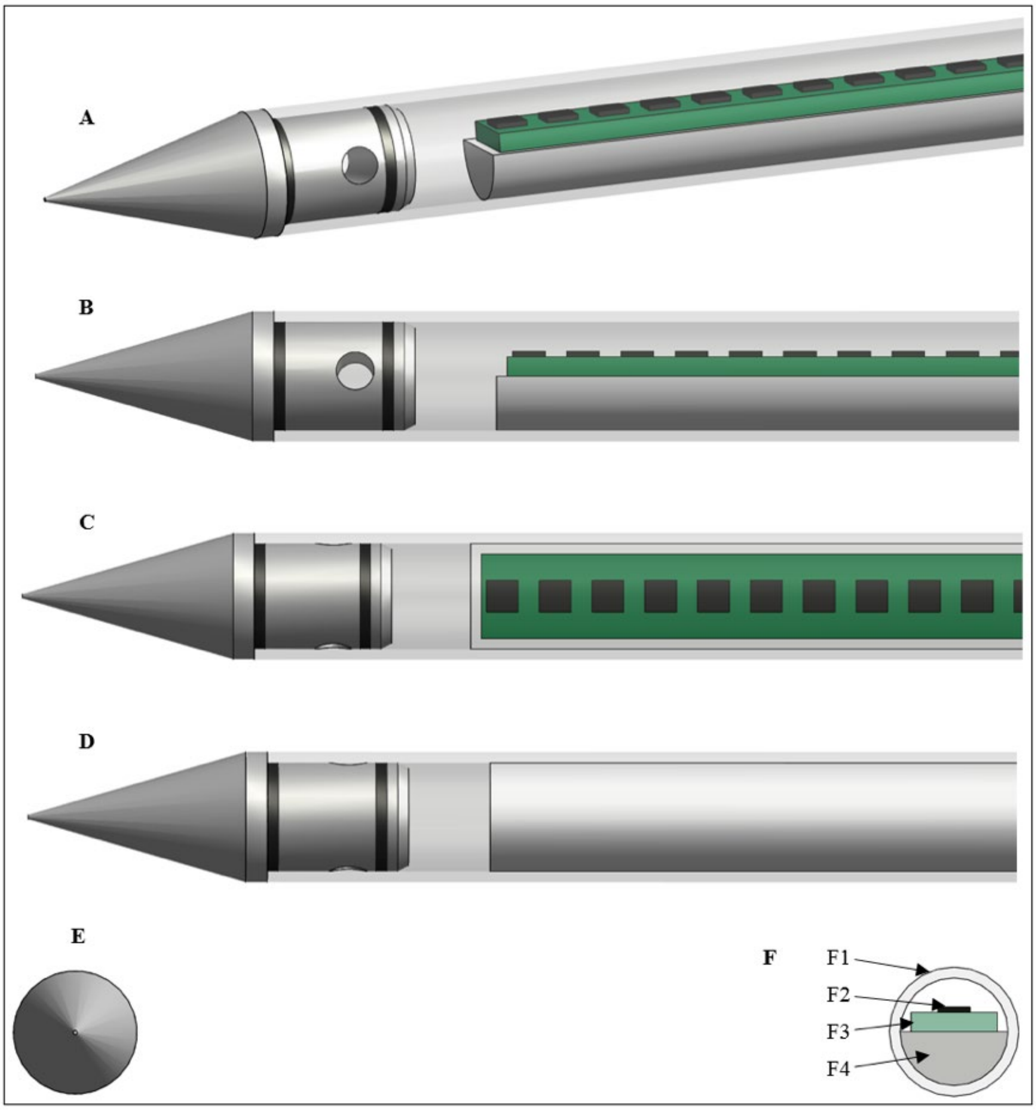

Fig. 8.3 The realistically modelled MAT device. **A, B, C, D, E** and **F** indicate oblique, side, top, bottom, front, and cross-section views, respectively. **F1, F2, F3** and **F4** indicate the Perspex tube, sensor-chip, printed circuit board and 316-grade stainless-steel rod, respectively.

8.6 Methods – Numerical Multipoint Axial Thermometry

The steady-state simulation described in chapter 7 in which the adult male 3D computational phantom Duke cooled in free air over a 5-hour interval was applied as the initial condition in this study. The virtual multipoint thermometry device was then inserted at a 5hr PMI in the right thigh of the 3D computational model. The initial temperature of the virtual multipoint thermometry device was identical to the ambient air temperature. Allowance was made for thermal equilibration, after which temperatures of the virtual sensors were obtained.

8.7 Results and Discussion – Numerical Multipoint Axial Thermometry

Existence of postmortem axial isotherms in all body parts was numerically demonstrated in chapter 7, but their simulated measurement with a virtual device had not been performed. In this numerical multipoint axial thermometry exercise, isotherm sensor-chips traversed the entire circumference of the thigh, leaving several sensor-chips outside the body anteriorly and posteriorly. This was the ideal manner of using the multipoint thermometry device. The isotherm curve exhibited flattened parabolic shape similar to that of the antemortem parasagittal chest curve shown in chapter 6, but obviously having lower temperatures. A key uncertainty in this simulation could be inter-component heat transfer, i.e. contact thermal resistance. The thermal characterization of the probe fell outside the scope of this study. It was concluded from this observation that the antemortem axial thermal profile is preserved postmortem, and that postmortem axial isotherms are measurable from all anatomical sites. Fig. 8.4 indicates 5hr postmortem axial isotherm curves from the right thigh.

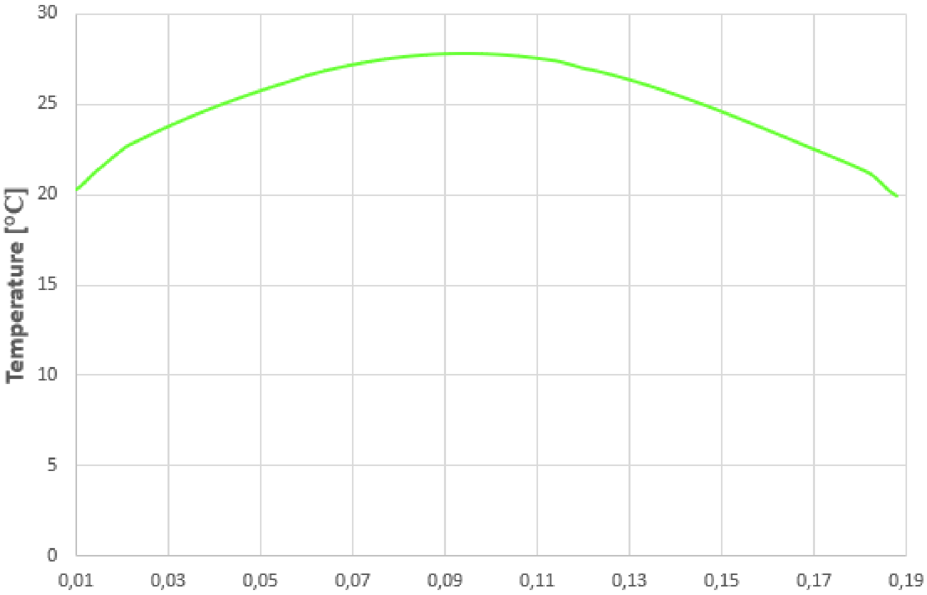

Fig. 8.4 The numerically simulated five-hour multipoint axial thermometry curve from the right thigh of Duke.

8.8 Conclusions

This chapter practically demonstrated MAT in a cooling dummy and numerically simulated it in a high-fidelity 3D computational phantom. MAT was therefore found to be a viable alternative to single-point thermometry for death-time estimation. This chapter proposes MAT using principles of the proposed device for death-time estimation.

Bibliography and cited references

1. Maxim Integrated Products Inc. (2016). MAX30205 Human body temperature sensor [Whitepaper].

2. Samsung SDI Co., Ltd (2005). Specification of product for lithium-ion rechargeable cell Model ICR18650-26A [Whitepaper].

3. Huawei Technologies Co., Ltd (2017). SC Card Technical White Paper [Whitepaper].

4. Broadcom Inc. (2012). BCM2835 ARM Peripherals [Whitepaper].

5. Mfolozi S (2020). Methods and systems of determining a time of death. UK Patent Application No. 2016836.5.

6. Henβge C, Hahn S, Madea B (1986). Praktische Erfahrungen mit einem Abkühlungdummy. (Practical experience with a body-cooling dummy. German, summary in English). Beitr. Gerichtl. Med., 44:123-126.

7. Henβge C, Madea B, Schaar U, Pitzken C (1987). Die Abkühlung eines Dummy unter verschiedenen Bedingungen im Vergleich zur Leichenabkühlung (The cooling of a dummy under various conditions in comparison with body cooling. German, summary in English). Beitr Gerichtl Med., 45:145-149.

8. Althaus L, Henssge C (1999). Rectal temperature time of death nomogram: sudden change of ambient temperature. Forensic Science International, 99:171-178.

9. Bisegna P, Henβge C, Althaus L, Giusti G (2008). Estimation of the time since death: Sudden increase of ambient temperature. Forensic Science International, 176:196-199.

---

10. Henβge C (1992). Rectal temperature time of death nomogram: Dependence of corrective factors on body weight under stronger thermic insulation conditions. Forensic Science International, 54(1):51-66.

11. Althaus L, Stückradt S, Henβge C, Bajanowski T (2007). Cooling experiments using dummies covered by leaves. International Journal of Legal Medicine, 121:112-114.

12. Eagle MJ, Rooney P, Kearney JN (2007). Investigating the warming and cooling rates of cadavers by development of a gel-filled model to validate core temperature. Cell Tissue Banking, 8:297-302.

CHAPTER 9

A numerical protocol for death-time estimation

Chapter 9

A numerical protocol for death-time estimation

Chapter 8 of this thesis demonstrated MAT both empirically and numerically using a proposed MAT device. This chapter proposes a numerical protocol of death-time estimation in which the MAT profile from a body found dead is iteratively compared to the MAT profiles from numerical simulations of increasingly longer candidate PMIs using a comparable 3D computational phantom to represent the body. Application of MAT would eliminate uncertainties of single-point thermometry discussed in preceding chapters of this thesis. In addition, the proposed numerical protocol applies historical periodic meteorological air temperatures that would have existed during the PMI of the body as far as recorded by the nearest weather station, without requiring the TOD to average meteorological air temperatures. An investigator wishing to implement the proposed protocol would be expected to first collect the required data from the decedent and death scene, which in the next section are described prior to description of the proposed protocol.

9.1 Data Collection

9.1.1 Examination of the Body

The weight and height of the body are to be measured and the sex established. The exact clothing items on the body are noted and enumerated. Body position (supine, prone, lateral, foetal) is noted with reference to contact with the ground-surface. Circumferences of the head, chest, abdomen, upper and lower limbs are measured, and the height of each measurement is noted. This information assists in selecting the most appropriate 3D computational phantom for the analysis.

9.1.2 Multipoint axial thermometry

The numeric study in chapter 8 demonstrated measurement of postmortem axial isotherms from the thigh. The choice of anatomic site would depend on various factors, including the user's personal preference, the desire to preserve pre-existing injuries that may have played a role in the death, the desire to avoid creating new / postmortem artefacts and the need to demonstrate isotherm shifting due to the ground-surface. To detect isotherm shifting in a body on the ground, insertion of the multipoint thermometry device must be normal to the ground. The body circumference at the insertion site is to be measured using a tape-measure. The multipoint thermometry device temperature must first be allowed to equilibrate with the body before thermometry using a series of preliminary measurements.

It was the author's opinion from the chapter 8 studies that simulated isotherm measurement in the 3D computational phantom that the proximal thigh was a suitable candidate site for device insertion because its bulk mass is predominantly skeletal muscle seldom dissected at autopsy. Device insertion through the centre of the thigh would not be impeded by the femur bone as the latter is not in the geometric centre. Device insertion into the chest would not only be impeded by the ribs, sternum and spinal column but would obviously create artefactual postmortem injuries to solid and hollow thoracic viscera. Device insertion into the abdomen carries the risk of bowel perforation, while insertion into the head would be impeded by the skull. In many death scenes the thigh rests on the ground in the supine or lateral positions, which would permit demonstration of the resultant isotherm shift effect if present. Moreover, the thigh has a more or less circular axial circumference that is relatively easy to measure for comparing morphometric similarity with the 3D computational phantom to be selected for numerical simulation.

9.1.3 Death Scene Investigation

The type of ground-surface on which the body is discovered is to be noted and photographed. Its temperature is to be measured where possible and effort made to establish its composition and thermophysical properties. A measurement of the ambient air temperature in the immediate vicinity of the body is to taken using an appropriate air thermometer if indoors.

9.1.4 Historical Meteorological Records

Records of historic air temperature measurements are to be obtained from the nearest weather station for the 72 hours preceding the discovery of the body. The periodicity of meteorological air temperature measurements is to be noted, e.g. 2-hourly, 1-hourly, half-hourly, or haphazardly. This information is often supplied in the record.

Although dedicated official weather stations are almost ubiquitous in urban areas of developed countries, in rural areas or underdeveloped nations weather stations may be few and far in-between. In many urban areas, private citizens keep private weather stations in their homes, and often publish their historical data in dedicated websites. An investigator who wishes to apply the proposed protocol visit such websites as www.wunderground.com[1] or similar to search for a weather station nearest to them.

9.2 The Proposed Multipoint Axial Thermometry Protocol

In the proposed MAT Protocol, the MAT profile measured from a decedent at an unknown PMI using the proposed MAT device is iteratively tested against MAT profiles predicted by numerical simulations of sequentially longer candidate PMIs, beginning from a candidate PMI of 0hrs (the time of MAT). A 3D computational human phantom of comparable anthropometry to the decedent. When MAT profiles do not match, the candidate PMI is excluded and a new, slightly longer candidate PMI is tested. A candidate PMI whose MAT profile matches is regarded as the final PMI estimated by the protocol. The MAT Protocol consists of one so-called 'antemortem' simulation (AM) that approximates the decedent's antemortem body temperature distribution, and one or more 'postmortem' simulations (PM) that predict postmortem cooling over a specified interval.

A candidate PMI of 0hrs requires only the one AM simulation, in which the ambient air temperature measured at the death scene is applied to the boundary condition. Any candidate PMI longer than 0hrs requires one AM simulation as well as at least one PM simulation whose initial condition is the solution of the AM simulation. More than one PM simulations may be required to test a candidate PMI. In such an instance the solution of the preceding PM simulation forms initial conditions of the subsequent PM simulation. The historical meteorological data collected as described earlier are to be applied to boundary conditions of PM simulations in a sequence that tests a candidate PMI in question. A PM simulation may be of any length, provided the correct air temperature value from the meteorological record that corresponds to the cooling interval concerned is applied in the boundary condition. Periodic differences of air temperature measurements in a meteorological record may require several PM simulations whose lengths correspond to the duration of temperature measurement in the record. Each periodic temperature value would then be applied in the boundary condition of each simulation.

A last PM simulation in a sequence to test a candidate PMI represents thermal equilibration and isotherm measurement using a virtual multipoint axial thermometry device. The simulation interval of this final PM simulation must be subtracted from that of the preceding PM simulation. The MAT Protocol is schematically depicted in Fig. 9.1 where 1hr increments are used and where postmortem axial isotherms are measured at the turn of the hour.

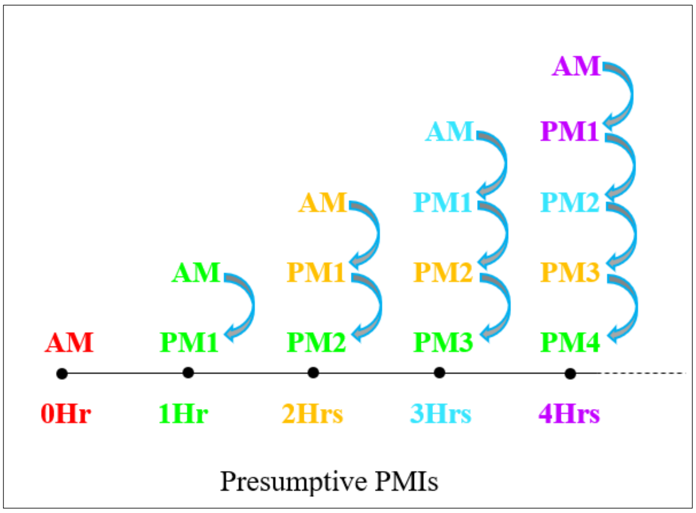

Fig. 9.1 A schematic representation of the proposed MAT Protocol. AM = antemortem simulation, PM = postmortem simulation. The horizontal line represents time and dots represent candidate PMIs. The simulation-sequence for each candidate PMI is indicated above each dot. Curved arrows indicate direction of simulation solutions as they become initial conditions. Colour-coding represents air temperature to be applied in boundary condition. The direction of iteration is left to right.

As can be seen in Fig. 9.1, the number of PM simulations performed when testing a candidate PMI increase with the length of the candidate PMI being tested. The colour-coding highlighted the unique sequence historical meteorological temperatures are applied in PM simulations for candidate PMIs being tested, which cannot be applied in another candidate PMI. Practically, however, PM simulations can be stacked in the simulation software and ambient temperature settings can be simply be reset to the correct sequence to test the next candidate PMI sequence without recreating each simulation-sequence from scratch.

The MAT Protocol may be commenced at any candidate PMI and not necessarily always at 0hrs, although doing so helps to monitor the comparison trend. Also, the time difference between candidate PMIs does not have to be a fixed and may be continuously adjusted depending on the proximity of the simulated MAT profile to the reference MAT profile. With enough computational resources, the MAT Protocol may be implemented simultaneously on multiple computer platforms, wherein a simulation-sequence that tests a specific candidate PMI is undertaken by on dedicated platform. A match in one platform would thus negate further analyses in the other platforms. In such a scenario, platforms would obviously have to be synchronised. Abundant computational resources would shorten not only the computational time but also allow for infinitesimally small increments between candidate PMIs, significantly increasing temporal resolution of the final predicted PMI to the order of seconds. This would be especially true if as many variables known to affect postmortem cooling as possible are included in the numerical analyses.

9.2.1 Object-modelling in proposed protocol simulations

Simulations in the proposed protocol should reflect the probable antemortem and postmortem position of the decedent deduced from examination of the death-scene. The ground-surface is to be modelled accurately in the simulation environment and the appropriate thermophysical properties assigned to it. A representative 3D computational phantom must be chosen and positioned on the ground-surface in the same manner the decedent's body was documented at the scene. If the need arises, joints of the 3D phantom must be manipulated to pose the phantom in the same manner the dead body was discovered. Correct posing would reproduce contact points with the ground, allowing heat transfer and shifted isotherm to be accurately simulated. Sim4Life® possessed a poser function that positions the underlying rigid skeleton by specifying the required orientation at articulated joints. Once a user was satisfied with the position of the bones, the poser tool deformed the complete anatomical model into the prescribed posture. Fig. 9.2 illustrates various possible poses.

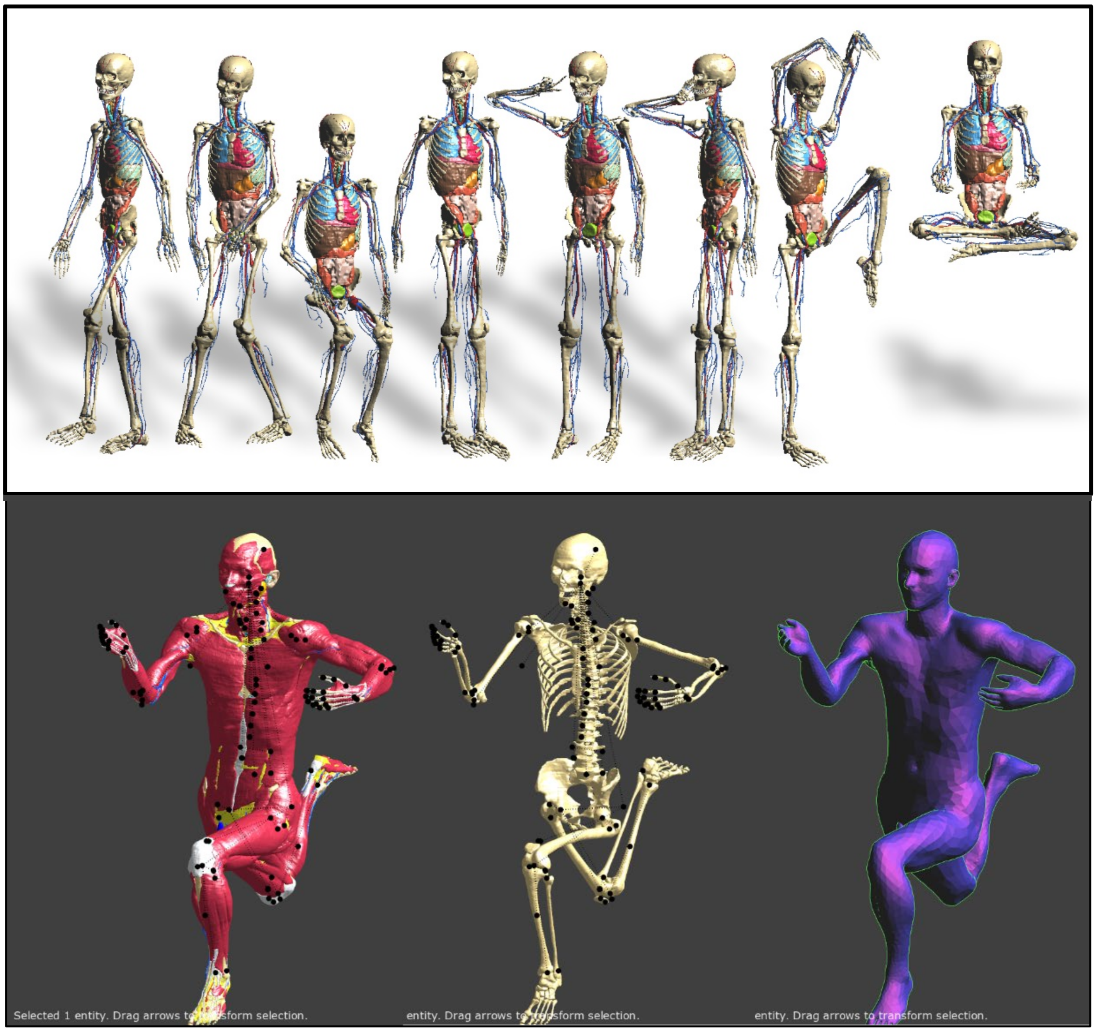
Selected 1 entity. Drag arrows to transform selection.
entity. Drag arrows to transform selection.
entity. Drag arrows to transform selection.

Fig. 9.2 Various poses achievable using the poser tool of Sim4Life®.

9.3 MAT comparison and death-time estimation

The MAT profile downloaded from the MAT device should exlude data recorded during thermal-equilibration. A virtual MAT device identical to the proposed MAT device must constructed in the simulation environment and used to measure simulated isotherms from the 3D computational phantom at a comparable anatomical site. A simulated MAT profile is compared to the MAT profile measured from the body at an unknown PMI, using statistical analysis methods if necessary. The candidate PMI whose MAT value matches is regarded as the final PMI estimated by the MAT Protocol.

9.4 Demonstration of the MAT Protocol

9.4.1 Circumstances of death

The ideal gold-standard to demonstrate the MAT Protocol would have been case-work using recently deceased human body, along with the materials and methods described in chapters 6, 7 and 8 of this thesis. However, this was not possible, as previously stated in chapter 8, therefore a fictitious scenario was used to demonstrate application of the protocol commencing after MAT from a dead body.

The scenario was as follows: On the morning of Saturday April 22nd 2018 the naked body of a 70.2kg, 1.77m tall male had been found hanging by the neck from a tree in a wooded area. The body bore marks of non-fatal torture. The global positioning system (GPS) coordinates of the body were 40°46’40” N, 73°58’11” W. The MAT device was inserted at 11H25 local-time through the proximal aspect of the right thigh in the parasagittal plane where the thigh circumference was 50cm. Thermal equilibration took 8 minutes (500s) and the final MAT measurement was obtained at 11H33, whose curve is plotted in Fig. 9.3. A corresponding excel spreadsheet with temperatures values and respective sensor numbers was provided. The ambient air temperature measured next to the body at 11H33 was 15.1°C. The task was to apply the MAT Protocol to estimate the PMI and/or time of death using the information provided.

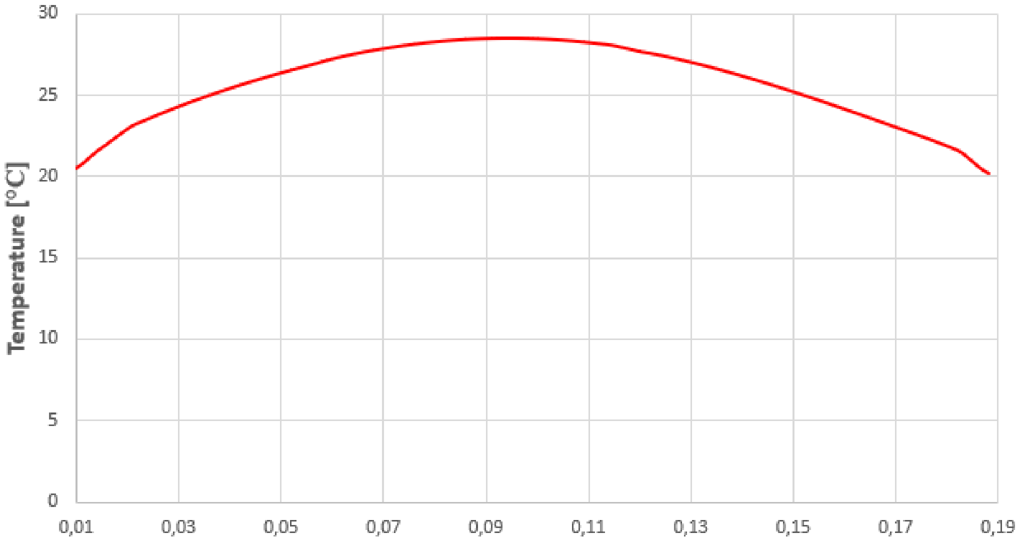

Fig. 9.3 The provided MAT curve measured from the right thigh of the dead body at an unknown PMI to be used in the MAT Protocol.

9.4.2 Pre-analysis preparations

The first step was to acquire historical meteorological data from the nearest weather station using the information provided. A readily available GPS-map desktop application (Google Earth) established that the provided GPS coordinates were of a densely wooded location in Central Park of New York City in the USA, consistent with the information provided. A historical meteorological record of that location for April 22nd 2018 was obtained from www.wunderground.com[2]. The meteorological record indicated recording intervals of one hour, 51 minutes into each hour, as indicated in Table 9.1.

Time	Measured air temperature
11H51	16.7°C
10H51	13.9°C
09H51	12.2°C
08H51	10.6°C
07H51	8.9°C
06H51	7.8°C
05H51	6.7°C
04H51	7.9°C
03H51	8.3°C
02H51	8.9°C
01H51	10.0°C
00H51	11.1°C

Table 9.1 The historical meteorological temperature record of Central Park, NYC, USA for 22nd April 2018 applied to the MAT Protocol.

The hourly periodic nature of this meteorological record meant that air temperatures were not recorded for 59 of the 60 minutes of all hours reflected on the record. The MAT Protocol, on the other hand, required air temperatures at times other than those provided in the record because TOD was unknown and may be any time. The MAT Protocol had to be able to test any candidate PMI/TOD without being restricted by unavailability of meteorological data. To overcome this limitations, the 'per-minute rate of temperature change' within a 1-hour interval in the record was assumed to be linear and calculated using the formula:

$$R = \frac{T_y - T_x}{t}, \qquad t = y - x \tag{9.1}$$

where R was the per-minute rate of temperature change between times x and y, T_x was air temperature recorded at time x, T_y was air temperature recorded at time y, t was the difference in minutes between times x and y (60 minutes), and time x existed before time y. Table 9.2 indicates per-minute temperature change rates of the meteorological record calculated using eqn. 9.1.

Time interval (time x) - (time y)	**Per Minute Temperature Change Rate (°C/min)**
00H51 - 01H51	–0.0183
01H51 - 02H51	–0.0183
02H51 - 03H51	–0.01
03H51 - 04H51	–0.007
04H51 - 05H51	–0.02
05H51 - 06H51	+0.0183
06H51 - 07H51	+0.0183
07H51 - 08H51	+0.0283
08H51 - 09H51	+0.0267
09H51 - 10H51	+0.0283
10H51 - 11H33	+0.0286

Table 9.2 Calculated per-minute rates of temperature change used to interpolate air temperature at any arbitrary time within these intervals.

To interpolate air temperatures for any arbitrary time within a 1-hour interval in Table 9.2, the following equation was used:

$$T_w = T_x + Rt_w, \qquad t_w = w - x \tag{9.2}$$

where T_w was air temperature at arbitrary time w, T_x was air temperature at time x for the 1-hour interval concerned, R was the per-minute rate of temperature change for the 1-hour interval concerned, t_w was the number of minutes between time x and time w, and time x existed before time w. Air temperatures interpolated using eqn. (9.2) would then be applied in boundary conditions of all AM simulations and used to calculate air temperatures of cooling intervals for PM simulations as required by the protocol. Cooling intervals for PM simulations were made to be 1-hour long to be consistent with the hourly periodicity of the meteorological record and to avoid averaged temperature over very long postmortem cooling intervals as discussed in earlier chapters.

9.4.3 Candidate PMI of 0hrs

For the candidate PMI of 0hrs, a steady-state simulation that assumed the TOD was 11H33 was undertaken using the adult male 3D computational phantom Duke. No ground-surface was modelled because the body in the given scenario had been found hanging from a tree. Joints of the 3D computational phantom were not posed either because the body was erect. The ambient temperature value of 15.1°C measured next to the body at the time of isotherm thermometry was applied in the boundary condition of the AM simulation. The heat transfer coefficient value applied to the boundary condition was 9.5 $W/m^2/K$ for a vertical cylinder cooling in natural convection conditions[3]. These settings were applied throughout the protocol. The simulation interval was set to 9000s, based on experience from chapter 6.

On completion of the above AM simulation, a 500s-long simulation representing postmortem cooling and thermal equilibration during MAT from 11H25 to 11H33 was carried out. The calculated air temperature at 11H25 using eqn. (9.2) was 14.872°C, while the measured air temperature at 11H33 was 15.1°C. Therefore, the calculated mean air temperature from 11H25 to 11H33 was 14.988°C, which was applied to the boundary condition. The virtual MAT device was inserted where the phantom's thigh had a circumference of 50cm. Fig. 9.3 indicates the isotherm curve for the candidate PMI of 0hrs plotted with the reference isotherm curve from the dead body. The two curves were clearly not match, even without statistical analysis, therefore an increment of 1 hour was arbitrarily added to the candidate PMI and the protocol was repeated.

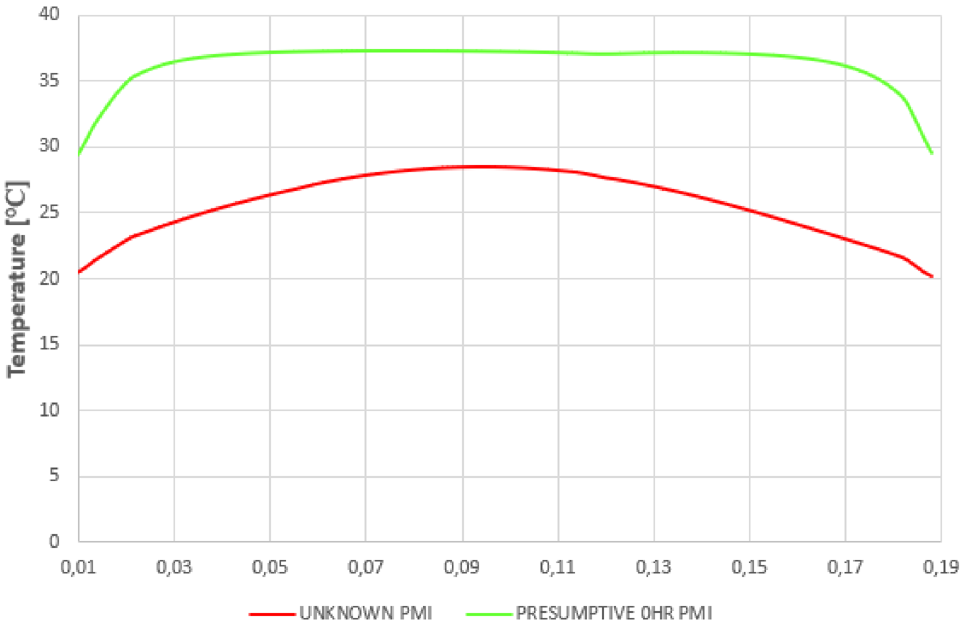

Fig. 9.4. Comparison of the 0hr candidate PMI isotherm curve with the reference curve from the unknown PMI.

9.4.4 Candidate PMI of 1hr

A candidate PMI of 1hr meant that the assumed TOD was 10H33. Using eqn. (9.2), the calculated air temperature at 10H33 was 13.389°C, which was applied in the boundary condition of the AM simulation whose interval was set to 9000s.

The solution of the above simulation was applied in initial conditions of 3100s-long PM-1 simulation to simulate postmortem cooling between 10H33 and 11H25. The calculated air temperature at 11H25 was 14.872°C, therefore the calculated mean air temperature between 10H33 and 11H25 was 14.1305°C, which was applied in the boundary condition.

The solution of the above simulation was then applied in initial conditions of the 500s-long simulation to simulate postmortem cooling and/during thermal equilibration between 11H25 and 11H33 during isotherm measurement. The given measured air temperature at 11H33 was 15.1°C, therefore the calculated mean air temperature of this interval was 14.988°C, which was applied to the boundary condition. The virtual MAT device was inserted where the 3D phantom’s thigh had a circumference of 50cm. Fig. 9.5 indicates the isotherm curve for the candidate PMI of 1hr plotted with the reference isotherm curve from the decedent.

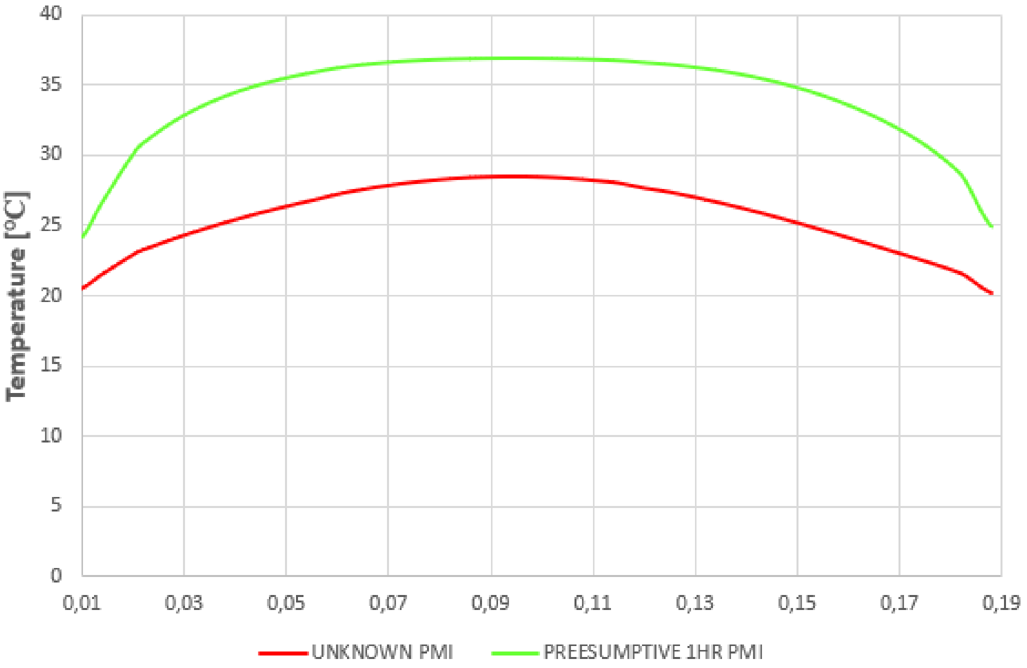

Fig. 9.5. The 1hr candidate PMI isotherm curve plotted with the reference curve from the unknown PMI.

The 1hr candidate PMI isotherm curve was slightly more parabolic than that of the 0hr counterpart, beginning to take a similar form to that of the reference isotherm curve but not enough to be a match. Therefore, an increment of 1 hour was arbitrarily added to the candidate PMI and the protocol was repeated.

9.4.5 Candidate PMI of 2hrs

A candidate PMI of 2hr meant that the assumed TOD was 09H33. Using eqn. (9.2), the calculated temperature at 09H33 was 11.789°C, which was applied in the boundary condition of the AM simulation whose interval was set to 9000s.

The solution of the above AM simulation was applied in initial conditions of PM-1 simulation to simulate postmortem cooling between 09H33 and 10H33. The calculated air temperature at 10H33 was 13.389°C, therefore the calculated mean air temperature of this interval was 12.589°C, which was applied in the boundary condition.

The solution of the PM-1 simulation was applied in initial conditions of 3100s-long PM-2 simulation to simulate postmortem cooling between 10H33 and 11H25. The calculated air temperature at 11H25 was 14.872°C, therefore the calculated mean air temperature between 10H33 and 11H25 was 14.1305°C, which was applied in the boundary condition.

The solution of the PM-2 simulation was then applied in initial conditions of the 500s-long simulation to simulate thermal equilibration between 11H25 and 11H33 during isotherm measurement. The measured air temperature at 11H33 was 15.1°C, therefore the calculated mean air temperature 11H25 and 11H33 was 14.988°C, which was applied to the boundary condition. The virtual MAT device was inserted where the 3D phantom's thigh had a circumference of 50cm. Fig. 9.6 indicates the isotherm curve for the candidate PMI of 2hrs plotted with the reference isotherm curve from the decedent.

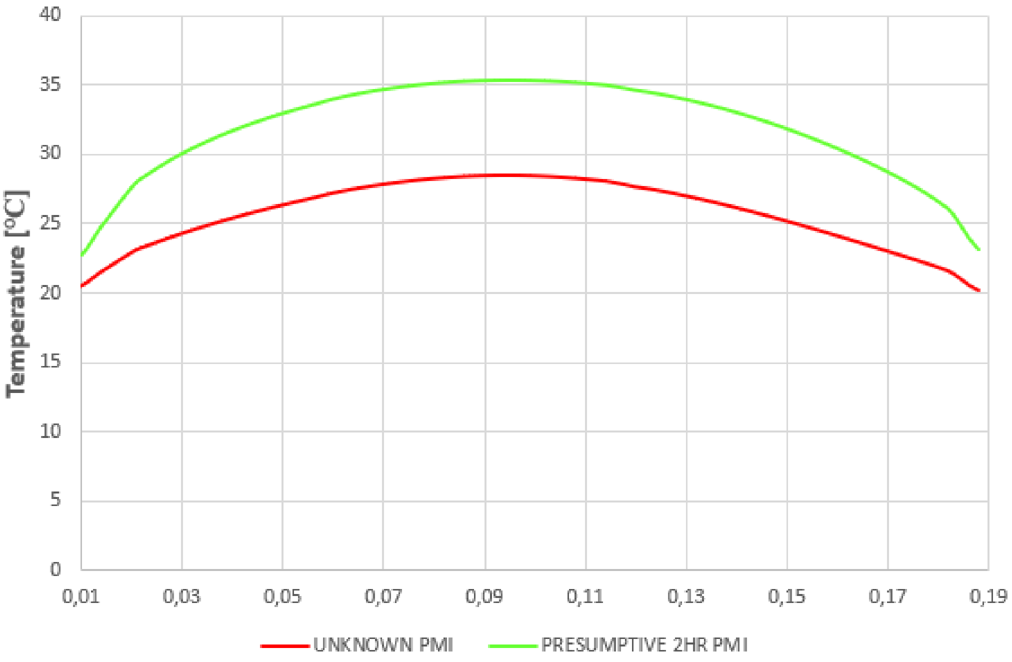

Fig. 9.6. The 2hr candidate PMI isotherm curve plotted with the reference curve from the unknown PMI.

The 2hr candidate PMI isotherm curve was even more parabolic than that of the 1hr counterpart, taking more of the form of the reference isotherm curve but not enough to be a match. Therefore, an increment of 1 hour was arbitrarily added to the candidate PMI and the protocol was repeated.

9.4.6 Candidate PMI of 3hrs

A candidate PMI of 3hr meant that the assumed TOD was 08H33. Using eqn. (9.2), the calculated air temperature at 08H33 was 10.081°C, which was applied in the boundary condition of AM simulation whose interval was set to 9000s.

The solution of AM simulation was applied in initial conditions of the PM-1 simulation to simulate postmortem cooling between 08H33 and 09H33. The calculated air temperature at 09H33 was 11.721°C, therefore the calculated mean air temperature between 08H33 and 09H33 was 10.901°C, which was applied to the boundary condition.

The solution the PM-1 simulation was applied in initial conditions of the PM-2 simulation to simulate postmortem cooling between 09H33 and 10H33. The calculated air temperature at 10H33 was 13.389°C, therefore the calculated mean air temperature between 09H33 and 10H33 was 12.589°C, which was applied in the boundary condition.

The solution of the PM-2 simulation was applied in initial conditions of 3100s-long PM-3 simulation to simulate postmortem cooling between 10H33 and 11H25. The calculated air temperature at 11H25 was 14.872°C, therefore the calculated mean air temperature between 10H33 and 11H25 was 14.1305°C, which was applied in the boundary condition.

The solution of the PM-3 simulation was then applied in initial conditions of the 500s-long simulation to simulate thermal equilibration between 11H25 and 11H33 during isotherm measurement. The measured air temperature at 11H33 was 15.1°C, therefore the calculated mean air temperature between 11H25 and 11H33 was 14.988°C, which was applied to the boundary condition. The virtual MAT device was inserted where the 3D phantom's thigh had a circumference of 50cm. Fig. 9.7 indicates the isotherm curve for the candidate PMI of 3hrs plotted with the reference isotherm curve from the decedent.

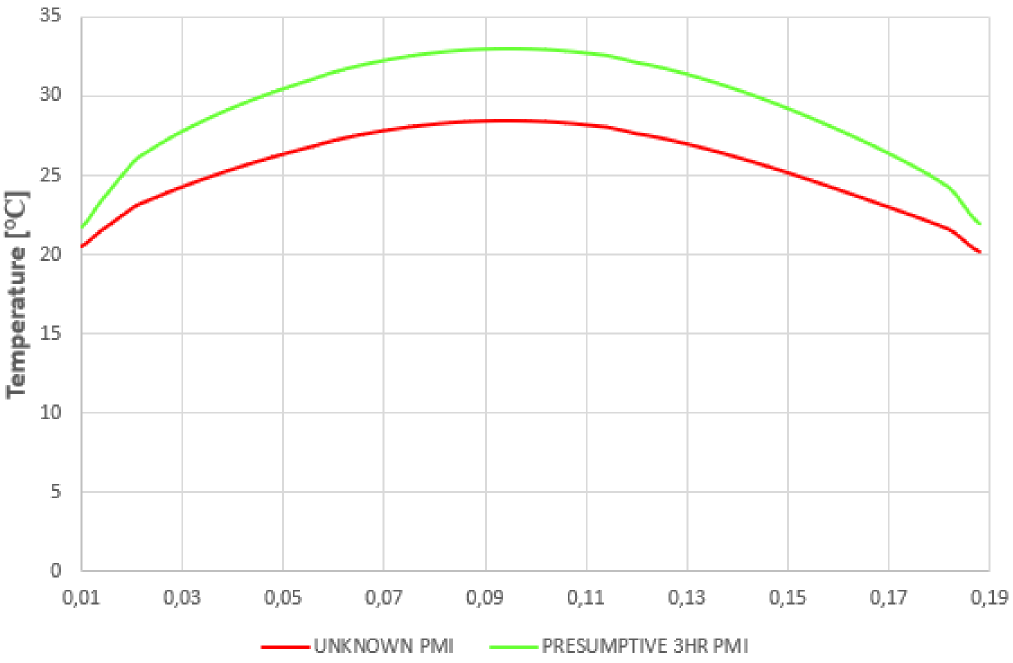

Fig. 9.7. The 3hr candidate PMI isotherm curve plotted with the reference curve from the unknown PMI.

The 3hr candidate PMI isotherm curve was even more parabolic than those of 0hr, 1hr and 2hr candidate PMIs, but not enough to be a match. Therefore, an increment of 1 hour was arbitrarily added to the candidate PMI and the protocol was repeated.

9.4.7 Candidate PMI of 4hrs

A candidate PMI of 4hr meant that the assumed TOD was 07H33. Using eqn. (9.2), the calculated air temperature at 07H33 was 8.569°C, which was applied in the boundary condition of the antemortem simulation whose interval was set to 9000s.

The solution of the above simulation was applied in initial conditions of the PM-1 simulation to simulate postmortem cooling between 07H33 and 08H33. The calculated air temperature at 08H33 was 10.089°C, therefore the calculated mean air temperature between 07H33 and 08H33 was 9.329°C, which was applied to the boundary condition.

The solution of the above simulation was applied in initial conditions of the PM-2 simulation to simulate postmortem cooling between 08H33 and 09H33. The calculated air temperature at 09H33 was 11.721°C, therefore the calculated mean air temperature between 08H33 and 09H33 was 10.905°C, which was applied to the boundary condition.

The solution of the PM-2 simulation was applied in initial conditions of the PM-3 simulation to simulate postmortem cooling between 09H33 and 10H33. The calculated air temperature at 10H33 was 13.389°C, therefore the calculated mean air temperature between 09H33 and 10H33 was 12.589°C, which was applied in the boundary condition.

The solution of the PM-3 simulation was applied in initial conditions of 3100s-long PM-4 simulation to simulate postmortem cooling between 10H33 and 11H25. The calculated air temperature at 11H25 was 14.872°C, therefore the calculated mean air temperature between 10H33 and 11H25 was 14.1305°C, which was applied in the boundary condition.

The solution of PM-4 simulation was then applied in initial conditions of the 500s-long simulation to simulate thermal equilibration between 11H25 and 11H33 during isotherm measurement. The measured air temperature at 11H33 was 15.1°C, therefore the calculated mean air temperature between 11H25 and 11H33 was 14.988°C, which was applied to the boundary condition. The virtual MAT device was inserted where the 3D phantom's thigh had a circumference of 50cm. Fig. 9.8 indicates the isotherm curve for the candidate PMI of 4hrs plotted with the reference isotherm curve from the decedent.

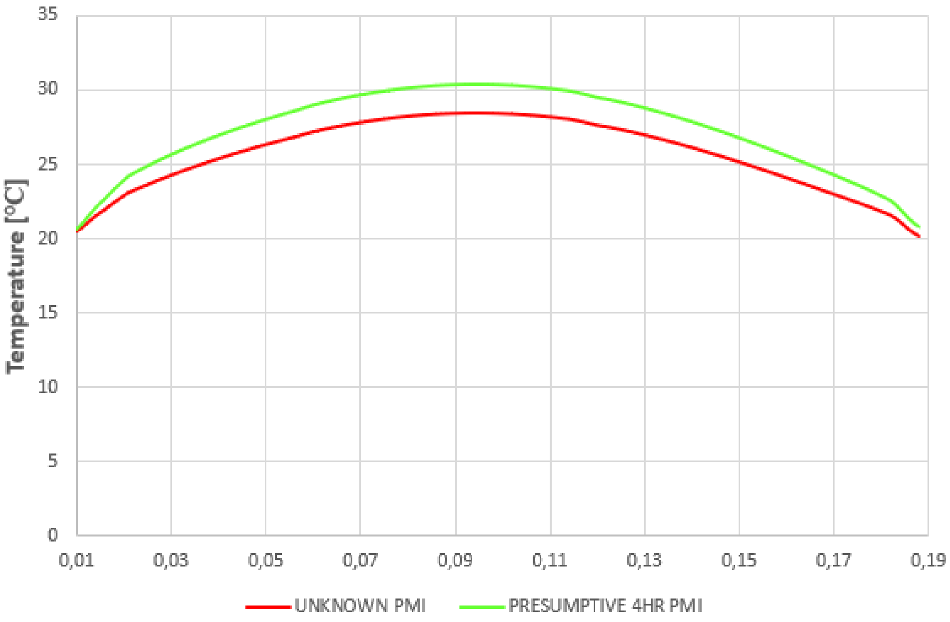

Fig. 9.8. The 4hr candidate PMI isotherm curve plotted with the reference curve from the unknown PMI.

The 4hr candidate PMI curve was very similar to the reference curve but did not align perfectly with it. Therefore, an increment of 1 hour was arbitrarily added to the candidate PMI and the protocol was repeated.

9.4.8 Candidate PMI of 5hrs

A candidate PMI of 5hr meant that the assumed TOD was 06H33. Using eqn. (9.2), the calculated air temperature at 06H33 was 7.4686°C, which was applied in the boundary condition of the AM simulation whose interval was set to 9000s.

The solution of the AM simulation was applied in initial conditions of the PM-1 simulation to simulate postmortem cooling between 06H33 and 07H33. The calculated air temperature at 07H33 was 8.5686°C, therefore the calculated mean air temperature between 06H33 and 07H33 was 8.0186°C, which was applied to the boundary condition.

The solution of the PM-1 simulation was applied in initial conditions of the PM-2 simulation to simulate postmortem cooling between 07H33 and 08H33. The calculated air temperature at 08H33 was 10.089°C, therefore the calculated mean air temperature between 07H33 and 08H33 was 9.329°C, which was applied to the boundary condition.

The solution of the PM-2 simulation was applied in initial conditions of the PM-3 simulation to simulate postmortem cooling between 08H33 and 09H33. The calculated air temperature at 09H33 was 11.721°C, therefore the calculated mean air temperature between 08H33 and 09H33 was 10.905°C, which was applied to the boundary condition.

The solution of the PM-3 simulation was applied in initial conditions of the PM-4 simulation to simulate postmortem cooling between 09H33 and 10H33. The calculated air temperature at 10H33 was 13.389°C, therefore the calculated mean air temperature between 09H33 and 10H33 was 12.147°C, which was applied in the boundary condition.

The solution of the PM-4 simulation was applied in initial conditions of 3100s-long PM-5 to simulate postmortem cooling between 10H33 and 11H25. The calculated air temperature at 11H25 was 14.872°C, therefore the calculated mean air temperature between 10H33 and 11H25 was 14.1305°C, which was applied in the boundary condition.

The solution of the PM-5 simulation was then applied in initial conditions of the 500s-long simulation to simulate thermal equilibration between 11H25 and 11H33 during isotherm measurement. The measured air temperature at 11H33 was 15.1°C, therefore the calculated mean air temperature between 11H25 and 11H33 was 14.988°C, which was applied to the boundary condition. The virtual MAT device was inserted where the 3D phantom's thigh had a circumference of 50cm. Fig. 9.9 indicates the isotherm curve for the candidate PMI of 5hrs plotted with the reference isotherm curve from the decedent.

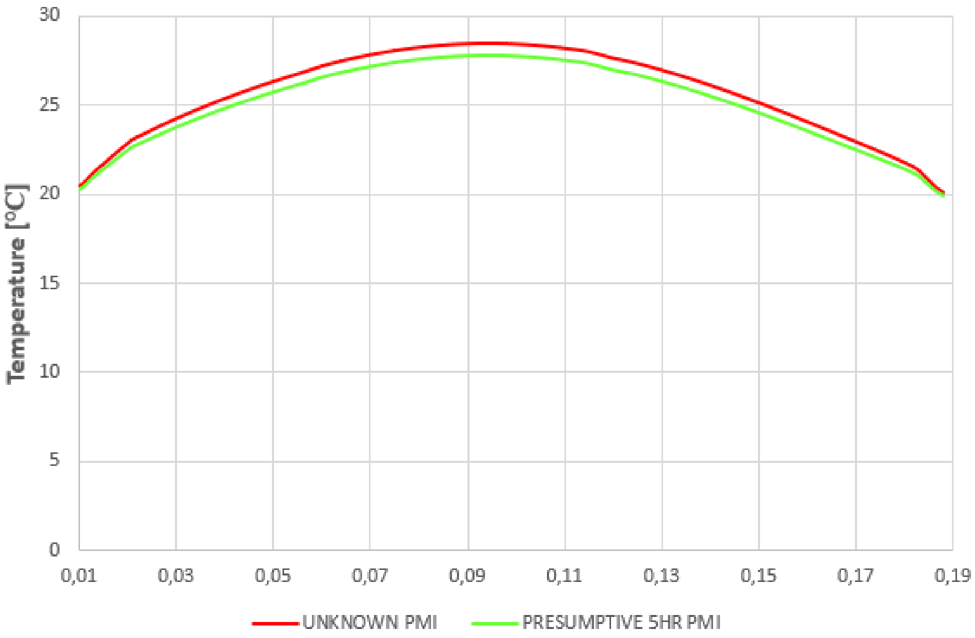

Fig. 9.9A. The 5hr candidate PMI isotherm curve plotted with the reference curve from the unknown PMI.

For the first time in this protocol, the isotherm curve of this candidate PMI had consistently lower temperatures than the reference isotherm curve, i.e. divergence. This indicated that a matching candidate PMI was shorter than 5hrs but longer than 4hrs. The divergence prompted refinement of the protocol's comparative procedure, characterised by stepwise reduction of the added increments to intervals shorter than 1 hour, followed by resumption of the protocol.

9.4.9 Refined Isotherm Curve Comparison

Because of the divergence, the added time increment was reduced from being 1hr to being10 minutes. The protocol was then resumed to test candidate PMIs 4hrs10mins, 4hrs20mins, 4hrs30mins, 4hrs40mins and 4hrs50mins. Times of death, air temperatures at death and air temperatures during postmortem cooling intervals were established for each candidate PMI as described in the previous sections.

9.4.9.1 Candidate PMI of 4hrs10mins

The candidate PMI of 4hrs10mins produced an isotherm curve whose temperatures were higher than the reference curve. This indicated that the target PMI was longer than 4hrs10mins but less than 5hrs and the protocol was continued to the next candidate PMI. Fig. 9.10 indicates the isotherm curve of this candidate PMI plotted with the reference curve. A matching PMI was expected to produce an isotherm curve identical to the reference isotherm curve from the decedent. In other words, a temperature difference curve between the two would be a zero straight-line curve. Fig. 9.10 indicates higher candidate PMI isotherm temperatures than the reference curve, which implied that 4hrs10mins was not a match.

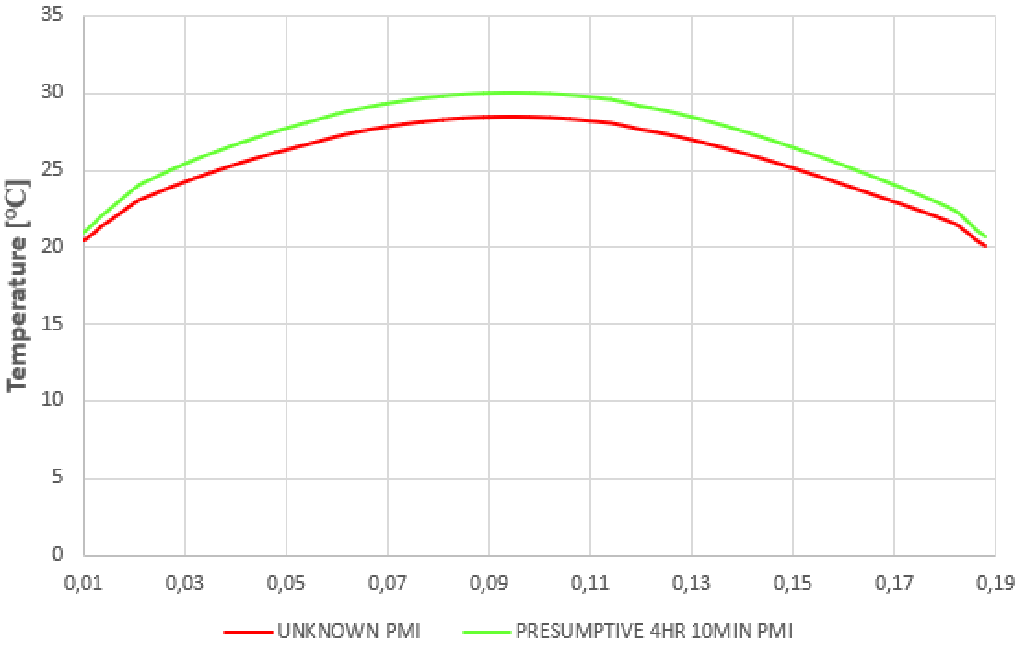

Fig. 9.10. The 4hr10min candidate PMI isotherm curve plotted with the reference curve from the unknown PMI.

9.4.1.2 Candidate PMI of 4hrs20mins

The candidate PMI of 4hrs20mins produced an isotherm curve whose temperatures were higher than the reference curve. This indicated that the target PMI was longer than 4hrs20mins but less than 5hrs and the protocol was continued to the next candidate PMI. Fig. 9.11 indicates the isotherm curve of this candidate PMI plotted with the reference curve.

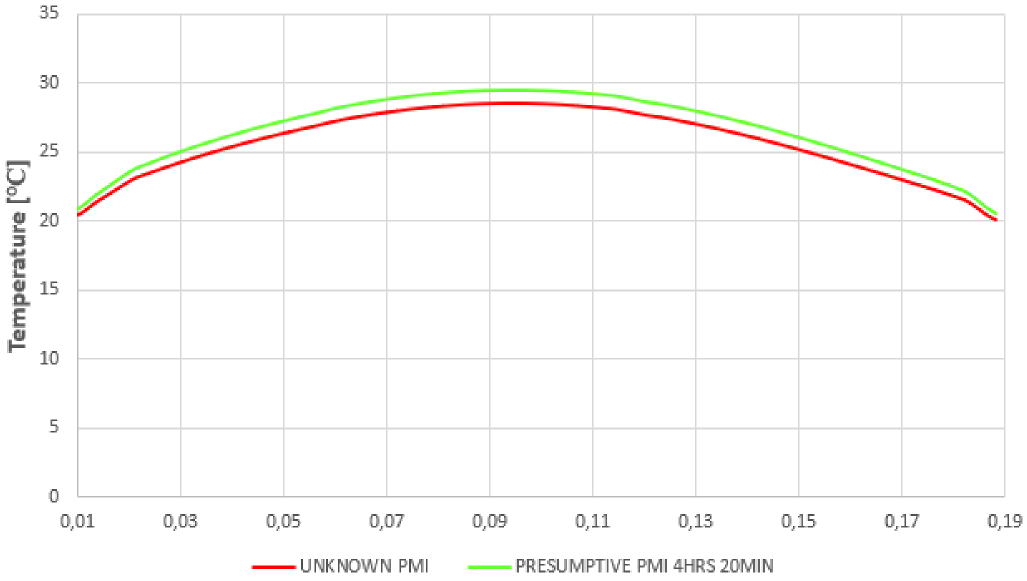

Fig. 9.11. The 4hr20min candidate PMI isotherm curve plotted with the reference curve from the unknown PMI.

9.4.1.3 Candidate PMI of 4hrs30mins

The candidate PMI of 4hrs30mins produced an isotherm curve whose temperatures were higher than the reference curve. This indicated that the target PMI was longer than 4hrs30mins but less than 5hrs and the protocol was continued to the next candidate PMI. Figs. 9.12 indicates the isotherm curve of this candidate PMI plotted with the reference curve.

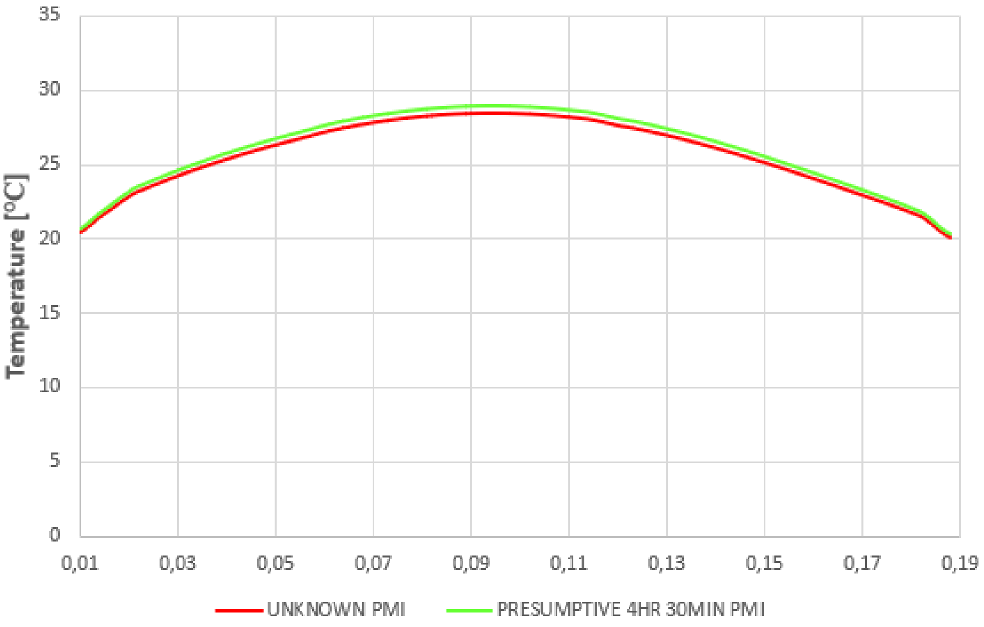

Fig. 9.12. The 4hr30min candidate PMI isotherm curve plotted with the reference curve from the unknown PMI.

9.4.1.4 Candidate PMI of 4hrs40mins

The candidate PMI of 4hrs40mins produced an isotherm curve whose temperatures were higher than the reference curve. This indicated that the target PMI was longer than 4hrs40mins but less than 5hrs and the protocol was continued to the next candidate PMI. Fig. 9.13A indicates the isotherm curve of this candidate PMI plotted with the reference curve. The two curves were almost identical, but the candidate curve showed higher temperatures than the reference. Fig. 9.13B indicates the temperature difference between the simulated and reference isotherm values.

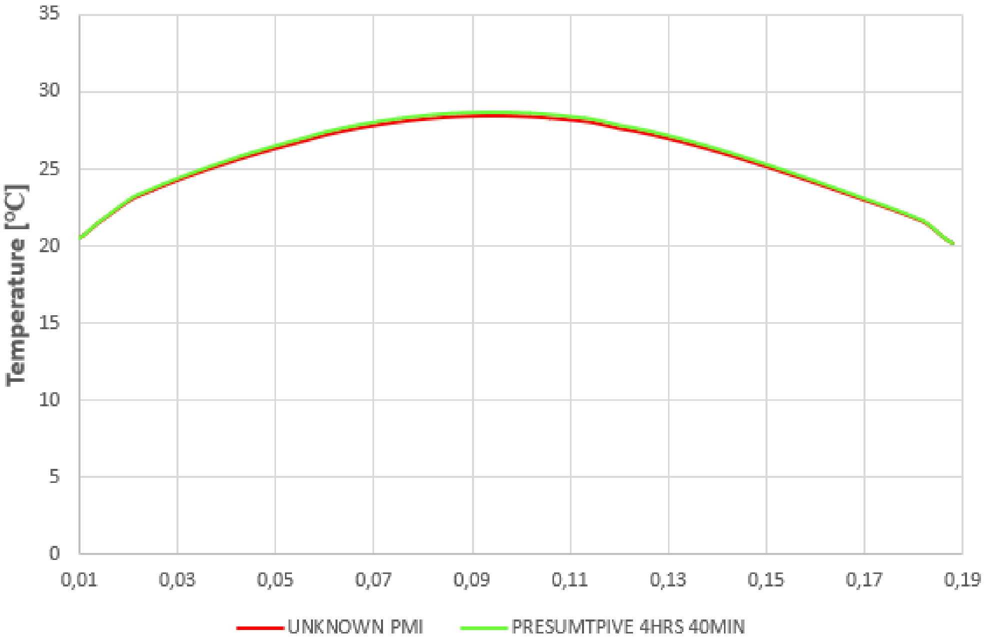

Fig. 9.13A. The 4hr40min candidate PMI isotherm curve plotted with the reference curve from the unknown PMI.

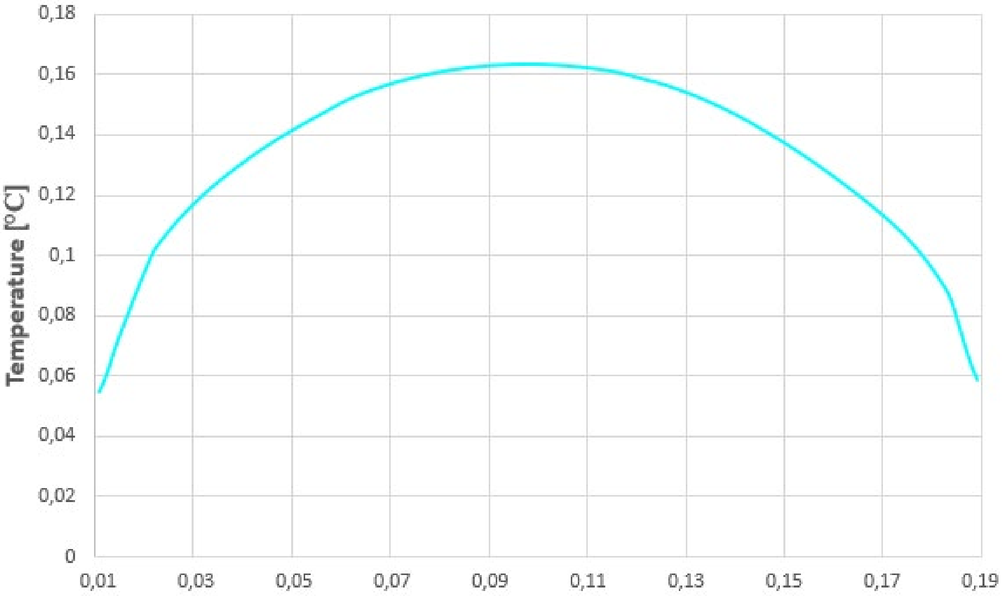

Fig. 9.13B. Divergence of the 4hr40min candidate PMI isotherm curve as indicated by the negative difference relative to the reference curve.

9.4.1.5 Candidate PMI of 4hrs50mins

The 4hr50min candidate PMI showed new divergence from the reference isotherm curve in which the candidate PMI isotherm temperatures were consistently lower than reference curve temperatures. This suggested that the matching candidate PMI was shorter than 4hr50min but longer than 4hr40min. Fig. 9.14A indicates the isotherm curve of the candidate 4hr50min PMI plotted with the reference curve. The two were almost but not quite identical, as the candidate PMI curve indicated lower temperatures than the reference isotherm curve. The difference between the two (candidate PMI temperatures subtracted from corresponding unknown PMI temperature) is plotted separately as a curve in Fig. 9.14B. It shows the temperature difference in the negative range, indicating divergence.

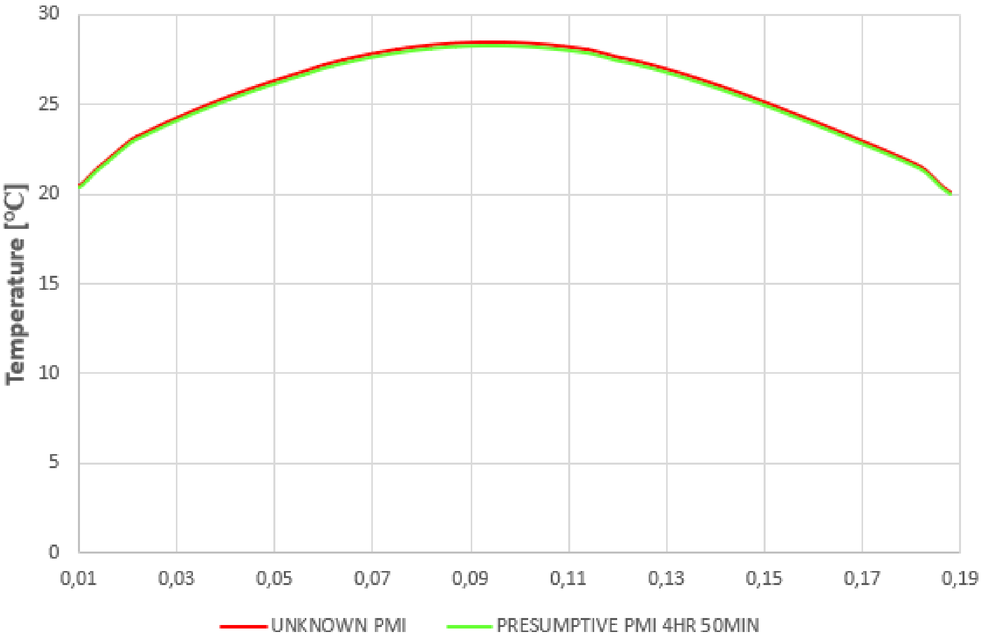

Fig. 9.14A. The 4hr50min candidate PMI isotherm curve indicating lower temperatures compared to the reference curve from the unknown PMI.

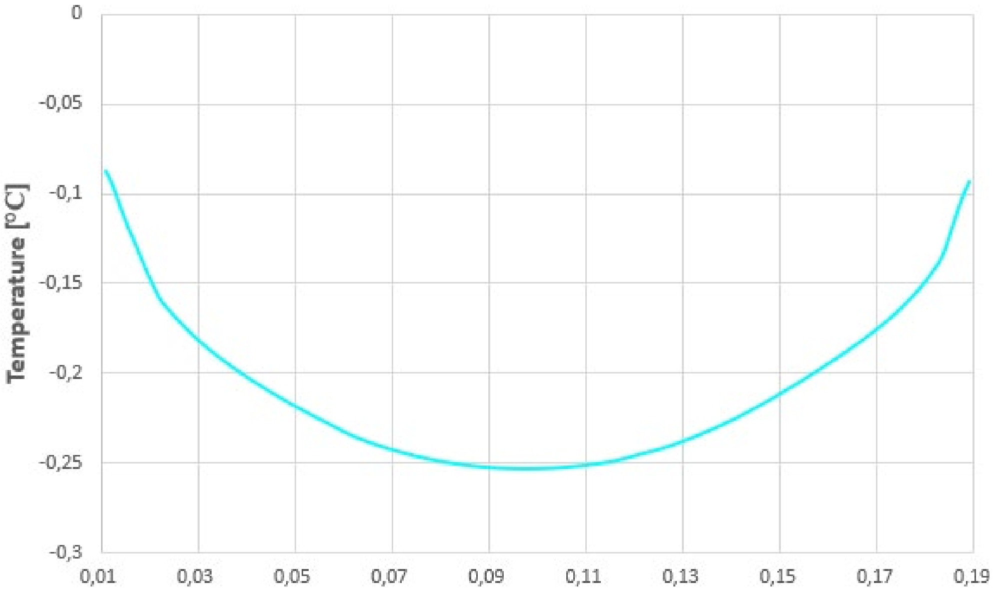

Fig. 9.14B. Divergence of the 4hr50min candidate PMI isotherm curve as indicated by the negative difference relative to the reference curve.

Because of the divergence, the added time increment was further reduced from 10 minutes to 2 minutes and the protocol was resumed from the 4hrs40mins candidate PMI to test candidate PMIs 4hr42mins, 4hr44mins, 4hr46mins, and 4hr48mins. Times of death, air temperatures at death and air temperatures during postmortem cooling intervals were established for each candidate PMI as described in the previous sections.

9.4.1.6 Candidate PMI of 4hrs42mins

The 4hrs42mins candidate PMI produced an isotherm curve whose temperatures were very slightly higher than the reference curve. This indicated that the target PMI was longer than 4hrs40mins but less than 4hrs50min, therefore the protocol was continued to the next candidate PMI. Figs. 9.15A indicates the isotherm curve of this candidate PMI plotted with the reference curve. The two curves are nearly identical, but have differences plotted as a curve in Fig. 9.15B.

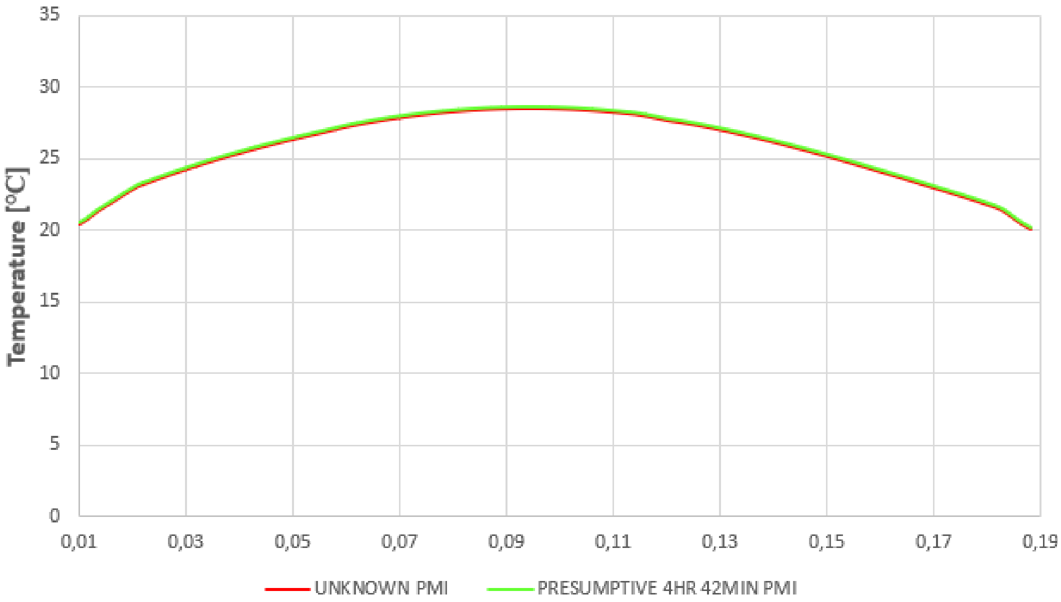

Fig. 9.15A. The 4hr42min candidate PMI isotherm curve plotted with the reference curve from the unknown PMI.

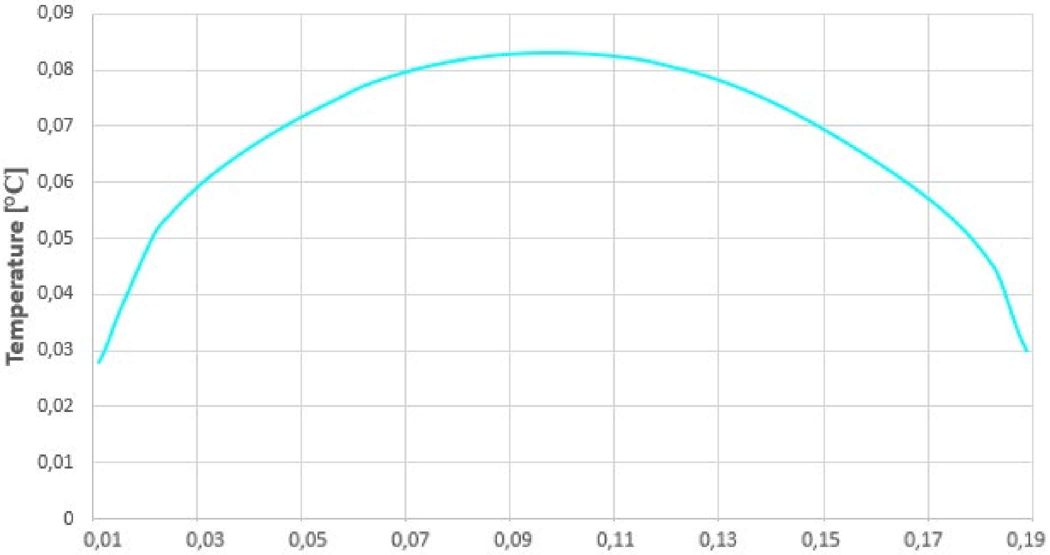

Fig. 9.15B. The magnified temperature difference curve between the 4hr42min candidate PMI isotherm curve and the reference curve from the unknown PMI.

9.4.1.7 Candidate PMI of 4hrs44min

The candidate PMI of 4hrs44min produced an isotherm curve that matched the reference isotherm curve exactly, with all corresponding curve temperatures matching to the fifth decimal, i.e. their difference was 0.00000°C. Fig. 9.16A indicates the isotherm curve of this candidate PMI plotted with the reference curve, while Fig. 9.16B indicates the plotted difference between the two curves. In the scenario provided, 4hrs44min would thus be regarded as the final PMI estimation determined by the MAT Protocol, making 06H49 on April 22nd 2018 the time and date of death. The protocol would therefore be terminated at this point. Table 9.3 summarises the proposed protocol used for the candidate PMI of 4hrs44min.

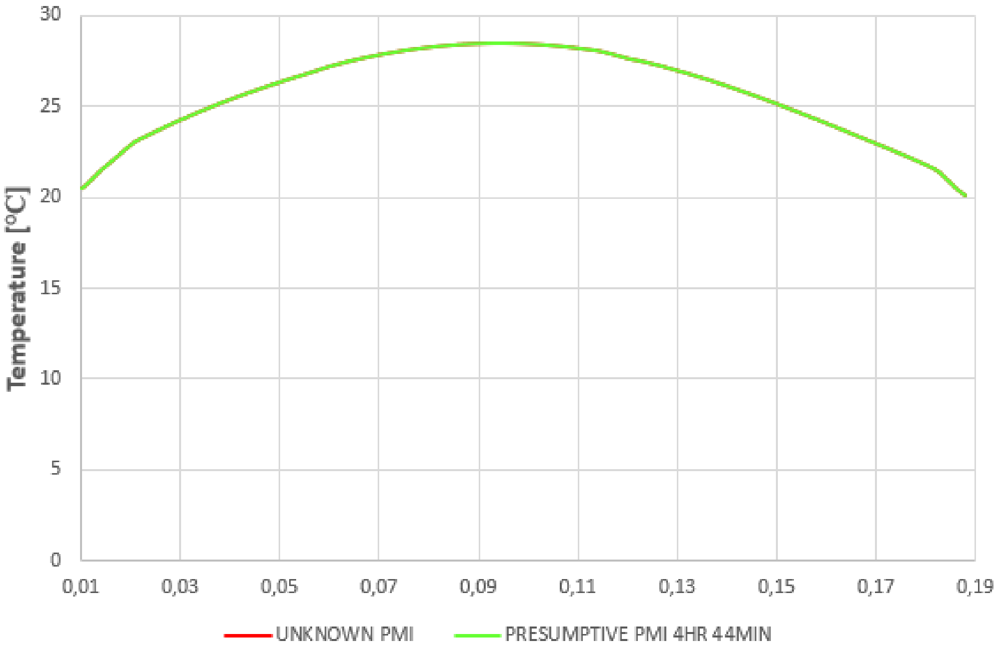

Fig. 9.16A. The matching 4hr44min candidate PMI isotherm curve plotted with the reference curve from the unknown PMI.

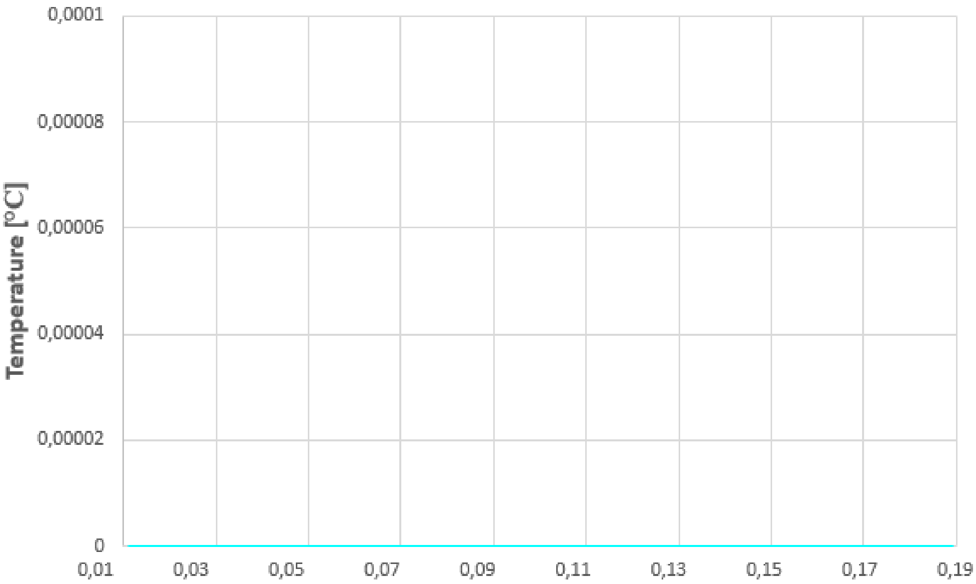

Fig. 9.16B. The magnified temperature difference curve between the 4hr44min candidate PMI isotherm curve and the reference curve from the unknown PMI.

Simulation Details	AM	PM 1	PM 2	PM 3	PM 4	PM 5	Isotherm measurement
Simulation interval	9000s	3600s	3600s	3600s	3600s	2160s	500s
Simulated period	Alive-06H49	06H49-07H49	07H49-08H49	08H49-09H49	09H49-10H49	10H49-11H25	11H25-11H33
Initial condition	37°C	AM	PM 1	PM 2	PM 3	PM 4	PM 5 for 3D human 15.1°C for virtual sensor
Boundary condition	7.761°C	8.311°C	9.701°C	11.345°C	12.995°C	14.358°C	14.988°C
Boundary type	mixed	mixed	mixed	mixed	mixed	mixed	mixed
Heat transfer coefficient [W/(m^{2}K)]	9.5	9.5	9.5	9.5	9.5	9.5	9.5
Grid cells (x10^7)	3.4595	3.4595	3.4595	3.4595	3.4595	3.4595	9.1563
Time to solution	28hrs	10hr4min	10hr36min	10hr4min	10hr36min	6hrs	5hrs34min

Table 9.3 Summary of the MAT Protocol used to test the 4hrs44min candidate PMI whose isotherm curve matched the reference curve. AM = antemortem simulation, PM = postmortem simulation.

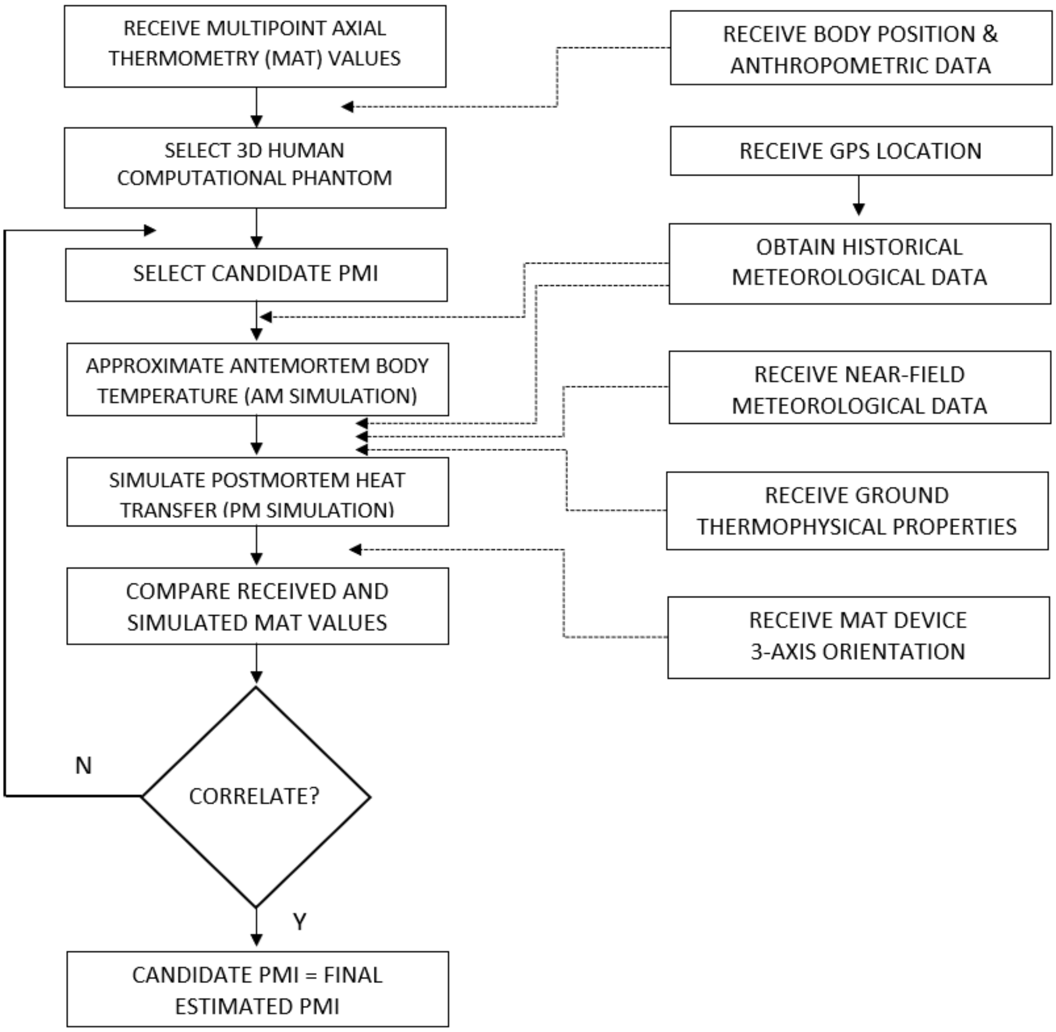

Fig. 9.17 A flow-diagram summarising general application of the MAT Protocol.

9.6 Discussion

9.6.1 Meteorological Data

A meteorological record of high temporal resolution, typically per minute, would evidently have been ideal to allow the MAT Protocol to simulate postmortem cooling from any arbitrary candidate TOD. In the absence of such a record, a simple interpolation technique had to be devised based on an assumption. Interpolation of climate data, especially over variable time intervals, is a complex science beyond the scope of this thesis[4]. In the end, the only data source to available to work with was the meteorological record provided, and the interpolation method was thought to have derived the most probable air temperature values that existed during postmortem cooling. Effects on skin of forced convective cooling by wind, meteorological condensation, solar radiation, and meteorological precipitation were omitted for the sake of simplifying the demonstration.

9.6.2 Iterative Comparison

One-hour increments applied at the beginning of the protocol were chosen arbitrarily, and an increment of any length may have been chosen. The obvious optimal increment length would be the correct PMI estimate, which would then negate further simulations and iterative comparisons. Divergence of the simulated from the reference isotherm curve signalled the need for reduction of the additive increment, after which iterative comparison had to be resumed. As the additive increment became smaller, so did the difference between simulated and reference MAT curves. The interval in which an isotherm match was likely to be found became shorter each cycle of additive increment reduction until only one candidate PMI produced a match. The data provided in the scenario could not be applied in any other simulation setup to produce a matching isotherm curve whose PMI was not 4hrs44min.

Accuracy of the final PMI estimate relative to the true PMI in the physical world would depend on the veracity of all pre-simulation data used in the MAT Protocol, as well as on the accuracy of numerical simulation materials and methodologies in representing the postmortem cooling conditions of a given case in the physical world. The PMI estimate demonstrated by the proposed protocol in the scenario is based upon the assumption that the temperature field of the body at death was equal to that simulated in the 3D phantom. The actual temperature field of a body at the time of death cannot be definitively known. Among others, this is a critical assumption that renders all thermometric PMI estimation methods circular. A priori knowledge of initial conditions, the solution being sought by AM simulations, are not known; they are therefore assumed. These factors, therefore, are the ones that constitute sources of uncertainty of the proposed protocol and are discussed separately in chapter 10.

9.7 Conclusions

9.7.1 The proposed MAT Protocol approximated antemortem temperature distribution of the entire body and did not use a single-point approximated ‘normal’ value. The protocol did not assume that the approximated antemortem body temperature was always the same under different ambient temperatures, as empiric methods do. Instead, antemortem body temperatures were approximated for each candidate PMI because air temperatures that existed as the respective candidate TODs differed. As suggested in chapter 6, the antemortem activity of each body may be approximated and antemortem body temperature distribution approximated using specific tissue parameters for metabolic heat generation and blood perfusion rates unique to it.

9.7.2 In ideal conditions the proposed protocol could eliminate all candidate PMIs, even those that were within the 3D computational phantom’s known PMTP of 3hr51min (chapter 7), something empiric methods are incapable of. The proposed protocol did not require the PMTP value of the body found dead to be solved for.

9.7.3 The proposed MAT Protocol applied historical meteorological record that existed only during the final estimated PMI and in the correct chronological sequence. It did not require a TOD estimate as a priori for averaging historical meteorological air temperatures thanks to its iterative testing and elimination of multiple candidate PMIs.

9.7.4 The proposed MAT Protocol was independent of uncertainty from thermometry-depth variation because the MAT automatically consisted of multiple simultaneous temperature measurements from multiple depths across the thigh.

9.7.5 The proposed protocol did not require an empiric method of death-time estimation for validation. In fact, comparison of the protocol's final PMI estimate against one that would have been estimated by, for example, the Henβge nomogram method was not possible without thermometry-depth of the simulated rectal temperature to make a comparison with being specified and justified over another thermometry-depth. Also, the nomogram method would have provided a range within which the PMI estimate may be, as demonstrated in chapter.

9.7.6 The effect of central isotherm shifting by ground surfaces was not applicable in the provided postmortem cooling scenario and was therefore not demonstrated. Nonetheless, the proposed protocol would have successfully reproduced the effect and avoided uncertainty of using a single-point core temperature measurement affected by the shift.

The MAT Protocol was therefore regarded as having fulfilled the core aims of this thesis set out in chapter 4.

Bibliography and References Cited

1. The Weather Underground

2. Weather History for Central Park, New York City, NY for Sunday, April 22, 2018. Weather Underground. The Weather Company, https://api.wunderground.com/history/airport/KNYC/2018/4/22/DailyHistory.html?req_city=New+York%2FCentral+Park&req_state=NY&req_statename=&reqdb.zip=10023&reqdb.magic=2&reqdb.wmo=99999

3. Totola NB, Shimpi MV, Shete NL, Bhopate VS (2013). Natural convection characteristics in vertical cylinder. International Journal of Engineering and Science; 3(8), 27-31.

4. Dyras I, Dobesch H, Grueter E, Perdigao A, Tveito OE, Thornes JE, van der Wel F, Bottai L (2005). The use of Geographic Information Systems in climatology and meteorology: COST 719. Meteorological Applications; 12, 1-5.

CHAPTER 10

Sources of uncertainty and limitations

Chapter 10

Sources of uncertainty and limitations

The proposed MAT Protocol is a complex method that involves measurement of new death scene parameters (body position, thermophysical properties of the ground), MAT, use of high-definition virtual 3D computational phantoms with multiplicity of organs, high temporal resolution historical meteorological data, multiple simulation-sequences that apply multiple parameters, and iterative comparative analysis. All these present potential sources of uncertainty that must be quantified to allow proposal of mitigating strategies. This chapter discusses known potential sources of uncertainty as far as could be discerned from studies in this thesis. The demonstration of the MAT Protocol in chapter 9 was intended only as an initial concept proposal and not a comprehensive critical analysis of the protocol.

The choice of materials and methods with which the MAT Protocol will be applied in the future may differ from those used in this thesis. For example, one may wish to use 3D computational phantoms built from CT scans, and/or that have a lower (or higher) resolution, and/or that have a lower (or higher) number of organ-segmentation than those used in this thesis; one may choose to use the finite-element method instead of the finite-difference time-domain method; and one may use a thermal solver other than Sim4Life®. Each combination will be characterised by a unique set of uncertainties, while other sources of uncertainty were not immediately obvious at the time of writing of this thesis but may become obvious in the future. The following were potential sources of uncertainty of the MAT Protocol that could be predicted as informed by experience gained in this thesis.

10.1 Anthropometric incomparability of a selected 3D computational phantom

As diverse as the Virtual Family 3D computational human phantoms may be, they are not representative of every corpse. Variations in normal anatomy and anthropometric parameters among the general population will be a source of uncertainty. The correlation between PMTP length and circumference of a body part/limb demonstrated in this thesis means that anthropometric discrepancies between a decedent’s body and the 3D computational phantom selected for the MAT Protocol would result in an incorrect PMI estimation. An error analysis of this variable was precluded by time constraints required in the executing the MAT Protocol.

10.2 Approximation of antemortem body temperature during physical exertion

Numerical approximation of antemortem body temperature performed in this thesis applied mean values of biothermal parameters. In the living human body these parameters fluctuate through a wide range as a result of physical activity, environment-related thermoregulation, emotional state, and pathology states. Postmortem cooling preceded by intense physical exertion will proceed differently from postmortem cooling after death during peaceful sleep. Inaccurate representation of physical exertion of a given body in the AM simulation may lead to inaccurate approximation of antemortem body temperature, and hence uncertainty of the PMI estimated by the MAT Protocol. An error analysis of approximation of antemortem body temperature during physical exertion was precluded by time constraints required in the executing the MAT Protocol.

10.3 Absence of thermoregulatory mechanism in 3D computational phantoms

The AM simulation used in the MAT Protocol did not have a thermoregulation mechanism to mimic sweating, vasodilatation, vasoconstriction and shivering normally used by the body to maintain core temperature within a narrow range. Blood flow, as far as it distributes heat around the body, was not explicitly solved for velocity and temperature, which probably resulted in low predicted cardiac blood temperatures observed in chapter 7. Some bioheat models used in human thermal comfort in the built environment, e.g. by Stolwijk[1], Fiala et al[2] and Huizenga et al[3], do model thermoregulation. However, internal anatomical fidelity of their 3D computational phantoms is generally low and does not meet the requirements of the MAT Protocol. An error analysis of this variable was precluded by non-availability of modelling thermoregulation methods in this thesis.

10.4 The heat transfer coefficient value used

The heat transfer coefficient value applied to the boundary condition should be that of the specific posture of the body recorded at the death scene[4]. This thesis determined that the heat transfer value applied influences how parabolic the MAT curve is. Higher heat transfer coefficient values created more parabolic MAT curves. Postmortem cooling may not always occur in natural / unforced convective conditions. Forced convective cooling by wind would require higher heat transfer coefficient values to be used. Use of an inappropriate heat transfer coefficient value may lead to under- or overestimation of heat transfer on the 3D computational phantom's skin, and thus uncertainty of the MAT Protocol. An error analysis of this variable was precluded by time constraints required in the executing the protocol.

10.5 Tissue thermophysical and biophysical values

Difference between a decedent body's true tissue parameters and those assigned to the selected 3D computational phantom is a source of uncertainty inherent to numerical analysis of postmortem cooling. Weiser et al[5] discussed uncertainty of death-time estimation arising from variations in tissue material parameters that presumably remain constant in life and during postmortem cooling. This thesis applied additional new biothermal tissue parameters that vary significantly in life depending on a number of factors, to approximate antemortem body temperature distribution. Application of biothermal parameters that do not correspond to those that existed in a decedent's body in life when approximating antemortem body temperature distribution may constitute a source of uncertainty in the PMI estimated by the MAT Protocol.

This thesis proposes that the pathologist who wishes to apply the MAT Protocol should first visit the death scene and make an approximation of the activity a decedent was undertaking immediately before death. The metabolic equivalent rate of that activity should be referenced from the literature[6] and proportionately applied to the 3D phantom's organs according to the degree of their metabolic involvement in the approximated antemortem activity.

An error analysis of variation in organ metabolic heat generation and blood perfusion rates on approximated body temperature at death was precluded by time constraints required in the executing the MAT Protocol.

10.6 Grid size

The size and spacing of the grid affect the simulation solution. Increasing the number of elements in a computational geometry is advisable until a mesh independent solution is achieved[7,8]. The commercial thermal solver of Sim4Life® used in this thesis was designed to be automatically mesh-independent when used with the ViP 3D computational phantoms[9], therefore the effect of a mesh dependent solution could not be demonstrated and its error margin could not be analysed in this thesis. Mesh-independence would need to be demonstrated by any numerical analysis scheme applying the MAT Protocol.

10.7 Historical meteorological record

A continuous (second-by-second) historical meteorological record would be ideal for application in the MAT Protocol, to avoid errors associated with the mathematical operations used to interpolate minute-to-minute air temperatures from the record. Distance of the death-scene from a weather station whose data is used in the MAT Protocol, plus the potential difference with the local microclimate around the dead body are potential sources of uncertainty.

10.8 Differences in multipoint thermometry device 3-axis orientation

The physical and virtual MAT devices used in the MAT Protocol must have identical 3-axis orientation, otherwise any differences will result in non-comparability of the respective MAT curves. A MAT device inserted into the body at an angle other than 90° to the skin would not pass through the central isotherm and would therefore have a lower maximum temperature value and thus a non-representative shape. An error analysis of this variable was precluded by time constraints required in the executing the MAT Protocol.

10.9 The multipoint thermometry device instrument error

Instrument error of a MAT device needs to be known. Instrument error analysis methods[10] in health sciences have been proposed by authors. The MAT device and its sensors need to have been validated, verified, and calibrated before thermometry. The MAT computational model must be identical to the physical device in geometry and material properties, otherwise small differences may be a source of uncertainty. An error analysis of this variable was precluded by non-availability of an alternative MAT device with which to perform MAT.

10.10 Thermophysical properties of the ground-surface

Thermophysical properties of the ground-surface applied in the MAT Protocol needs to be verified. Temperature of the ground surface may be assumed to be at equilibrium with prevailing ambient air temperature. Failure to correctly model the ground surface or to assign correct material properties may result in uncertainty depending on difference magnitude with the physical world. As an example, Table 10.1 indicates material properties[11,12,13,14,15,16] of wood and stainless-steel, two common ground-surfaces on which postmortem cooling occurs. The differences would obviously affect the rate of postmortem cooling by thermal conduction. An error analysis of using incorrect surface thermophysical parameters, incorrect surface temperature or non-modelling of the ground-surface was precluded by time constraints required in the executing the MAT Protocol.

Material	Density (kg/m^3)	Thermal conductivity [W/(mK)]	Specific heat capacity (J/kg C°)
Wood	850	0.147	1850
Stainless- steel	8000	14.4	490

Table 10.1 indicating material properties for wood and stainless-steel.

10.11 General human errors during data-handling

Although many functions of Sim4Life® and P-Thermal® were automated, the MAT Protocol consisted of multiple iterations that involved thousands of manual steps, which required impeccable operator concentration. The potential for uncertainty resulting from human-error existed, which must be mitigated. The MAT Protocol can be programmed to operate as a computer software application, which is regarded as a cognitive product[17,18]. Human error is regarded as a primary cause of software defects, and human error analysis is a field that plays a key role in the understanding and prevention of software defects. Human error analysis methods in software engineering have been proposed [19] by authors. Automation of the MAT Protocol within the numerical analysis software was possible via the software's scripting function using PYTHON coding language.

10.12 Length of PM simulations

The correct simulation interval of a postmortem simulation in the MAT Protocol ensures representative exposure of the 3D computational phantom to the appropriate air temperature over the correct time interval consistent with actual postmortem cooling conditions. Availability of higher resolution historical meteorological data would enable shorter postmortem interval simulations without increasing the overall computational time. The increased number of simulations carries the risk of increased human error.

Bibliography and References Cited

1. Stolwijk JAJ (1970). A Mathematical model of physiological temperature regulation in Man. NASA Report.

2. Fiala D, Lomas KJ, Stohrer M (1999). A computer model of human thermoregulation for a wide range of environmental conditions: the passive system. Journal of Applied Physiology 87(5):1957-1972.

3. Huizenga C, Hui Z, Arens E (2001). A model of human physiology and comfort for assessing complex thermal environments. Building and Environment 36, 691-699.

4. de Dear R, Arens E, Zhang H, & et al. (1997). Convective and radiative heat transfer coefficients for individual human body segments. Int. J. Biometeorol.,141-156.

5. Weiser M, Erdmann B, Schenkl S, Muggenthaler H, Hubig M, Mall G, Zachow S (2017). Uncertainty in temperature-based determination of time of death. Heat and Mass Transfer, 2815-2826.

6. Jette M, Blümchen G (1990). Metabolic Equivalents (METS) in Exercise Testing, Exercise Prescription, and Evaluation of Functional Capacity. Clin. Cardiol. 13, 555-565.

7. Sørensen, DN, Nielsen PV (2003). Quality control of computational fluid dynamics in indoor environments. Indoor Air 13, 2-17.

8. Wang, H, Zhai Z (2012). Analyzing grid independency and numerical viscosity of computational fluid dynamics for indoor environment applications. Building

---

and Environment 52, 107-118.

9. Szolnoki L, Neufeld E, Kuster N (2018). Foundation for Research on Information Technologies in Society. Sim4Life and SEMCAD Thermal Solver (Verification Report TS002AA201812).

10. Chatburn EL (1996). Evaluation of instrument error and method agreement. Journal of the Aermican Association of Nurse Anesthetists, 64(3), 261-268.

11. Engineering ToolBox, (2005). *Thermal Conductivity of Metals, Metallic Elements and Alloys*. [online] Available at: https://www.engineeringtoolbox.com/thermal-conductivity-metals-d_858.html [Accessed 21 October 2020].

12. Engineering ToolBox, (2003). *Thermal Conductivity of selected Materials and Gases*. [online] Available at: https://www.engineeringtoolbox.com/thermal-conductivity-d_429.html [Accessed 21 October 2020].

13. Engineering ToolBox, (2003). *Specific Heat of some common Substances*. [online] Available at: https://www.engineeringtoolbox.com/specific-heat-capacity-d_391.html [Accessed 21 October 2020].

14. Engineering ToolBox, (2003). *Specific Heat of some Metals*. [online] Available at: https://www.engineeringtoolbox.com/specific-heat-metals-d_152.html [Accessed 21 October 2020].

15. Engineering ToolBox, (2004). *Density of Various Wood Species*. [online] Available at: https://www.engineeringtoolbox.com/wood-density-d_40.html [Accessed 21 October 2020].

---

16. Engineering ToolBox, (2004). *Metals and Alloys - Densities*. [online] Available at: https://www.engineeringtoolbox.com/metal-alloys-densities-d_50.html [Accessed 21 October 2020].

17. Détienne F (2002). Software Design–Cognitive Aspects. New York, NY: Springer-Verlag New York, Inc.

18. Huang F, Liu B, Huang B (2012). A Taxonomy System to Identify Human Error Causes for Software Defects. In: The 18th International Conference on Reliability and Quality In Design, Boston, USA, 44-49.

19. Huang F (2017). Human error analysis in software engineering, Theory and Application on Cognitive Factors and Risk Management – New Trends and Procedures, Fabio De Felice and Antonella Petrillo, IntechOpen, DOI: 10.5772/intechopen.68392. Available from: https://www.intechopen.com/books/theory-and-application-on-cognitive-factors-and-risk-management-new-trends-and-procedures/human-error-analysis-in-software-engineering.

CHAPTER 11

Summary and conclusions

Chapter 11

Summary and conclusions

This thesis represents a continuum of work by the author to contribute in improving accuracy of death-time estimation. This chapter discusses summary and conclusions reached in the course of the thesis, as well as future implications of the proposed MAT Protocol and proposed MAT device for the science of death-time estimation.

11.1 Summary and conclusions

11.1.1 Application of a single-point approximation of antemortem body temperature used by empiric methods of death-time estimation today misrepresents total-body temperature and result in uncertainty of death-time estimation.

11.1.2 Numerical simulation offers more realistic approximation of antemortem body temperature distribution compared to a single-point approximation.

11.1.3 Application of 3D computational phantoms that have high anatomical fidelity offers more realistic representation of the human body and representative numerical approximation of body temperature at death.

11.1.4 Application of metabolic and blood perfusion rates to organs of a 3D computational phantom is proposed for numerical approximation of antemortem body temperature distribution.

11.1.5 Future work on approximation of antemortem body temperature distribution could incorporate thermoregulation and approximation of antemortem activity.

11.1.6 The thesis proposes separation of approximation of antemortem body temperature distribution from numerical simulation of postmortem cooling.

11.1.7 A single-point postmortem core temperature measurement as required by empiric methods of death-time estimation detects the temperature of the central isotherm, which is not PMI specific.

11.1.8 The PMTP is the central isotherm that exists in life. It can be demonstrated without simulating supravital heat production in the intermediary stages of life. The PMTP is an unfortunate manifestation of single-point thermometry.

11.1.9 The postmortem location of the central isotherm is influenced by temperature and thermophysical properties of the ground-surface of postmortem cooling.

11.1.10 A ground-surface of postmortem cooling may not always be an infinite heat-sink because heat transfer with it results in its temperature change, which affects subsequent heat transfer rates of the body.

11.1.11 Postmortem heat transfer occurs from the body to a heated floor of 25°C in the early PMI.

11.1.12 Postmortem single-point core thermometry requires standardisation of relative thermometry-depth, otherwise thermometry-depth variations are a source of uncertainty.

11.1.13 The postmortem axial thermal profile of the body may be specific for the PMI at which it is measured.

11.1.14 MAT measures the axial thermal profile of a body and eliminates uncertainties of single-point thermometry in death-time estimation discussed in this thesis.

11.1.15 MAT is possible using the proposed MAT device.

11.1.16 The MAT curve from a cooling body (torso or limb) has a parabolic shape.

11.1.17 The proposed MAT Protocol avoids pitfalls of single-point thermometry by iteratively comparing the MAT profile from a dead body against the simulated MAT profiles from numerical simulations of increasingly longer candidate PMIs, whereupon the simulated candidate PMI that produces a matching MAT profile is considered the final PMI estimate.

11.1.18 The proposed MAT Protocol applies high-fidelity 3D computational phantoms whose anthropometric parameters approximate those of a dead body.

11.1.19 The proposed MAT Protocol approximates antemortem body temperature on 3D computational phantoms.

11.1.20 The proposed MAT Protocol models ground-surfaces using material properties according to death-scene observations.

11.1.21 MAT in the proposed MAT Protocol ensures that effects of modelled ground-surface on the position of the central isotherm are detected.

11.1.22 The proposed applies exact historical meteorological air temperature that existed during the final estimated PMI, and in the correct chronological sequence without requiring the TOD as a priori.

11.1.23 Data, materials, and methods used in the application of the proposed MAT Protocol collectively constitute sources of uncertainty of the protocol.

11.1.24 The proposed MAT Protocol and proposed MAT device have the potential to extend numerical thanatochronometry beyond the state-of-the-art through their continued refinement and extended application.

11.2 Implication for the science of death-time estimation

By reducing of single-point thermometry uncertainties, the MAT Protocol extends the scope of numerical death-time estimation and builds on the work of previously mentioned authors in this field. The scope of future research opportunities inspired by it, many of which have already been mentioned in the thesis, is vast. This chapter presents a few of such opportunities, which the authors regards as priority research areas.

11.2.1 Non-invasive full-body postmortem thermometry

Non-invasive postmortem thermometry methods are always attractive because a) they do not require the medical examiner at the death scene to carry any surgical instruments or sharps-containers, b) they do not cause postmortem artefacts in the body that may present difficulties with interpretation of autopsy findings later at the mortuary, c) family members find them more appealing as they result in less postmortem incisions on the body of their loved ones. Non-invasive postmortem thermometry is a concept attempted by Al-Alousi and Anderson[1,2] with mixed results, which the author thinks were due to shallow/variable thermometry-depth of their microwave method. Magnetic resonance thermal imaging (MRtI)[3] has the ability to measure temperature of a desired organ during MRI scanning and is a promising tool for performing total-body postmortem thermometry for application in the MAT Protocol.

However, an MRtI scanner is a large, immobile, specialised piece of equipment for use in strictly regulated environments, usually a specialist medical facility. The decedent’s body would either have to be transported to the medical facility, or the MRtI unit would have to be brought to the death-scene in a suitable vehicle, e.g. a truck. A more compact and portable version that could be carried by one or two people and that could be placed directly over the decedent’s body without disturbing it would be ideal. The non-invasive method of death-time estimation by Wilk et al[4] is limited to surface skin temperature and does not address internal axial isotherm measurement.

11.2.2 Death-scene 3D scanning and reconstruction

3D scanning of a death scene would assist with high-fidelity virtual reconstruction and modelling of the postmortem cooling environment for application in the MAT Protocol. Precise geometric shapes, physical dimensions and relative distances of all objects involved in the postmortem heat transfer process can be documented by 3D scanning. In particular, this tool would enable documentation of:

- Body position (prone, supine, lateral),
- Body posture (joint angle and joint rotation),
- Body anthropometry, allowing for more realistic selection and representative posing of a 3D computational phantom.
- Ground-surface texture, e.g. rough asphalt vs smooth ceramic tile, thereby allowing high-fidelity modelling.
- Body coverings, e.g. clothing or bedding, along with their natural folds and creases, allowing their high-fidelity modelling.
- Nearby sources of thermal radiation, e.g. convection heaters and air-conditioning units, and their distances from the body.

Handheld and tripod-mounted 3D scanning techniques are described for application in a number of forensic investigations, e.g. virtual crime scene reconstruction[5,6,7,8].

11.2.3 Numerical modelling of clothing

Clothing and coverings obviously play a significant role as insulators of heat transfer from the body, and by accelerating heat transfer from the skin when wet/moist. While empiric methods of death-time estimation such as the Henβge Rectal Temperature Nomogram method[9] apply corrective factors for clothing, current numerical methods have to simulate clothing on top of 3D computational phantoms. However, such modelling is still simplistic and of low 3D realism[10,11]. More realistic[12] and robust[13] methods of simulating clothing are described in the literature and would enable more representative numerical modelling of the body, especially when used along high resolution death scene 3D scan data of folds, creases, fabric weave pattern and fabric thickness as a guide. Wetness, moisture and water/water-vapour permeability[12] are additional physical characteristic of clothing that affect heat transfer from the skin, which would require numerical simulation.

11.2.4 Numerical simulation of airflow using CFD

Numerical simulations conducted in this thesis were for so-called unforced/natural convection in which the driving force is gravity, and air flow velocity on the skin is assumed to be negligible. However, airflow of wind results in forced/assisted convection. The Henβge rectal temperature nomogram method[9] applies corrective factors to address the effect of air flow affecting postmortem cooling. As it is, the nomogram method is unable to apply windspeed measurements that are usually part of the historical meteorological record. To date there is no record of a numerical method of death-time estimation that applies CFD to simulate natural or forced-convective airflow. The study by Wilk et al[4] did not explicitly state how they simulated airflow on their 3D computational phantom. CFD simulation of airflow on a 3D computational phantom during simulated postmortem cooling requires coupling of the CFD software with the thermal solver modelling heat transfer in the 3D computational phantom[14]. The method of modelling clothing by Barry and Hill[12] was coupled with CFD and allowed simulation of air flow over simulated clothing to illustrate its effect on the body. Modelling airflow during postmortem cooling using CFD would thus extend application of the historical meteorological record as described in the MAT Protocol.

11.2.5 Wind-speed-adjusted heat transfer coefficients

In the absence of CFD, the forced convection heat transfer coefficient in air for air velocities from 2 ms^{-1} to 20 ms^{-1} can be calculated using the empirical equation[15]:

$$h_c = 12.12 - 1.16v + 11.6v^{1/2} \tag{11.1}$$

where h_c is the heat transfer coefficient (W/m^2°C), v is the relative speed between the object surface (the decedent's body) and air (ms^{-1}). Using Eqn. (11.1) would allow calculation of heat transfer coefficients to be applied in the MAT Protocol using wind speed measurements from the meteorological record.

11.2.6 Improved anatomical fidelity of 3D computational phantoms to decedents

Any preselected 3D computational phantoms from the Virtual Population used in the MAT Protocol will almost certainly differ in anatomical exactness to a given decedent's body due to natural variability. This is true even for the human subjects whose bodies were originally scanned to create the phantoms because of ageing-related changes since MRI scanning. Therefore, a method of creating 'bespoke' 3D computational phantoms from MRI scans of a decedent's own body using ultra-rapid anatomical segmentation algorithms similar to those used by Gosselin et al[16] in developing the Virtual Population phantoms would ensure anatomical consistency and true anatomical difelity of the 3D computational phantom. The MRtI scanning technique suggested earlier for total-body thermometry is the obvious candidate for this purpose.

11.2.7 Reduction of the PROPOSED Protocol computational time

The MAT Protocol demonstration reported in chapter 10 took 94 days of continuous 24-hour-a-day simulation. Approximation of the antemortem temperature distribution in AM simulations had to be performed for every candidate PMI and each took ±27 hours to complete. This was because the ambient temperature that existed at the assumed TOD was different for each candidate PMI, which affected the approximated antemortem body temperature distribution. Thereafter, each hour of simulated postmortem cooling in the PM simulations took ±7 hours. These lengths of time were mainly due to the number of cells in a grid, which primarily depended on physical dimensions of the 3D computational phantom and on grid resolution. As stated in chapter 5, the grid resolution used in this thesis was so-called ‘normal’. The two higher grid resolution options (‘fine’ and ‘very fine’) that were optional would have increased the computational time even more. A total of 14 candidate PMIs were tested by the time the matching candidate PMI of 4hrs44mins was encountered. The commercial thermal solver used in this thesis did not support parallelisation and therefore only one instance of it could be run in one computer at a time (licensing agreement conditions). This meant that simulations for candidate PMIs had to wait their turn in thermal solver queue.

One solution to reduce the MAT Protocol computational time would be to use multiple computer platforms and multiple thermal solver licenses, in which each platform is assigned one candidate PMI to solve. Even so, the computational time would be at least be ±27 hours long because of mandatory approximation of antemortem body temperature for each candidate PMI. A solution to reduce this computational time is obviously required if the protocol is to be practicable in real-world death-time estimations. It is therefore apparent that more work is required to create faster algorithms or to allow parallelization.

11.2.8 Historical air temperature from geothermal satellite imagery in the MAT Protocol

The National Aeronautics and Space Administration (NASA)'s Goddard Institute for Space Studies (GISS) run the GISS Surface Temperature Analysis programme (GISTEMP v4) that estimates global surface temperature change using data files from land-based meteorological weather stations and ocean-based data[17]. The data are combined as described by Hansen et al[18] and Lenssen et al[19]. GISTEMP v4 is a potential source of GPS-specific historical meteorological data to be applied in the MAT Protocol for remote death-scenes that are far from weather stations. Another potential source of GPS-specific historical meteorological data is the National Oceanic and Atmospheric Administration (NOAA)'s National Centres of Environmental Information (NCEI).

11.2.9 Expeditious verification of a decedent’s tissue parameters

As pointed out by Weiser et al[20], variation in tissue parameters (density, thermal conductivity, specific heat capacity) is a source of uncertainty in numerical methods of death-time estimation. Applied values used in this thesis were sourced from the literature and may differ from those of the decedent’s body. Access to a body’s internal organs as an opportunity to experimentally verify tissue parameters may arise not at the death-scene but at the mortuary once the body is removed. A minimally-invasive percutaneous technique for expeditious verification of tissue parameters at the death-scene is a potential research area that would assist in mitigating this uncertainty.

11.2.10 CFD simulation of heat transfer by blood flow in blood vessels

CFD has application in a number of medical sciences, particularly cardiovascular medicine, to simulate intravascular blood flow in the living patient. It is used for modelling disease processes for improving clinical diagnostics, designing optimised implantable prosthetic devices, and improving outcomes of surgical procedures[21]. In the MAT Protocol, coupling CFD with heat transfer modelling would be used to simulate heat distribution throughout the living body via the arterial and venous systems, heat exchange between the vascular and tissue compartments and heat exchange in artery-vein coupled blood vessels. CFD may also be coupled with thermoregulation models to enhance them. CFD application would solve for blood temperature intrinsically, improving on the Pennes bioheat model[22] in which the blood temperature value has to be stated by the operator of the model. Certainty of CFD solutions would be improved when the 3D computational phantom used was built from MRI scans of the decedent, as suggested in 11.2.6 above.

11.2.11 Automation of the MAT Protocol

Advantages that automation of the MAT Protocol would offer towards reducing human error and computational time have already been elaborated upon in the previous subsections.

11.2.12 Simplification of the MAT Protocol using one PM simulation and an averaged air temperature value

The current proposed format of the MAT Protocol entails multiple PM simulations that are1 hour long. Longer or shorter periods can be simulated. However, simulation of longer periods entails use of averaged air temperature values for that period, and one PM simulation would require averaged air temperature, the very practice avoided by the MAT Protocol. Use of one versus multiple PM simulations would have no bearing on the final simulation time but is technically easier and involves fewer operational steps and potential sources of human error. A study to evaluate the pros and cons of a single PM simulation in the protocol is required.

11.2.13 Simulation of putrefactive decomposition using the MAT Protocol

Currently, the proposed application of the MAT Protocol is limited to the early PMI in which heat transfer occurs. However, the protocol's scope can be extended to include the late PMI in which changes such as putrefaction, mummification and adipocerification occur. Putrefaction involves tissue breakdown by autolysis and bacterial action and is characterised by distinct patterns of bodily changes, e.g. bloating, blister formation, skin slippage, green/black skin discolouration, and marbling of subcutaneous veins[23]. All these changes are caused by postmortem biochemical reactions that, in turn, are moisture and temperature-dependent and may be numerically simulated to reproduce the distinct patterns.

Computational biochemistry methods may be used to numerically predict putrefactive changes occurring in the 3D computational phantom. Computational biochemistry is a broad scientific area of research that uses computation to get insight on biological molecules and their many interactions[24]. These include proteins, carbohydrates, nucleic acids, lipids, and other mediators essential for cellular activity (including small compounds, metabolites, and cofactors)[24]. Computational biochemistry encompasses the structural and functional characterization of biosystems at the molecular level[24]. This is often performed by employing different physical approaches, ranging from classical molecular mechanics to quantum mechanics[24]. In a fashion similar to MAT comparison, postmortem changes recorded on a decedent's body may be correlated with changes numerically simulated by computational biochemistry using the MAT Protocol.

11.2.14 Death-scene infrared thermography

Infrared thermography (thermal imaging) systems detect infrared radiation and covert it to an image, similar to a common camera that forms an image using visible light[25]. Infrared thermography has a wide range of applications, including crime scene documentation[25,26]. In the context of the MAT Protocol, infrared thermography would assist in 1) the evaluation, documentation and quantification of near-field sources of thermal radiation affecting postmortem cooling, 2) evaluation, documentation and quantification of skin/clothing temperature, 3) detection of the original body location and posture if postmortem tempering and repositioning occurred within a reasonable time prior to thermography, and 4) the evaluation, documentation and quantification of ground-surface temperature, e.g. heated floor, to facilitate numerical modelling. Modelling a crime scene in 3D, as suggested in 11.2.2 above, and adding infrared thermal information, as demonstrated by Van Iersel et al[26], would form the dataset on which comparisons of the MAT Protocol's simulations are made.

11.2.15 Modelling sources of strong indoor thermal radiation and heat sink

As stated in 11.2.14 above, infrared thermography can document thermal intensity from indoor sources of thermal radiation in proximity to the body. Such sources need to be modelled accurately in the simulation environment so that their effect on the 3D computational phantom can be accurately represented. The dimensions, make, model, power rating and power setting of an electric thermal radiation source would need to be documented for accurate modelling. In addition to detecting sources of strong thermal radiation, infrared thermography can also detect strong thermal sinks not immediately appreciated by the naked eye, such as ground ice or snow under the dead body that could be colder than ambient air temperature.

11.2.16 Modelling effects of natural solar radiation, shades, and cloud cover

Solar thermal radiation affects the rate of postmortem cooling by increasing skin/clothing temperature. The amount of solar thermal radiation absorbed by a body after death depends on a number of factors, including the body's orientation on the ground relative to the north pole, earth's distance from the sun (due to season), hours of sunshine (due to season), time of day, amount of cloud cover, shade and shadows of nearby tall objects or landscape, additional reflected solar radiation, the colour of clothes, and atmospheric clarity. The discrete-ordinates method by Chandrasekhar[27] is used to approximately solve the radiative transfer equation (a five-dimensional integro-differential equation with three spatial and two directional coordinates)[28] by discretizing both the *xyz*-domain and angular variables that specify the direction of radiation. The discrete-ordinate method is commonly applied in several physics and engineering numerical simulation programs, e.g. COMSOL Multiphysics[29]. Simulation of postmortem solar radiation in the MAT Protocol is a potential research topic that would be beneficial for death-time estimation.

11.2.17 Simulation of flowing liquid using CFD in submersion deaths

Simulation of convective cooling on a body fully/partially submerged in a flowing body of water is possible when CFD is coupled with a thermal solver. The Henβge rectal temperature nomogram method applies corrective factors for correction of fluid flow.

11.2.18 Automated assignment of material properties using automatic object detection

In the science of computer vision, object detection allows computers to detect and identify objects presented to them in the form of images. Several techniques such as Deep Learning and Transfer Learning are used to ‘teach’ computers. Deep Learning algorithms extract high-level, complex abstractions as data presentations through a hierarchical learning process[30] similar to that of the human brain. Object identification has a wide range of applications, including in self-driving or autonomous vehicles by such companies as Tesla and Google. Some object identification applications of smartphones can identify types of flowers, plants, birds, fish etc. from images taken by the smartphone’s camera. Object identification can be easily adopted to images of a death-scene for automated identification and assignment of material properties of ground-surface materials, sources of thermal radiation and other objects relevant to the postmortem heat transfer process.

11.2.19 Skin thermal conductivity adjusted to simulate clothing during postmortem cooling

One way to overcome absence of numerical modelling techniques for clothes would be to establish and add the thermal resistance value of each clothing item to the thermal resistance value assigned to the skin of the 3D computational model. This technique was used by Stolwijk[31] thermoregulation model.

11.2.20 Numerical simulation of natural condensation during postmortem cooling

Natural condensation such as dew formation affects the rate of postmortem cooling by evaporative cooling on the surface of the dead body. Formation of dew depends on a number of meteorological factors including air temperature, barometric pressure, and relative humidity (dew point). Neither empiric nor numerical methods of death-time estimation today account for the cooling effects of natural condensation on postmortem cooling. Numerical simulation of water vapour condensation[32] can be applied in the MAT Protocol using relative humidity data from the meteorological record.

11.2.21 Numerical simulation of natural precipitation during postmortem cooling

The three common forms of natural precipitation that affect postmortem cooling are rain, snow, and hail. The effect of natural liquid precipitation such as rain on a dead body is to wet the dead body's clothing items, if the body is clothed, or to wet the naked skin. Wet clothes in turn would accelerate postmortem cooling by evaporative skin cooling. Fluid drops landing on the naked skin would also absorb heat from skin and result in accelerated cooling in comparison to dry skin. Fluid viscosity would predict the potential maximum flow-off rate of the liquid precipitant while body position, posture and anatomical location of each drop/liquid collection would determine the flow-off rate from the body. Numerical simulation of wet clothing is described in the literature[33]. These techniques can be applied in the MAT Protocol.

Numerical simulation of snowfall over complex terrain was described by Wang and Huang[34]. Such a technique would be suitable for simulating snowfall over the complex topography of a 3D computational phantom. Heat transfer from the body to snowfall on the body would result in accelerated skin cooling. Numerical simulation of snow melting as described by Nagai et al[35] could be performed for this effect. Numerical simulation of heat transfer with hail particles and subsequent melting can also be undertaken. For each type of precipitation, the amount or rate precipitation to be applied in the MAT Protocol would be obtained from the historical meteorological record. Again, the MAT Protocol would simulate the exact amount of precipitation that occurred during the final estimated PMI.

11.2.22 Death-time estimation in children using the MAT Protocol

The MAT Protocol can equally be applied to death-time estimation of infants and small children using the same size or smaller MAT device and appropriate 3D computational phantoms from the Virtual Population.

11.2.23 Application of the MAT Protocol in real-world case work

Application in real-life case work would be the ultimate platform on which of the MAT Protocol would be verified.

11.2.24 Numerical forensic entomology modelling coupled with the MAT Protocol for death-time estimation from putrefaction to skeletonization

Forensic entomology involves the study of the natural life cycle and interactions of insects that colonise and use a decomposing body (carrion) as a food source. Insects visit and inhabit carrion in waves of often predictable pattern, a process called insect succession. Pregnant female blow flies (Diptera: Calliphoridae), house flies (Diptera: Muscidae) or flesh flies (Diptera: Sarcophagide) arrive on a dead body and begin laying eggs within minutes after death[36]. Oviposition is on moist body surfaces such as eyes, nostrils, mouth, open wounds etc. The flies fly only when the weather is favourable, i.e. warm, no rain, daylight. Deposited eggs incubate over a number of hours, the rate of which is temperature dependent.

Upon hatching, larvae aggregate as they secrete digestive enzymes to break down carrion, to form maggot-masses consisting up to several hundred-thousand individuals. Maggot-masses generate heat that can be several degrees Celsius above ambient temperature[36]. The heat enhances their motility, digestion, growth, and denaturation (cooking) of carrion protein. The maggot-mass confers protection of individual larvae but represents intense competition for heat and nutrition. Larvae undergo several stages of maturation (insta stages) as their length and width increase. When no further growth can occur, the larvae stop feeding, leave the carrion and bury themselves in the surrounding soil to begin pupation. Fly larvae attract higher-order insects such as beetles that feed upon them.

The maturation stage of a fly larva and evidence of higher-order insect predictors are used by forensic entomologists to estimate the minimum PMI required for those observations to exist after oviposition, which is assumed to occur immediately after death. Such estimation is done by collection of mature fly larvae from the dead body and collection of any unhatched fly eggs. The larvae are killed by alcohol or hot-water submersion, while the eggs are incubated and reared in the laboratory under constant ambient temperature calculated using the Accumulated Degree Day (ADD) concept (because of the problem of the TOD being the unknown, as discussed in 3.2.8). The effect of maggot-mass temperatures on larvae growth rates cannot be represented by the ADD method and may result in lower laboratory growth rates and thus uncertainty in forensic entomology PMI estimation[37]. A forensic entomology numerical model to be implemented alongside the MAT Protocol would:

- simulate oviposition only under favourable environmental conditions and only on moist surfaces of a 3D computational human phantom by numerical fly species common in the region,
- simulate egg incubation using historical meteorological data according to the MAT Protocol and do away with ADD,
- simulate larva motility using a simulated sensory-motor system and known larva motility rates,
- simulate maggot-mass formation and inter-individual larva competition determined by larva size, larva age and larva temperature.

- simulate maggot-mass heat generation and heat transfer by thermal conduction, thermal radiation, thermal convection, friction, and larva motility,
- simulate temperature-dependent larval growth rates,
- simulate insect succession and larva predation, and
- simulate progressive loss of soft tissue of the 3D computational phantom.

The process of death-time estimation using the MAT Protocol would involve iterative comparisons of:

a) blowfly larvae size,
b) insect succession,
c) extend of soft tissue loss due to larva consumption, and
d) extent of body skeletonization predicted in the numerical simulation relative to that documented at the scene for several candidate PMIs.

It would make sense to couple such an entomology numerical model with the numerical method of simulating putrefaction and skeletonization discussed in 11.2.13.

11.2.25 The MAT Protocol, Big Data Analytics, Deep Learning and Artificial Intelligence

As application of the MAT Protocol l is predicted to become increasingly complex and data-intense, obvious future arenas in which numerical death-time estimation methods will play themselves out are Big Data Analytics[30], Deep Learning[30] and Artificial Intelligence (AI). The numerical nature of the MAT Protocol allows coupling of any numerical simulation technique relevant to death-time estimation. The multiple techniques suggested in the preceding subsections may evidently need to be coupled simultaneously, as occurs in nature. The MAT Protocol and its extended applications thus would qualify numerical death-time estimation as a stand-alone science – namely Numerical Thanatochronometry.

Bibliography and References Cited

1. Al-Alousi LM, Anderson RA (1986). Microwave thermography in forensic medicine. Police Surgeons, 30-42.

2. Al-Alousi LM, Anderson RA, Land DV (1994). A non-invasive method of temperature measurements using a microwave probe. Forensic Science International, 35-46.

3. Stauffer PR, Craciunescu OI, Maccarini PF, Wyatt C, Arunachalam K, Arabe O, Stakhursky V, Soher B, MacFall JR, Li Z, Joines WT, Rangarao S, Cheng KS, Das SK, Martins CD, Charles C, Dewhirst MW, Wong T, Jones E, Vujaskovic Z (2009). Clinical Utility of Magnetic Resonance Thermal Imaging (MRtI) For Realtime Guidance of Deep Hyperthermia. Proc of SPIE (7181): 1-12.

4. Wilk LS, Hoveling RJM, Edelman GJ, Hardy HJJ, van Schouwen S, van Venrooij H, Aalders MCG (2020). Reconstructing the time since death using non-invasive thermometry and numerical analysis. Science Advances, 6(22): eaba4243, 1-7.

5. Barazzetti L, Sala R, Scaioni M, Cattaneo C, Gibelli D, Guisani A, Poppa P, Roncoroni F, Vandone A (2012). 3D scanning and imaging for quick documentation of crime and accident scenes. Proc. SPIE 8359, Sensors, and Command, Control, Communications, and Intelligence (C3I) Technologies for Homeland Security and Homeland Defense XI, 835910.

6. Se S, Jasiobedzki P (2005). Instant Scene Modeler for Crime Scene Reconstruction. 2005 IEEE Computer Society Conference on Computer Vision and

---

Pattern Recognition (CVPR'05) - Workshops, San Diego, CA, USA, 2005, pp. 123-123, doi: 10.1109/CVPR.2005.477.

7. Raneri D (2018). Enhancing forensic investigation through the use of modern three-dimensional (3D) imaging technologies for crime scene reconstruction. Australian Journal of Forensic Sciences, 697-707.

8. Buck U, Naether S, Räss B, Jackowski C, Thali MJ (2013). Accident of homicide – Virtual crime scene reconstruction using 3D methods. Forensic Science International 225, 75-84.

9. Henβge C (1982). Temperatur-Todeszeit-Nomogramm für Bezugsstandardbedingungen der Leichenlagerung (Temperature-death-time nomogram for reference to standard conditions of cadaver storage. German) Krim. Forensische Wiss., 109-115.

10. Hartog EA, Lotens WA (2004). Postmortem time estimation using body temperature and a finite-element computer model. Eur J Appl Physiol 92, 734-737.

11. Mall G, Eisenmenger W (2005). Estimation of time since death by heat-flow Finite-element model part II: application to non-standard cooling conditions and preliminary results in practical casework. Legal Medicine, 69-80.

12. Barry JJ, Hill RH (2003). Computational modeling of protective clothing. International Nonwovens Journal, os-12 (3); 25-33.

13. Selle A, Su J, Irving G, Fedkiw R (2009). Robust high-resolution cloth using parallelism, history-based collisions and accurate friction. IEEE Transactions on Visualization and Computer Graphics, 15 (2); 1-12.

---

14. Gao N, Niu J, Zhang H (2006). Coupling CFD and human body thermoregulation model for the assessment of personalized ventilation. HVAC&R Research, 2 (3); 497-518.

15. Engineering ToolBox, (2003). *Convective Heat Transfer*. [online] Available at: https://www.engineeringtoolbox.com/convective-heat-transfer-d_430.html [Accessed 10 October 2020].

16. Gosselin M, Neufeld E, Moser H, Huber E, Farcito S, Gerber L, Jedensjö M, Hilber I, Di Gennaro F, Lloyd B, Cherubini E, Szvzerba D, Kainz W, Kuster N (2014). Development of a new generation of high-resolution anatomical models for medical device evaluation: the Virtual Population 3.0. Physics in Medicine and Biology, 5287-5303.

17. GISTEMP Team, 2020: GISS Surface Temperature Analysis (GISTEMP), version 4. NASA Goddard Institute for Space Studies. Dataset accessed 2020-10-20 at https://data.giss.nasa.gov/gistemp/.

18. Hansen J, Ruedy R, Sato M, Lo K (2010). Global surface temperature change, Rev. Geophys., 48, RG4004, doi:10.1029/2010RG000345.

19. Lenssen N, Schmidt G, Hansen J, Menne M, Persin A, Ruedy R, Zyss D (2019). Improvements in the GISTEMP uncertainty model. J. Geophys. Res. Atmos., 124(12): 6307-6326, doi:10.1029/2018JD029522.

20. Weiser M, Erdmann B, Schenkl S, Muggenthaler H, Hubig M, Mall G, Zachow S (2017). Uncertainty in temperature-based determination of time of death. Heat and Mass Transfer, 2815-2826.

---

21. Bluestein D (2017). Utilizing Computational Fluid Dynamics in Cardiovascular Engineering and Medicine—What You Need to Know. Its Translation to the Clinic/Bedside. Artif Organs, 41(2): 117-121.

22. Pennes HH (1948). Analysis of tissue and arterial temperatures in the resting human forearm. Journal of Applied Physiology, 93-122.

23. Saukko P, Knight B (2004). Knight's Forensic Pathology, 3Ed. Abingdon, Oxon: CRC Press.

24. Brás NF, Coimbra JTS, Neves RPP, Cerqueira NMFSA, Sousa SF, Fernandes PA, Ramos MJ (2015). Computational Biochemistry. In Editor J Reedijk of book (2015) *Reference Module in Chemistry, Molecular Sciences and Chemical Engineering*. doi:10.1016/b978-0-12-409547-2.10833-9.

25. Edelman GJ, Hoveling RJM, Roos M, Van Leeuwen TG, Aalders MCG (2013). Infrared Imaging of the Crime Scene: Possibilities and Pitfalls. Journal of Forensic Sciences, 58(5): 1156-1162.

26. Van Iersel M, Veerman H, van der Mark W (2009). Modelling a crime scene in 3D and adding thermal information. Electro-Optical and Infrared Systems: Technology and Applications VI. doi:10.1117/12.829990.

27. Chandrasekhar S (1960). Radiative Transfer. Dover Publications Inc. ISBN 978-0-486-60590-6.

28. Modest MF (2013). The Method of Discrete Ordinates (S_N-Approximation). In Editor MF Modest of book (2013) *Radiative Heat Transfer*, 3Ed. Elsevier BV. doi:10.1016/b978-0-12-386944-9.50017-0.

29. https://www.comsol.no/paper/using-comsol-multiphysics-software-and-the-application-builder-for-neutron-trans-26182.

30. Najafabadi MM, Villanustre F, Khoshgoftaar TM, Seliya M, Wald R, Muharemagic E (2015). Deep learning applications and challenges in big data analytics. Journal of Big Data, 2(1) doi:10.1186/s40537-014-0007-7.

31. Stolwijk JAJ (1970). A Mathematical model of physiological temperature regulation in Man. NASA Report.

32. Orazzo A, Tanguy S (2019). Direct numerical simulations of droplet condensation. International Journal of Heat and Mass Transfer 129, 432-448. ff10.1016/j.ijheatmasstransfer.2018.07.094ff. ffhal-01912759.

33. Chen YJ, Thalmann NM, Allen B (2012). Physical simulation of wet clothing for virtual human. The Visual Computer 28(6-8), 765-774. Dio: 10.1007/s00371-012-0687-y.

34. Wang Z, Huang N (2016). Numerical simulation of the falling snow deposition over complex terrain. Journal of Geophysical Research: Atmospheres 22(2), 980-1000. Dio:10.1002/2016JD025316.

35. Nagai N, Miyamoto S, Nishiwaki M, Takeuchi M (2009). Numerical simulation of snow melting on pavement surface with heat dissipation pipe embedded. Heat Transfer – Asian Research 38(5), 313-329.

36. Anderson GS, VanLaerhoven SL (1996). Initial studies on insect succession on carrion in southwestern British Columbia, J. Forensic Sciences 41, 617-625.

37. VanLaerhoven SL (2008). Blind validation of postmortem interval estimates using developmental rates of blow flies. Forensic Science International 180, 76-80.